Title
DECAY OP THE ^|Cr* COMPOUND NUCLEUS FORMED BY THE NUCLEAR REACTIONS 3He +a^T|, %Ie + ^Ti, l6O + 3^s, loo + 32S> AND ^Ne + s8Si

Author
Go, Man K.

Publication Date
1971-05-01

DECAY OF THE $^{50}Cr^{*}$ COMPOUND NUCLEUS FORMED BY THE NUCLEAR REACTIONS $^{3}He + ^{47}Ti$, $^{4}He + ^{46}Ti$, $^{16}O + ^{34}S$, $^{18}O + ^{32}S$, AND $^{22}Ne + ^{28}Si$

Man K. Go
(Ph. D. Thesis)

May 1971

AEC Contract No. W-7405-eng-48

LAWRENCE RADIATION LABORATORY
UNIVERSITY of CALIFORNIA BERKELEY

DISCLAIMER

DECAY OF THE $^{50}Cr^{*}$ COMPOUND NUCLEUS FORMED BY THE NUCLEAR REACTIONS $^{3}He + ^{47}Ti$, $^{4}He + ^{46}Ti$, $^{16}O + ^{34}S$, $^{18}O + ^{32}S$, AND $^{22}Ne + ^{28}Si$

Contents

DECAY OF THE $^{50}Cr^*$ COMPOUND NUCLEUS FORMED BY THE NUCLEAR REACTIONS $^{3}He + ^{47}Ti$, $^{4}He + ^{46}Ti$, $^{16}O + ^{34}S$, $^{18}O + ^{32}S$, AND $^{22}Ne + ^{28}Si$

Man K. Go

Department of Chemistry and
Lawrence Radiation Laboratory
University of California
Berkeley, California 94720

May 1971

ABSTRACT

Experimental excitation functions have been measured for nuclear reactions $^{3}He + ^{47}Ti$, $\alpha + ^{46}Ti$, $^{16}O + ^{34}S$, $^{18}O + ^{32}S$, and $^{22}Ne + ^{28}Si$. The observed products are ^{48}Cr and ^{48}V, and for the ^{3}He- and α-induced reactions, the ^{49}Cr production cross sections are also measured. The excitation function $^{46}Ti(\alpha,p)^{49}V$ is also obtained. Simple theoretical calculation based on the compound-statistical model is performed to calculate the excitation functions from ^{3}He and α reactions and found to agree reasonably with experiment.

The observed cross sections from the ^{18}O- and ^{22}Ne-induced reactions have been strongly suppressed by the Coulomb barrier. The $^{47}Ti(^{3}He,n)^{49}Cr$ excitation function is similarly found to be an order of magnitude smaller than that for the corresponding α-induced reaction.

A displacement of the experimental excitation functions relative to one another along the excitation energy axis is observed and explained by the effect of angular momentum upon the de-excitation of the compound nucleus. The shapes and magnitudes of the ratios of the various experimental excitation functions indicate the compound-nucleus model can be applied to these reactions. Bohr's independence postulate is valid, if

corrections are made for the difference in angular momentum of the different entrance channels.

Recoil ranges for ^{49}Cr and ^{48}Cr from $\alpha + {}^{46}Ti$ reaction are obtained by measuring the recoil distribution of these nuclei from a thick target. These recoil ranges are found to be consistent with the calculation based on the theory of Lindhard, Scharff, and Schiøtt for a compound-nucleus reaction.

I. INTRODUCTION

The observation of narrow resonances from nuclear reactions with low energy neutrons led Bohr[1] to introduce a compound nucleus mechanism for nuclear reactions in 1936. The narrow widths of the neutron absorption implied, according to the uncertainty principle, a long-lived excited state after the absorption of the neutron. This reaction model is extended to nuclear reactions involving other projectiles. In this model, the incident particle fuses with the target nucleus and the excitation energy is distributed quickly and randomly among all nucleons in the nucleus, forming a compound nucleus. The compound nucleus then de-excites slowly, in the nuclear time scale, by emitting particles and gamma rays. Weisskopf[2] showed how to treat the decay of the compound nucleus in a statistical way. Ericson[3] extended the model to include the conservation of angular momentum and a formalism for the study of level density. Since then the compound-statistical mechanism has been widely applied to nuclear reactions of low and intermediate energies.[4]

The validity of the assumption that statistical equilibrium will be attained in the excited nucleus has been investigated by Harp et al.[5] They solved numerically a Botzmann-like master equation for a Fermi-gas system and concluded that with excitation energies even up to the vicinity of the total binding energy, the bulk of the de-excitation of nuclei may be treated as emissions from an equilibrium system.

Experimental evidence for the concept of compound nucleus reaction greatly increases in the 1960's. Measurements of particle evaporation spectra,[6,7] nuclear temperature,[8] fluctuations in excitation functions,[9] complete fusion reaction cross sections,[10] recoil range distributions,[11] isomeric yield ratios,[12] and conventional excitation functions[13] were

made. Only experiments for the direct measurement of the compound nucleus life time[14] remain untried.

On the theoretical front, calculation of excitation functions based on the compound-statistical theory[15] were made possible by high speed electronic computers. Increasing attention has been paid to angular momentum effects,[16] nuclear shell effects,[17] and the effects of the competition between particle and gamma emission on the decay of the compound nucleus.[18,19] Recently, attempt has been made to unify the compound nucleus model with the microscopic approach to nuclear reactions.[20]

One of the features of the compound nucleus reaction model is the independence postulate--the decay of the compound nucleus is independent of its mode of formation. Ghoshal[21] devised a method of testing this postulate by forming a compound system from different entrance channels and then comparing the production of the same final radionuclide.* Many experiments[22-25] following Ghoshal's work has been performed and the results agree qualitatively with the compound nucleus model. In forming the compound nucleus, however, there are many constants of motion, in addition to energy, that must be conserved: linear momentum, angular momentum,[26] parity, nucleon number, and possibly isotopic spin.[8] In the classical test of the independence postulate, only energy, nucleon number and linear momentum conservation are considered. Therefore, apparent violation of the independence postulate is expected for systems formed with significantly different angular momentum or isotopic spin. More recently, D'Auria et al.[27] tested the independence postulate by

*See Appendix V.

taking into account both the excitation energy and angular momentum. They verified the independence postulate for the ^{75}Br compound nucleus.

In this work, the compound system $^{50}Cr^{*}$ is investigated. The reaction cross sections for pn and 2n evaporation are measured in the "iso-compound nuclear system" tradition. The effect of positive reaction Q values and the nuclear Coulomb barrier is noted. For the reactions involving ^{3}He and ^{4}He particles, the excitation functions are calculated based on the compound-statistical theory. The effect of high angular momentum brought in by heavy ion bombardments are also discussed. For the ^{4}He reactions, ^{48}Cr and ^{49}Cr recoil ranges are measured by a thick-target method.[28] It is hoped to establish the validity of the compound nucleus reaction mechanism to systems with masses near 50.

The following reactions were studied:

$^{47}Ti(^{3}He, n)^{49}Cr$ $\quad$ $^{46}Ti(\alpha, n)^{49}Cr$

$^{46}Ti(\alpha, p)^{49}V$

and

$^{47}Ti(^{3}He,2n)^{48}Cr$	$^{47}Ti(^{3}He,pn)^{48}V$
$^{46}Ti(\alpha,2n)^{48}Cr$	$^{46}Ti(\alpha,pn)^{48}V$
$^{34}S(^{16}O,2n)^{48}Cr$	$^{34}S(^{16}O,pn)^{48}V$
$^{32}S(^{18}O,2n)^{48}Cr$	$^{32}S(^{18}O,pn)^{48}V$
$^{28}Si(^{22}Ne,2n)^{48}Cr$	$^{28}Si(^{22}Ne,2n)^{48}V$

II. EXPERIMENTAL PROCEDURES

Experimental determinations of the excitation functions for the nuclear reactions in this work were performed using the stacked foil method. Aluminum foils were usually used as beam degrader and target support. The target support also served as recoil catcher. Normally several sets of degrader-target-support were stacked in a target holder. Ion beams from particle accelerators were allowed to impinge upon the target.

After the bombardment, each target-support unit was mounted on a 1/16-inch aluminum card and counted with a Ge(Li) γ-ray detector or a Si(Li) X-ray detector. These solid state detectors were equipped with linear amplifiers, multichannel analyzers and sometimes a magnetic tape recording device.

Data from the multichannel analyzer were fed into the CDC 6600 computer for photopeak analyses. Because the solid state detectors used have very good resolution, the radioactive decay curves obtained were often of the single-component type, such that hand analysis was sufficient. Sometimes the decay data were fitted by computer, in the least-square sense, to the radioactive decay equation.

The result of the decay curve analysis is a set of counting rates at the end of bombardment for the product nuclei. These counting rates were corrected for detector efficiency and decay branching ratios to obtain the absolute disintegration rates at time zero, D_0.

The reaction cross sections were then calculated by

$$\sigma_E = \frac{D_0}{NI(1 - e^{-\lambda\tau})} \quad , \qquad (1)$$

where σ_E = cross section at a given energy E, in cm^2,

D_0 = disintegration rate at the end of bombardment, in dis/sec,

N = target thickness in atoms/cm^2,

I = beam intensity in particles/sec,

λ = decay constant of the radioisotope, in min^{-1},

τ = length of bombardment time, in minutes.

Details of the experimental procedures are discussed in the following sections. During the course of this work, nuclear forward-recoil experiments were also performed. These recoil range measurements will be discussed in part V of this report.

A. Target Preparation

Most targets used in this work were prepared by vacuum evaporation. Normally, circular foils 1-inch in diameter were punched out from a 0.25 mil ($\sim$ 1.8 mg/cm^2) aluminum foil and used as target support. These aluminum foils were placed inside a vacuum evaporation apparatus. The target material was then evaporated in a tungsten crucible onto the aluminum foils to form a circular surface 3/4-inch in diameter. The thickness of the target was calculated from the weights of the aluminum foil before and after evaporation and the known area of the deposited material. The thickness of the target material was typically 500 μg/cm^2. Up to six aluminum foils can be placed in the vacuum evaporation apparatus approximately the same distance from the crucible. The thicknesses of the six targets obtained from one evaporation usually agree to within $\pm$3%. This is an indication of good target uniformity. Observed under a low-power microscope, the evaporated surface was normally very smooth.

After evaporation the foils were mounted on 15-mil stainless steel rings to prevent the evaporated material from touching other target foils or aluminum degrader foils when they were assembled into a stack.

Most of the titanium targets for $^{46}Ti + {}^{4}He$ and $^{47}Ti + {}^{3}He$ reaction sutdies were prepared by vacuum evaporation using the enriched isotopes obtained from Oak Ridge National Laboratory. The isotopes are in the form of titanium dioxide. Because vacuum evaporation involved high temperature and may change the chemical composition of titanium dioxide, a few targets were analyzed colorimetrically for Ti content (see Appendix I).

Some of the titanium targets were prepared by sedimentation method. This was done by settling a suspension of titanium dioxide powder in alcohol onto 1-mil aluminum foils by means of a glass tubing, 3/4-inch in inside diameter. The settling time was about one day. Then the settled oxide was baked at 200°C for one hour to remove organic impurities. Ten-mil copper rings were then mounted to protect the layer. The thickness of the settled layer was calculated from its weight and area defined by the settling glass tubing. Usually uniform target, 1 mg/cm^2 thick, was obtained.

The sulfur targets used in $^{18}O + {}^{32}S$ reaction were prepared by vacuum evaporation of natural sulfur on 1/4-mil aluminum backing foils. Because sulfur has a low melting point and is a poor conductor of heat, further treatment of the evaporated target is necessary to prevent loss of targer sulfur material during bombardment. A thin (about 100 μg/cm^2) aluminum coating was evaporated onto the sulfur surface to serve as cover and heat conductor. The target then was mounted on a stainless steel ring as before.

The evaporated sulfur layer was not uniform, it showed "mountains and valleys" under a microscope. However, the pattern of these mountains and valleys of sulfur material was quite regular and was evenly distributed throughout the evaporated surface. During ^{18}O bombardment, a wobbled beam was used so that the sulfur target can be regarded as uniform.

Natural sulfur contains $^{32}S(95\%)$, $^{33}S(0.8\%)$, and $^{34}S(4.2\%)$. Because the reactions studied were $^{32}S(^{18}O,2n)^{48}Cr$ and $^{32}S(^{18}O,pn)^{48}V$, the abundance and expected reaction cross section for the ^{33}S and ^{34}S isotopes are too low to interfere under the experimental conditions.

For $^{16}O + ^{34}S$ reaction, the sulfur targets were prepared in the same way as the natural sulfur targets, except ^{34}S enriched sulfur was used instead of natural sulfur. The enriched sulfur was also obtained from Oak Ridge National Laboratory.

Natural silicon was used to prepare targets for the $^{22}Ne + ^{28}Si$ reaction study. The Si targets were also prepared by the vacuum evaporation method.

Table I summarizes the mass analysis and chemical composition of the materials used to prepare the targets. The data of the mass analysis of the enriched isotopes are obtained from Oak Ridge National Laboratory.

B. Range-Energy Relations

Determination of beam energy on each target is based on the knowledge of the energy-loss of charged particles passing through various target materials. Although experimental measurements of the energy loss by charged particles are scarce, there are several theoretical calculations which agree with existing experimental data.[29,30,31]

Table I. Mass analysis and chemical composition of target material.

Target	Mass analysis		Chemical impurities (maximum) (percent)
	mass number	percent	
Titanium-46	46	81.2	Ca < 0.01
(TiO_2)	47	2.1	Fe < 0.05
	48	14.5	Si < 0.07
	49	1.1	W < 0.05
	50	1.1	others negligible
Titanium-47	46	1.9	Fe < 0.02
(TiO_2)	47	79.5	Si < 0.03
	48	16.5	others negligible
	49	1.1	
	50	1.0	
Sulfur-34	32	65.9	Zn < 0.02
	33	0.57	Al,Cd,Cr,Cs,Ge,Ni,
	34	33.5	Pt,W, Zr each < 0.05
	36	< 0.05	
Sulfur	32	95.0	
(natural)	33	0.76	
	34	4.22	negligible
	36	0.014	
Silicon	28	92.2	
(natural)	29	4.7	negligible
	30	3.1	

Steward[32] has recently developed a method for calculating ranges of any charged particles in non-gaseous media.

For ^{3}He and ^{4}He reactions, the tabulation of Williamson, et al.[29] was used. For ^{16}O, ^{18}O, and ^{22}Ne reactions, Steward's program was used. Figure 1 represents a typical range-energy curve as calculated by Steward's program.

Calculation of beam energy after the charged particles has passed through a certain thickness of degrader or target material can easily be done by first finding the range of the initial beam, then subtracting the thickness of target or degrader to obtain the residual range, and finally reading the residual energy from the range-energy curve. This procedure minimizes the effect from the errors in absolute magnitude of the range-energy curves, because only the differences in ranges and energies are used.

The uncertainty in beam-energy determination is mainly due to the uncertainty in the initial energy from the accelerator, beam-energy spread due to degradation through matter, and the variations in target and degrader thickness. For heavy-ion reactions the uncertainty can be as large as 2 to 6 MeV at the low energy portion of the beam.

C. Bombardments

The Berkeley 88-inch spiral ridge cyclotron[33] was used for ^{3}He and ^{4}He bombardments. The initial beam energies were 30 and 47 MeV respectively for ^{3}He and ^{4}He with energy resolution of about 0.14%. The current used is about 1 $\mu A(3.14 \times 10^{12}$ $He^{++}/sec)$. The bombardment time was from 10 minutes to one hour.

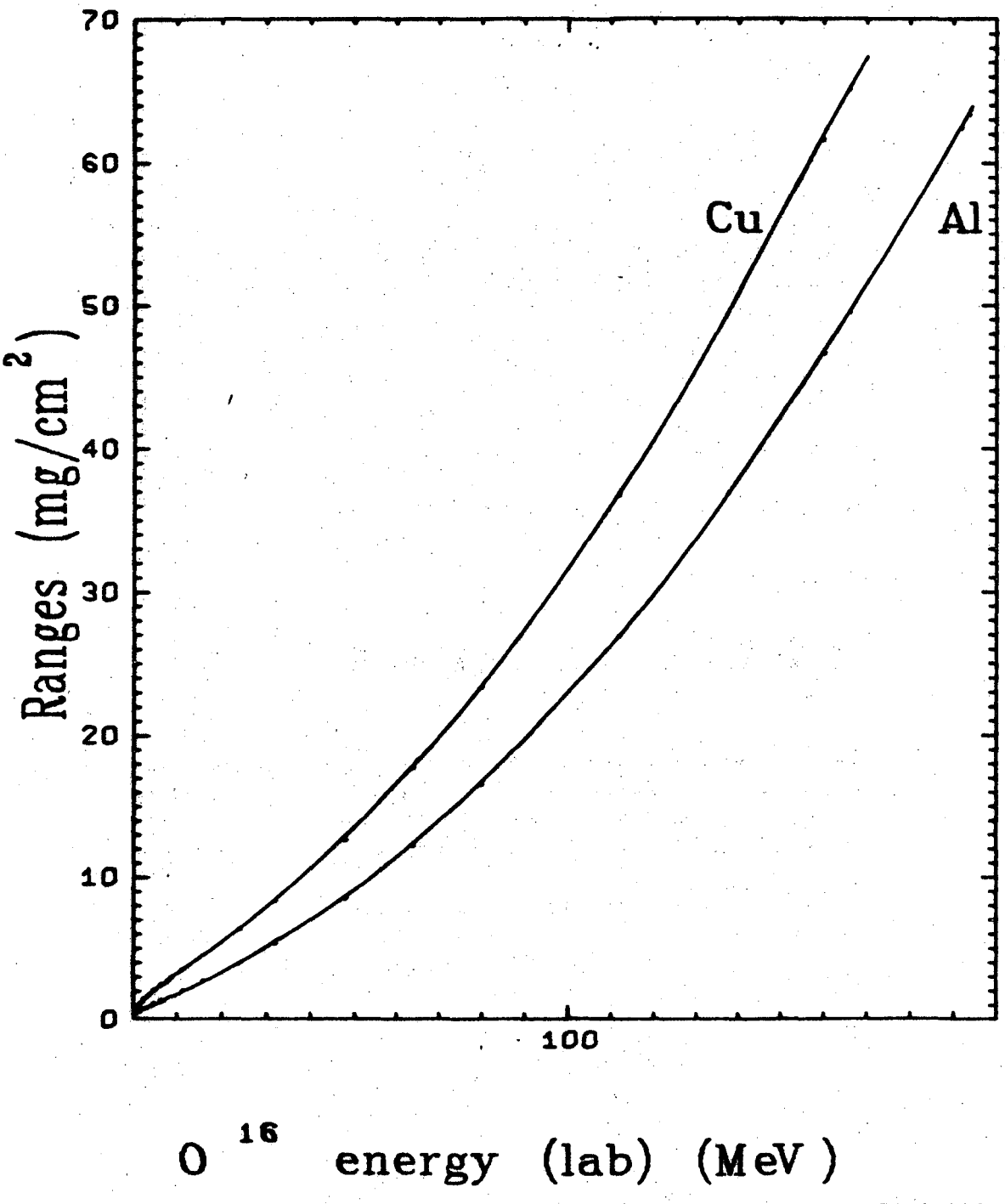

Fig. 1. Range energy curves for ^{16}O particles on natural copper (Cu) and aluminum (Al). These curves are drawn from the calculation by Steward (Ref. 32). Curves similar to these for other ion-target pairs are used to determine the bombardment energy for each target in the stack.

For ^{16}O, ^{18}O, and ^{22}Ne bombardments, the Berkeley Heavy Ion Linear Accelerator (Hilac)[34] was used. The Hilac supplied a pulsed beam, 2 msec per pulse and 15 pulses per second, of energy 10.4 ± 0.2 MeV per nucleon. The current used was about 150 nanoamperes. This low current was necessary to avoid burning the targets. The heavy ion beam was often wobbled to eliminate hot spots in the target. Bombardment time was typically 1 to 1.5 hours.

The Hilac was also used for ^{3}He and ^{4}He bombardments. The energy for ^{3}He is 31.2 ± 0.6 MeV and for ^{4}He is 41.6 ± 0.8 MeV. Bombardment time was usually 20 to 60 minutes. The excitation functions obtained from the Hilac runs do not differ significantly from the 88-inch cyclotron runs.

The target holder for most of the experiments was the copper tag target holder, shown in Fig. 2. This target holder is a copper block with a water cooling system. The target foils with appropriate degrader foils and cover foils were screwed down with a 3/16-inch thick aluminum collimator. The target holder was then inserted at the end of the beam pipe and properly shielded by a magnetic field, so that the target holder can be used as a Faraday cup. The beam current can then be measured directly and continuously. The total current was recorded with an integrating electrometer.

D. Counting Procedures

After irradiation, the target was dismantled, and the target foils were mounted on standard aluminum counting cards, 3-1/2" × 2-1/2" × 1/16" in dimension, with a slight depression in the center. The mounted samples were counted with a lithium-drifted germanium

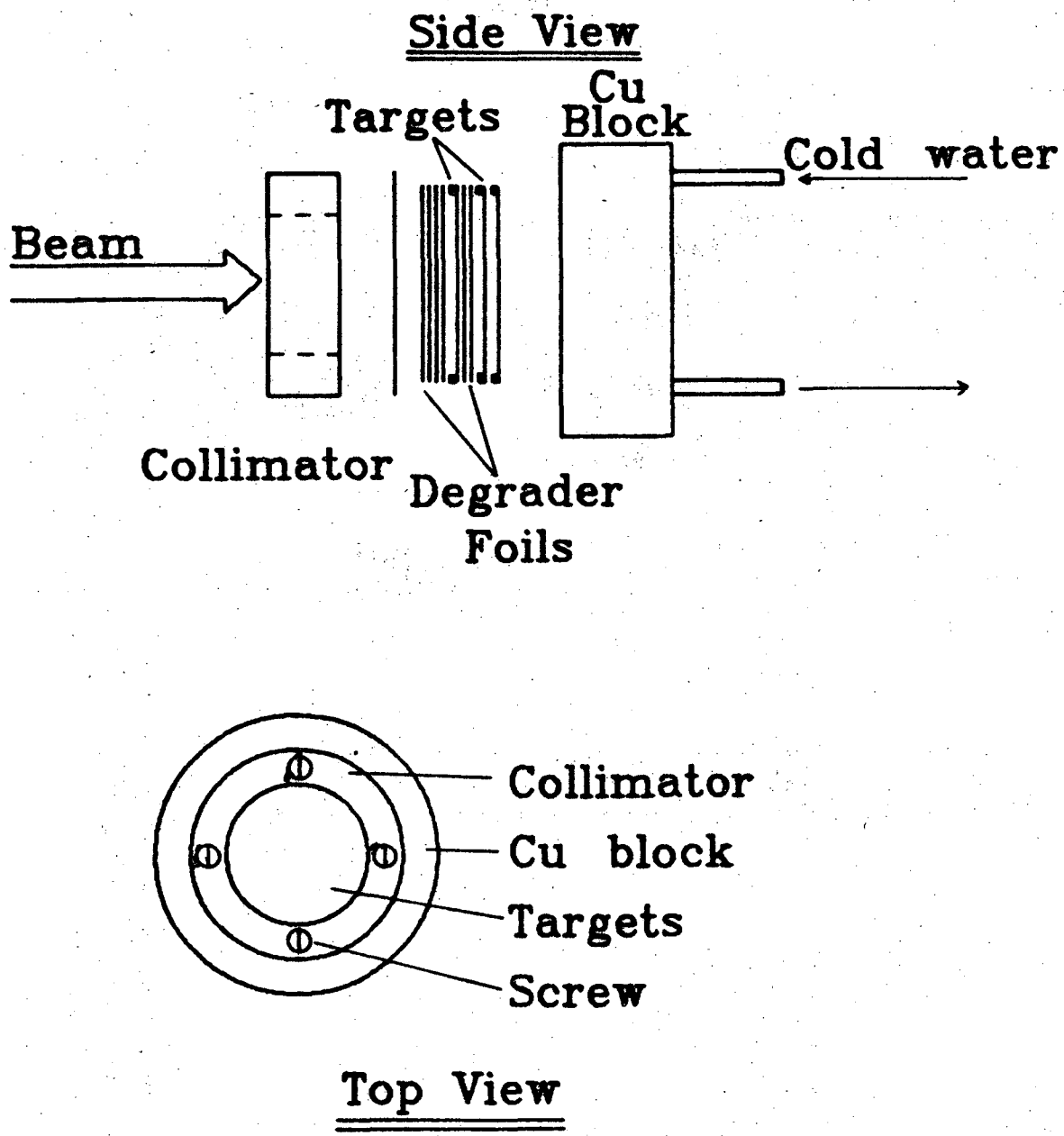

XBL 7010-6851

Fig. 2. Copper tag target assembly used for bombardments. The particle beam is usually collimated to 3/8" before reaching the target assembly. The purpose of the Al collimator in the figure is mainly to secure the foils in the target.

gamma-ray detector[35] or a lithium-drifted silicon x-ray detector.[36] The fabrication and operation of these high resolution semiconductor devices has been described by Goulding.[37] The radioactivities detected in this work are summarized in Table II.

Two Ge(Li) γ-ray detectors were employed in this work. These were planar detectors having active volumes 14 cm^3 and 7 cm^3. The smaller detector was connected to a high count rate, high resolution amplifier system (see Fig. 3) designed by Goulding, Landis, and Pehl.[38] A linear amplifier-biased amplifier system[39] was used with the 14 cm^3 Ge(Li) detector. The amplifier signals were led to either a 400-channel Victoreen[40] or a 1024-channel Northern Scientific[41] pulse-height analyzer for singles spectra. The resolution of the gamma-ray detector systems are about 2.5 keV and 1.4 keV (full width at half maximum) at the 122 keV ^{57}Co gamma-ray for the 14 and 7 cm^3 detectors, respectively.

The x-ray detector used was a lithium drifted silicon detector with a beryllium window. X-rays as low as 3.5 keV energy can be measured with a resolution of about 0.5 keV. A resolution of 0.1 keV could be obtained if a pulsed-light feedback preamplifier[42] is used.

The data accumulated in the analyzer can be printed out onto a paper strip or written on a magnetic tape. The magnetic tape-pulse height analyzer interface unit (see Fig. 4) was designed and built by M. Lee[43] in this laboratory. The tape recorder used is available commercially.[44]

Table II. Radioisotopes measured in this work.

Nuclide	Half-life	Decay mode		Major radiations (keV)	(yield/decay)
^{49}Cr	41.9 min	β^+	94%	63.	(14%)
		EC	6%	91.	(28%)
				153.	(13%)
				511.	(186%)[a]
^{48}Cr	23 hours	EC	100%	116.	(98%)
				310.	(99%)
^{49}V	330 days	EC	100%	4.5 Ti x-ray[b]	
^{48}V	16.1 days	β^+	61%	511.	(120%)[a]
		EC	39%	983.	(100%)
				1312	(97%)

[a]The 511 keV radiation is from annihilation of positrons.

[b]See Appendix IV for the percentage of Ti x-rays per decay of ^{49}V.

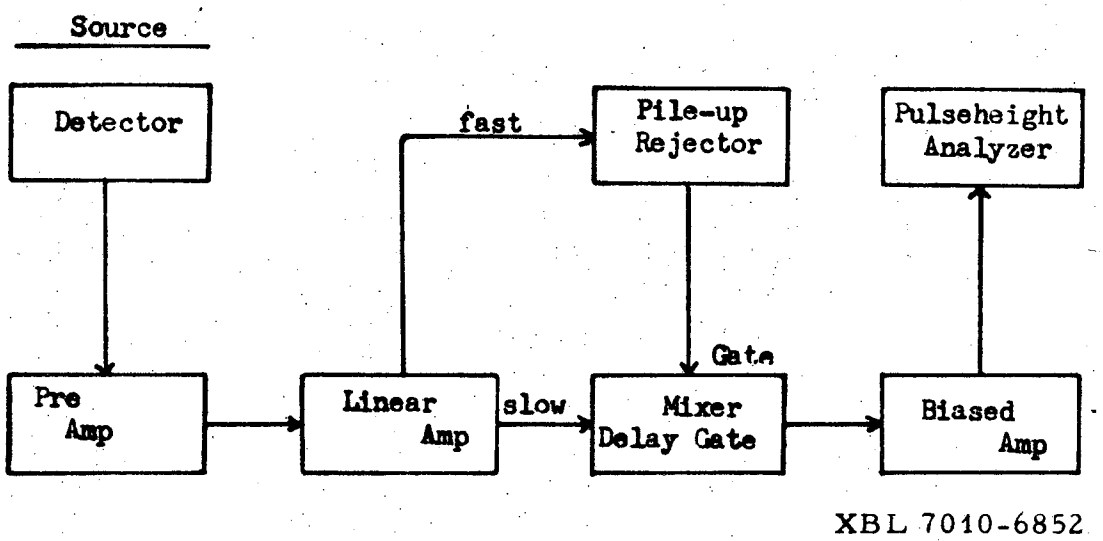

Fig. 3. Block diagram for the high count rate, high resolution gamma-ray detection system.

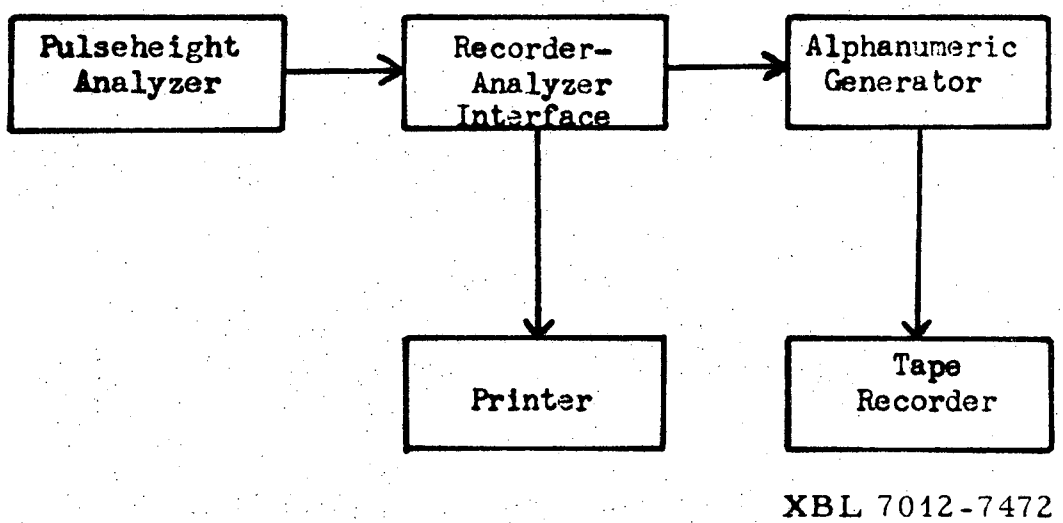

Fig. 4. Magnetic tape recorder or printer readout system for spectra recording.

E. Data Analysis

Most of the spectra from the analyzer were written onto 7-inch reel magnetic tapes. Other spectra were printed on paper strips and the data were later punched on IBM cards. The spectra were then fed into a CDC 6600 computer for photopeak analysis. The gamma ray spectra analysis program, SAMPO, was developed by Routti and Prussin[45] in this laboratory. Detailed applications of this computer code is given by Bernthal[46] and Routti.[47] The SAMPO program attempts to fit the gamma ray photopeak by a Gaussian function with an exponential tailing off on both the low- and high-energy sides. The code can also be used to resolve multiple peaks.

A sample gamma ray spectrum is shown in Fig. 5. Computer analyzed singles and doublet photopeaks with the residuals are shown in Fig. 6 and Fig. 7.

The result from the gamma ray photopeak analysis is a set of photopeak intensities at various energies. In this work, almost all the photopeaks are from a single radioisotope. Normally a graphical decay curve analysis was sufficient to obtain the decay rates of the various radioactivities at the end of bombardment. In some cases a least square code was used to resolve the decay components or to yield a better fit to the single component decay curve. Two programs have been used, RAD[48] and CLSQ.[49] Both codes can treat decay curves of up to 10 components and yield solutions for half-lives, initial activities, and standard deviations in the fitted parameters.

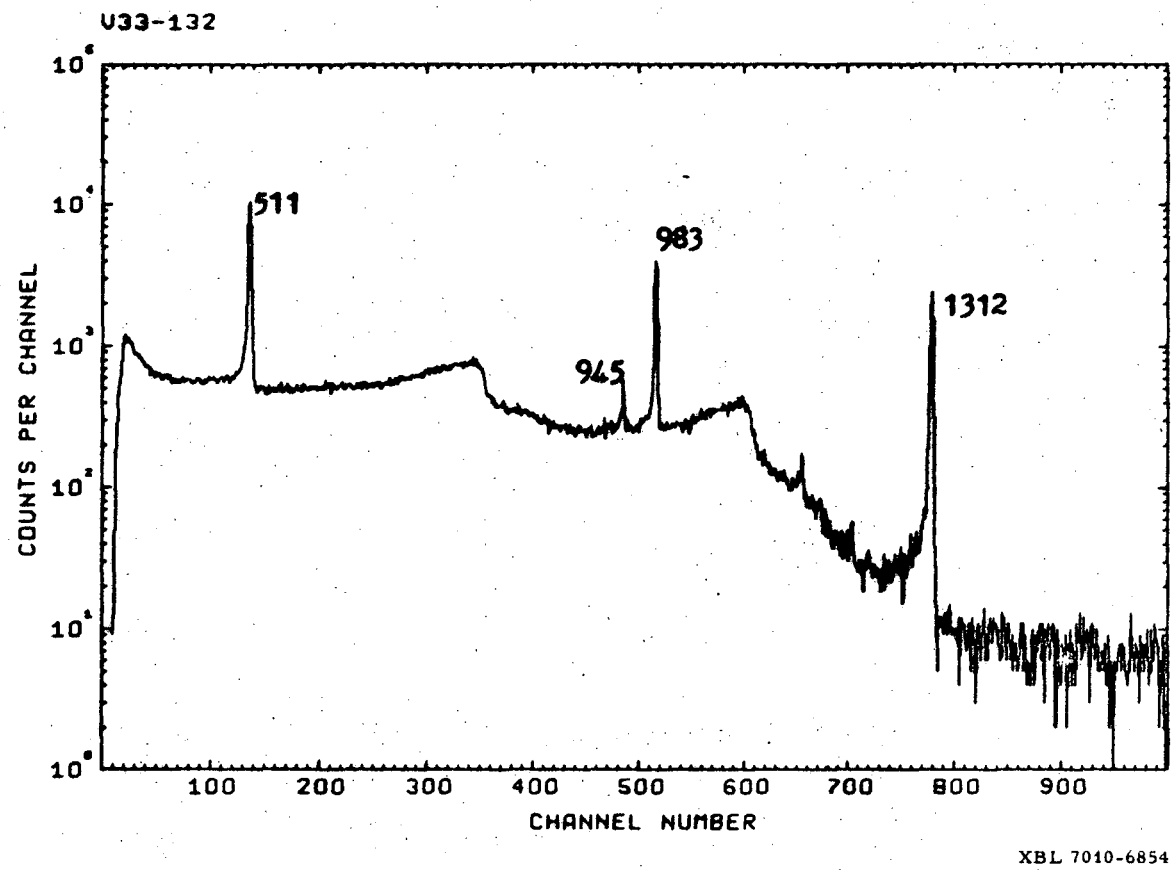

Fig. 5. A typical gamma-ray spectrum. This spectrum is from the activity of ^{48}V. The numbers near the peaks in the figure are the energies of the gamma-rays in keV.

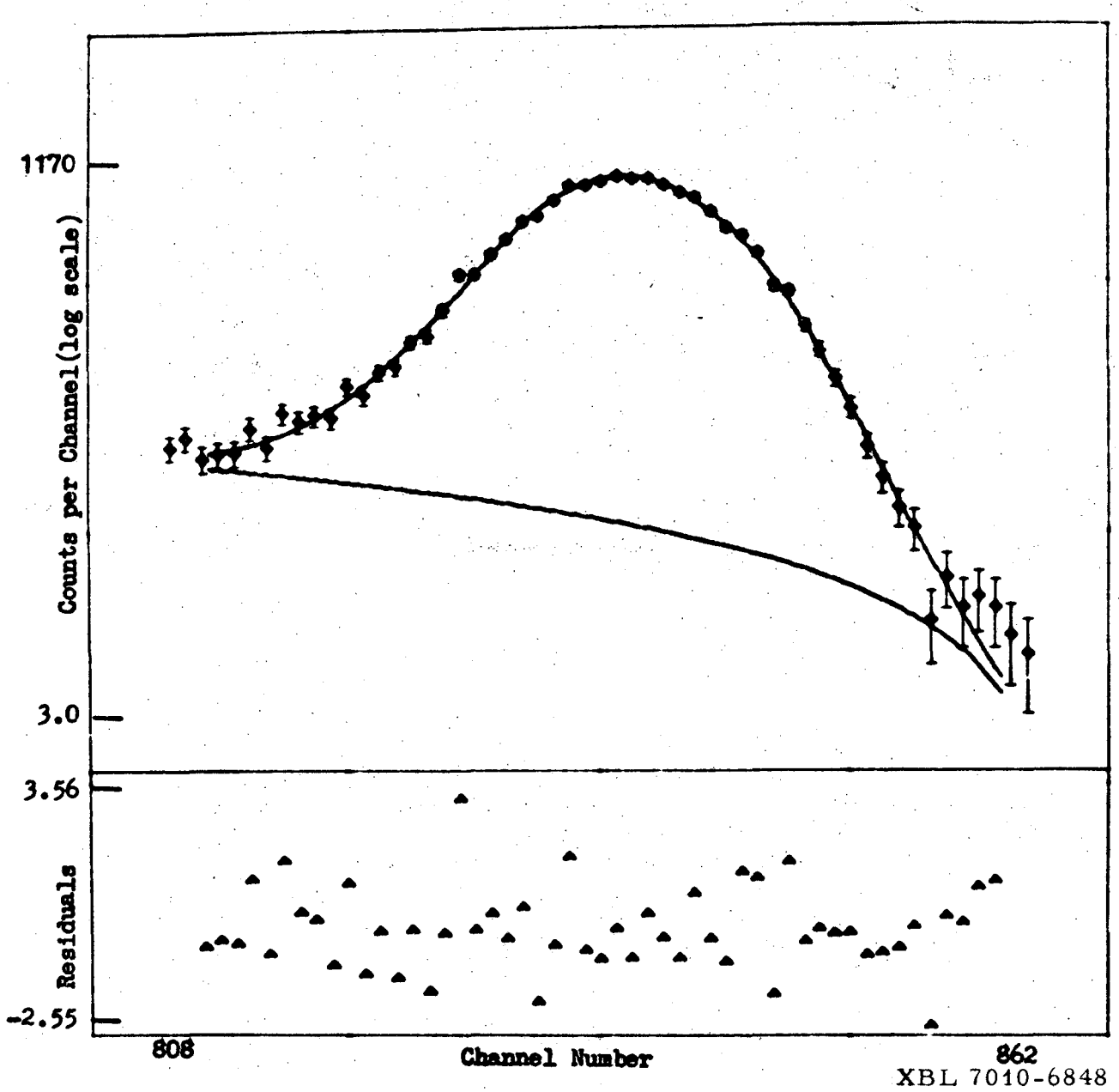

Fig. 6. Computer analyzed single peak. The solid lines are the fitted peak and the background, the points with error bars are the experimental data. The residuals are expressed in standard deviations of the counts measured. Small and randomly distributed residuals indicate a good fit.

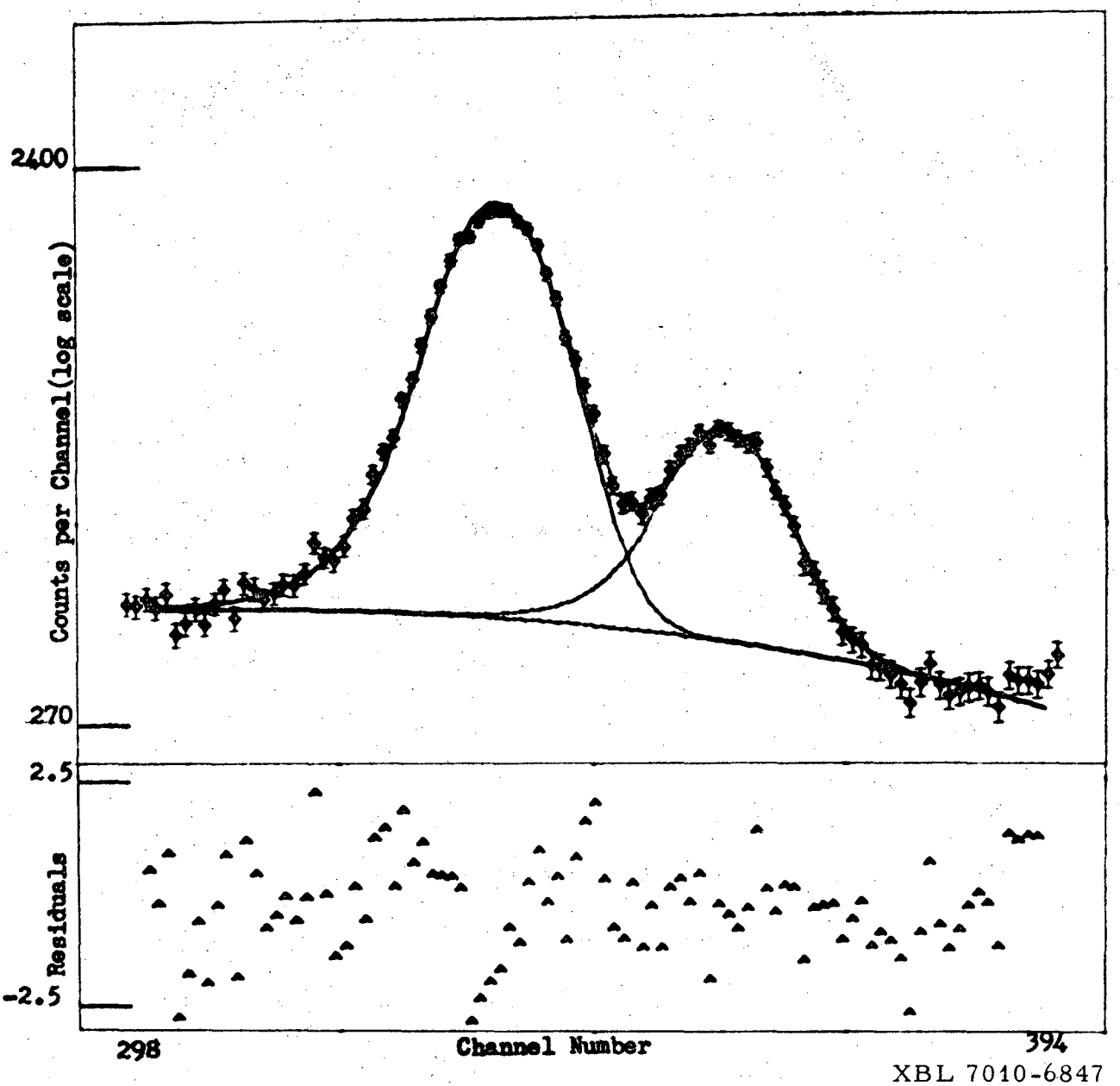

Fig. 7. Computer fit to a gamma-ray doublet. The data are the K x-ray from the decay of ^{203}Hg.

III. EXPERIMENTAL RESULTS

The reaction cross sections for the following nuclear reactions were measured:

$$\left.\begin{array}{l} {}^{3}He + {}^{47}Ti \\ {}^{4}He + {}^{46}Ti \\ {}^{16}O + {}^{34}S \\ {}^{18}O + {}^{32}S \\ {}^{22}Ne + {}^{28}Si \end{array}\right\} \longrightarrow {}^{50}Cr^{*} \longrightarrow \left\{\begin{array}{l} {}^{48}Cr + 2n \\ {}^{48}V + pn \end{array}\right.$$

Production of ^{49}Cr or ^{49}V from ^{4}He and ^{3}He reactions was also measured. The excitation functions are presented in Fig. 8 through Fig. 14. The following sections deal with the properties of the excitation functions. Nuclear reaction Q values and Coulomb barriers are summarized in Table III for easy reference.

Experimental and theoretical considerations for recoil experiments of ^{49}Cr or ^{48}Cr from ^{3}He and ^{4}He reactions will be given in Chapter V.

A. Excitation Functions

1. $^{4}He + {}^{46}Ti$

The Q value for the nuclear reaction $^{4}He + {}^{46}Ti \rightarrow {}^{50}Cr^{*}$ is 8.6 MeV, which is considerably lower than all other nuclear reaction pairs studied in this work (see Table III). The reaction Q values for the production of ^{49}Cr and ^{49}V are only slightly negative, thus the reaction threshold is the Coulomb barrier and we should expect to see the peak of these excitation functions. Figure 8 shows the excitation functions for ^{49}Cr, ^{49}V, ^{48}Cr, and ^{48}V production from $^{4}He + {}^{46}Ti$ reactions. Indeed we see that the excitation functions (α,n) and (α,p) do go through a maximum.

Table III. Coulomb barriers and Q values for reactions of interest.

Reaction pair	Product	Coulomb barrier[a] (MeV)	Q values[b] (MeV)
$^{3}He + ^{47}Ti$	^{50}Cr	8.4	20.3
	^{49}V		10.7
	^{49}Cr		7.4
	^{48}Cr		- 3.0
	^{48}V		- 0.8
$^{4}He + ^{46}Ti$	^{50}Cr	8.2	8.6
	^{49}V		- 1.0
	^{49}Cr		- 4.4
	^{48}Cr		-14.8
	^{48}V		-12.6
$^{16}O + ^{34}S$	^{50}Cr	21.3	15.6
	^{48}Cr		- 7.7
	^{48}V		- 5.6
$^{18}O + ^{32}S$	^{50}Cr	21.2	23.5
	^{48}Cr		0.2
	^{48}V		2.3
$^{22}Ne + ^{28}Si$	^{50}Cr	23.0	20.8
	^{48}Cr		- 2.5
	^{48}V		- 0.4

[a] The Coulomb barriers were calculated with a nuclear radius parameter $r_o = 1.5$ fm.

[b] Q values were based on the masses given in Table of Isotopes (Ref. 70).

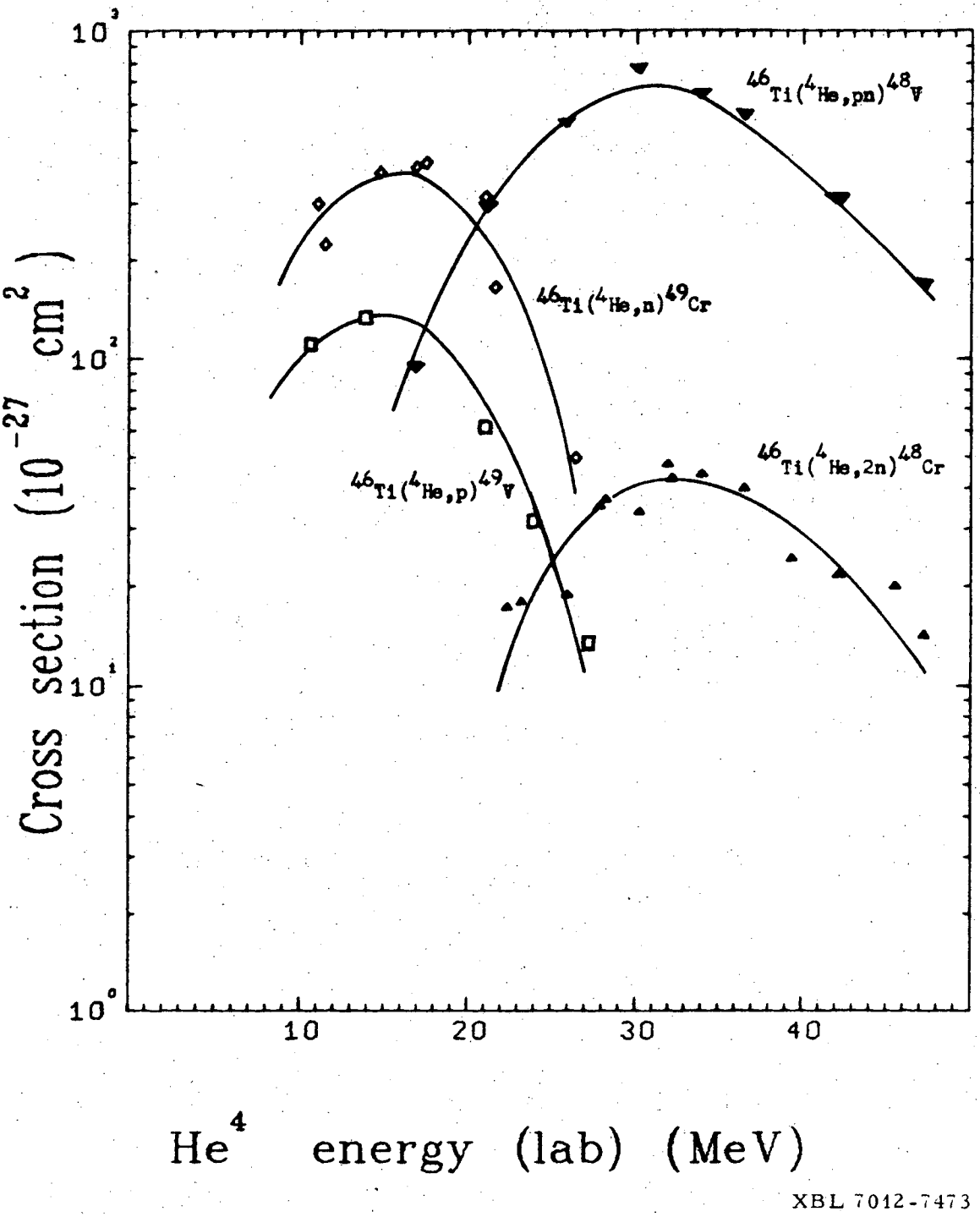

Fig. 8. Experimental excitation functions for reactions from ^{4}He + ^{46}Ti. The solid lines are drawn to aid the eyes only.

The widths of the ^{49}Cr and ^{49}V excitation functions are consistent with that given by the evaporation theory (see Chapter IV).

In spite of the expected suppression of proton evaporation by the Coulomb barrier, the (α,pn) excitation function is much greater than the (α,2n) excitation function. The greater probability for proton emission can be explained by the difference in the level densities of the product nuclei. The (α,pn) product is ^{48}V(odd-odd) which has greater number of available levels than the (α,2n) product nucleus ^{48}Cr(even-even). Therefore, there are more open channels for proton emission than neutron emission, and enhancement of (α,pn) reaction results. The same phenomenon has been observed, by Markowitz, Miller, and Friedlander[50] in $^{4}He + ^{50}Cr$ reactions, and by Porile[51] in $^{4}He + ^{64}Zn$, and by others.[52]

The cross section for (α,n) is greater than that for (α,p) reaction. As expected, proton emission is somewhat inhibited by the Coulomb barrier, when both the product nuclei are odd-A.

Both the excitation functions (α,n) and (α,2n) are directly observed and calculated from gamma ray spectra. For (α,pn) reaction, the contribution of $^{48}Cr \xrightarrow{EC} ^{48}V$ is subtracted from the total ^{48}V activity. This correction is small (less than 10% of the total ^{48}V activity), because the ^{48}Cr production cross section is considerably smaller than the $^{46}Ti(\alpha,pn)^{48}V$ cross section. The details of growth and decay of ^{48}V from the decay of ^{48}Cr is given in Appendix II.

The $^{46}Ti(\alpha,p)^{49}V$ is obtained by measuring the titanium x-rays from ^{49}V electron capture decay. Details of the x-ray calibration is given in Appendix IV. In order to eliminate contribution of Ti x-ray from ^{48}V (16 day half-life) decay, the samples are counted about 3 months

after bombardment. The contribution of ^{49}V activity from $^{49}Cr \xrightarrow{EC} {}^{49}V$ is subtracted from the total ^{49}V radioactivity. However, the contribution from ^{49}Cr decay is very great, because the cross section of $^{46}Ti(\alpha,n)^{49}Cr$ is large. Therefore the uncertainty in the (α,p) cross sections is large.

Contribution of radioactivity from other titanium isotopes in the target is small. The main impurity is $^{48}Ti(14.5\%)$. The excitation functions for $^{48}Ti(\alpha,3n)^{49}Cr$, and $^{48}Ti(\alpha,p2n)^{49}V$ at alpha-particle energies about 20 MeV are very small from reaction Q values considerations. The cross sections for $(\alpha,4n)$ and $(\alpha,p3n)$ should also be negligible at energies less than 50 MeV.

The four excitation functions agree generally (within 20%) with those measured by Raleigh.[53]

2. $^{3}He + {}^{47}Ti$

Figure 9 represents the excitation functions for $^{47}Ti(^{3}He,2n)^{48}Cr$ and $^{47}Ti(^{3}He,pn)^{48}V$. Again the $(^{3}He,pn)$ cross section is considerably greater than the $(^{3}He,2n)$ as seen in the alpha + ^{46}Ti system. The Q value for a single particle evaporation (p or n) is +10.7 MeV and +7.4 MeV, respectively. Therefore, the reaction threshold for these reactions is the Coulomb barrier, and the excitation functions should have peaked and become small at the actual bombarding energies. Because the enriched ^{47}Ti target contains significant amount of $^{48}Ti(16.5\%)$ and the $^{48}Ti(^{3}He,2n)^{49}Cr$ cross section is expected to be considerably greater than that for $^{47}Ti(^{3}He,n)^{49}Cr$ at ^{3}He energies less than 20 MeV, the contribution of ^{49}Cr from ^{48}Ti must be subtracted from the enriched ^{47}Ti experiments. Figure 10 represents the production of ^{49}Cr from enriched

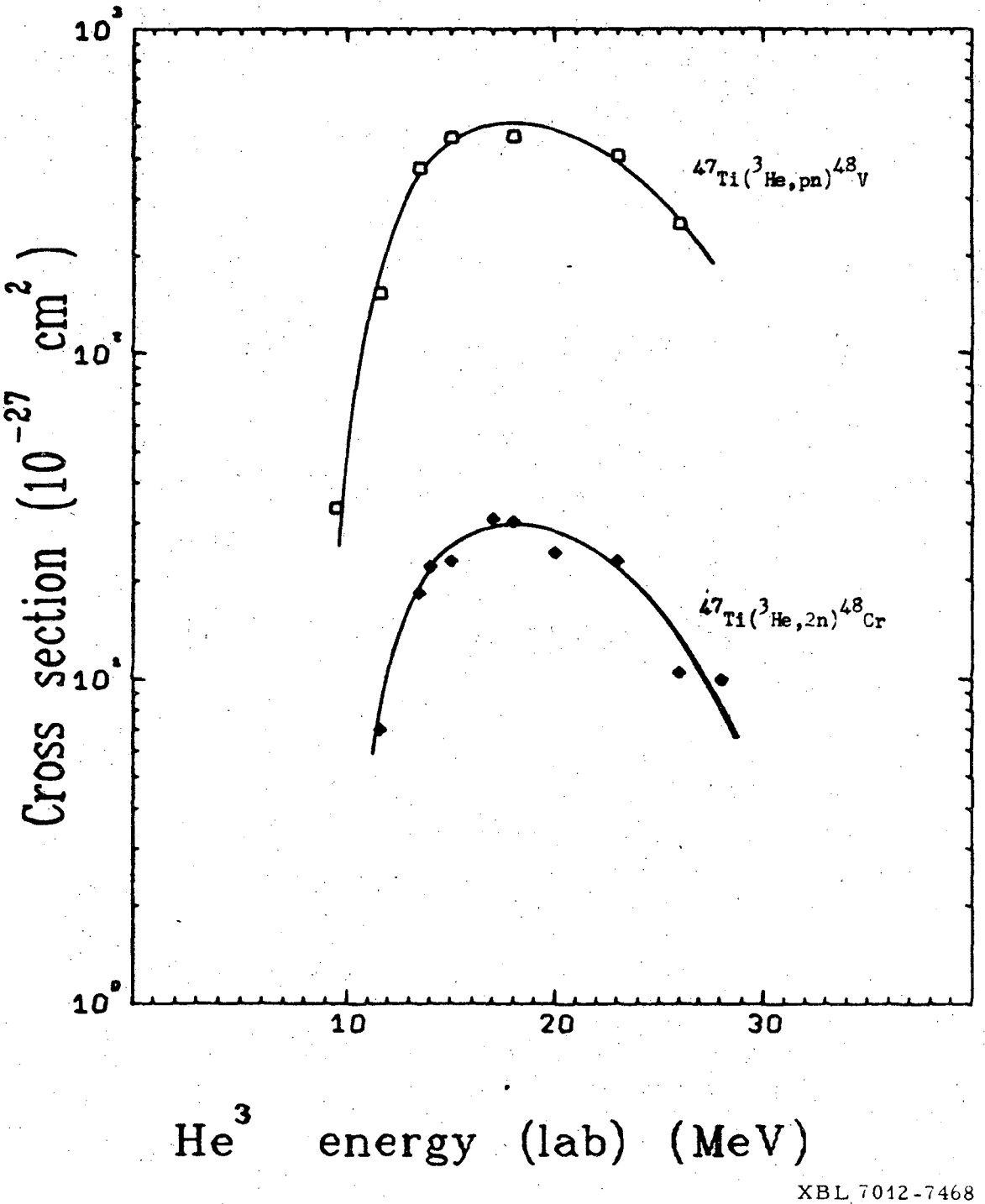

Fig. 9. Experimental excitation functions for the 2n and pn evaporation from ^{3}He + ^{47}Ti reaction.

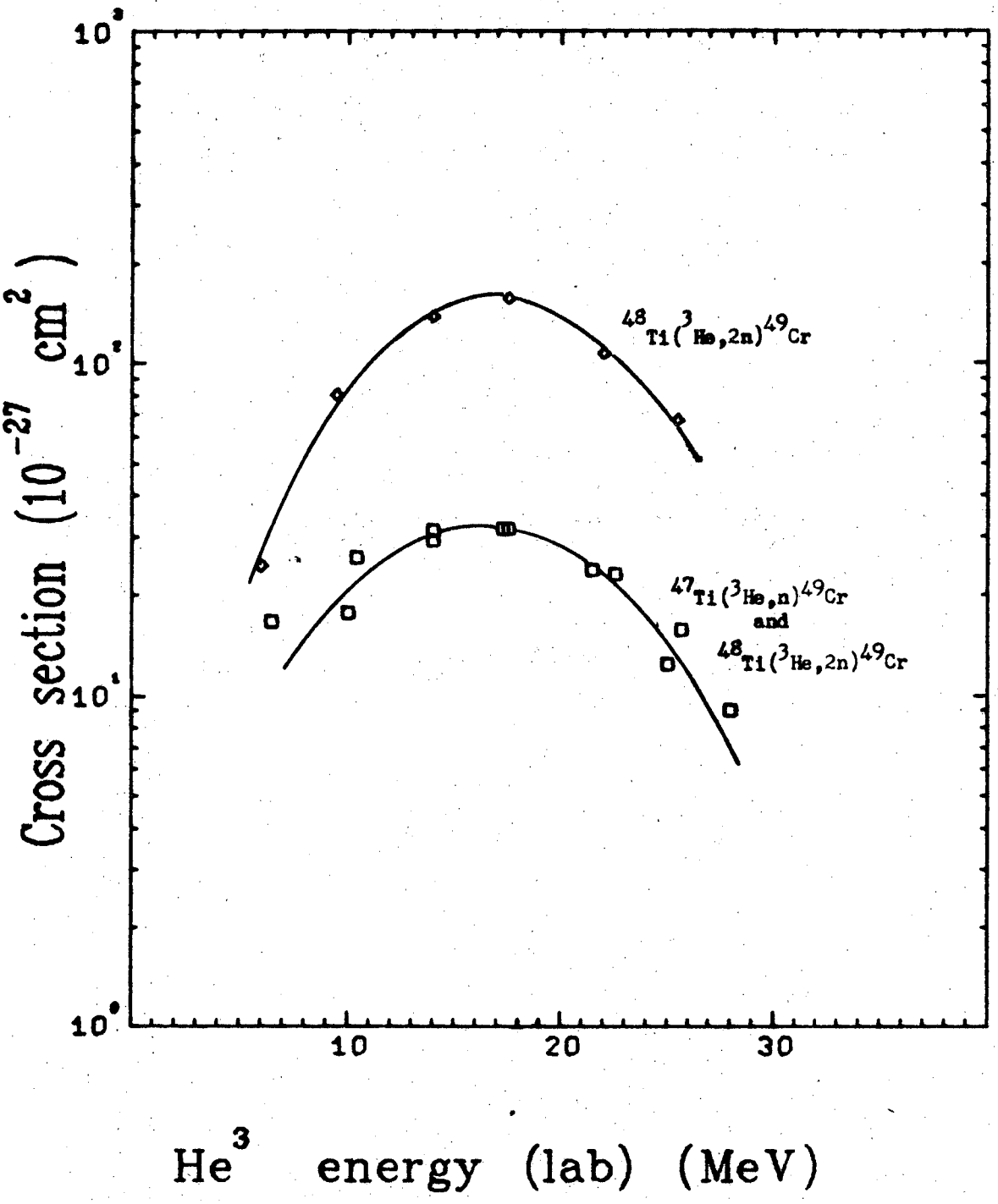

Fig. 10. Excitation functions for ^{48}Ti(^{3}He,2n)^{49}Cr and the sum production of ^{49}Cr from ^{47}Ti and ^{48}Ti with ^{3}He using ^{47}Ti-enriched targets. ^{47}Ti(79.5%) and ^{48}Ti(16.5%).

^{48}Ti targets(99.1% ^{48}Ti) and from the enriched ^{47}Ti targets by ^{3}He bombardment. The "true" ^{47}Ti(^{3}He,n)^{49}Cr excitation function is then obtained by subtracting the ^{49}Cr activity from ^{48}Ti reaction and is shown in Fig. 11. Here, the difference between two big numbers is used, and the uncertainty in ^{47}Ti(^{3}He,n)^{49}Cr cross sections would be large. Nevertheless this (^{3}He,n) cross section is small, as expected, and in Chapter IV, we show that it agrees reasonably with the predictions of the evaporation theory.

The ^{47}Ti(^{3}He,p)^{49}V excitation function is not measured for the following reasons. First, the (^{3}He,p) reaction cross section may be even smaller than the (^{3}He,n) cross section, as indicated in the α + ^{46}Ti case. Secondly, contribution from ^{49}Cr $\xrightarrow{\beta^+, EC}$ ^{49}V will be very great. Thirdly, the interference from ^{48}Ti(^{3}He,pn)^{49}Cr cross section will be very significant. Of course, the measurement of the ^{47}Ti(^{3}He,p)^{49}V excitation function will be feasible if very high enrichment of ^{47}Ti isotope (say, 99+%) is used. Unfortunately isotope ^{47}Ti of such enrichment is not currently available.

3. ^{16}O + ^{34}S

Heavy ion reaction provides a convenient way of forming excited nuclei at high excitation energy and high angular momentum. At incidence energies of about 10 MeV/nucleon, the formation of a compound nucleus is hindered by the high angular momentum.[54,55] Kowalski, Jodogne, and Miller[10] reported that the cross section for complete-fusion reaction actually decreased with increasing energy above 100 MeV for the ^{16}O + ^{27}Al system. However, heavy ion reactions of lower incident energies (< 5 MeV/nucleon) do proceed predominantly via the compound nucleus

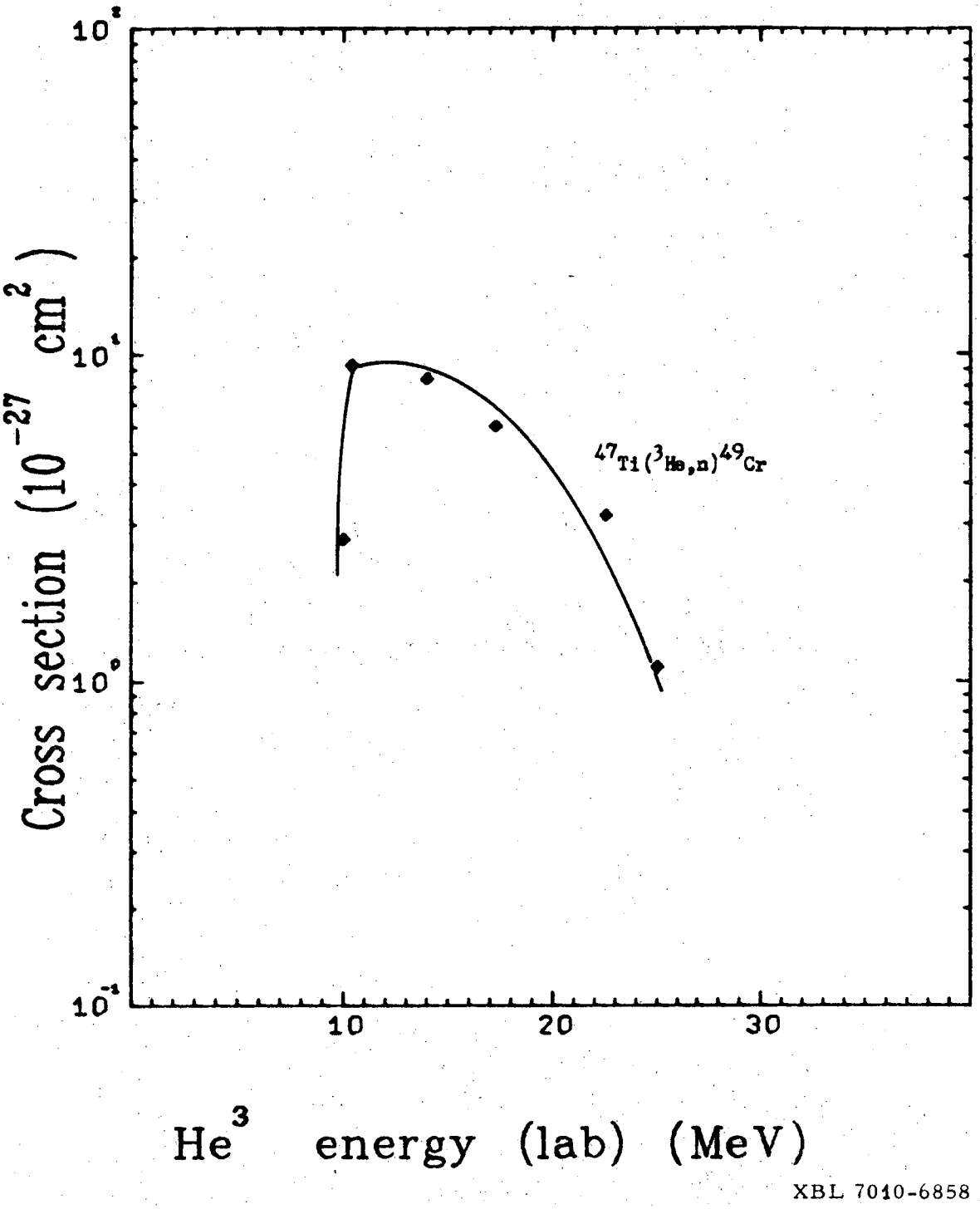

Fig. 11. Excitation function for ^{47}Ti(^{3}He,n)^{49}Cr calculated from the sum production cross section and the ^{48}Ti(^{3}He,2n)^{49}Cr cross section of Fig. 10. The uncertainties in this excitation function is expected to be large.

mechanism.[56] The lower velocity of the ions reduces the probability of knock-on reaction, and the angular momentum is less than the so-called critical angular momentum[57] for compound nucleus formation.

The reactions $^{34}S(^{16}O,n)^{49}Cr$ and $^{34}S(^{16}O,p)^{49}V$ are not observed. The cross section of these reactions are very low because of high Coulomb barrier and positive reaction Q values. At reaction threshold of $^{16}O + ^{34}S$, the excitation energy is about 35 MeV. De-excitation of an excited nucleus of such high excitation energy by evaporation of only a single nucleon is very unlikely.

Figure 12 shows the excitation functions for $^{34}S(^{16}O,2n)^{48}Cr$ and $^{34}S(^{16}O,pn)^{48}V$. The reaction Q values are respectively -7.7 and -5.6 MeV, which are considerably less than the Coulomb barrier (21 MeV) for $^{16}O + ^{34}S$ interaction. The threshold for these reactions is the Coulomb barrier; the steep low-energy edge of the excitation function suggests that this is true.

Again the $(^{16}O,pn)$ cross section is much greater than the corresponding $(^{16}O,2n)$ cross section, as seen in the ^{4}He and ^{3}He reactions. The same phenomenon is also observed in the ^{18}O and ^{22}Ne reaction systems.

The other isotope in the target, $^{32}S(66\%)$, will not interfere with the ^{34}S reaction studied, because $^{32}S + ^{16}O$ produces excited nucleus $^{48}Cr^{*}$, which can not decay to ^{48}Cr and ^{48}V by particle evaporation. The contents of sulfur isotopes ^{33}S and ^{36}S in the target are too low to warrant any further consideration.

4. $^{18}O + ^{32}S$

Observation of the suppression of $^{47}Ti(^{3}He,n)^{49}Cr$ cross section by high Coulomb barrier and positive Q value leads one to expect the

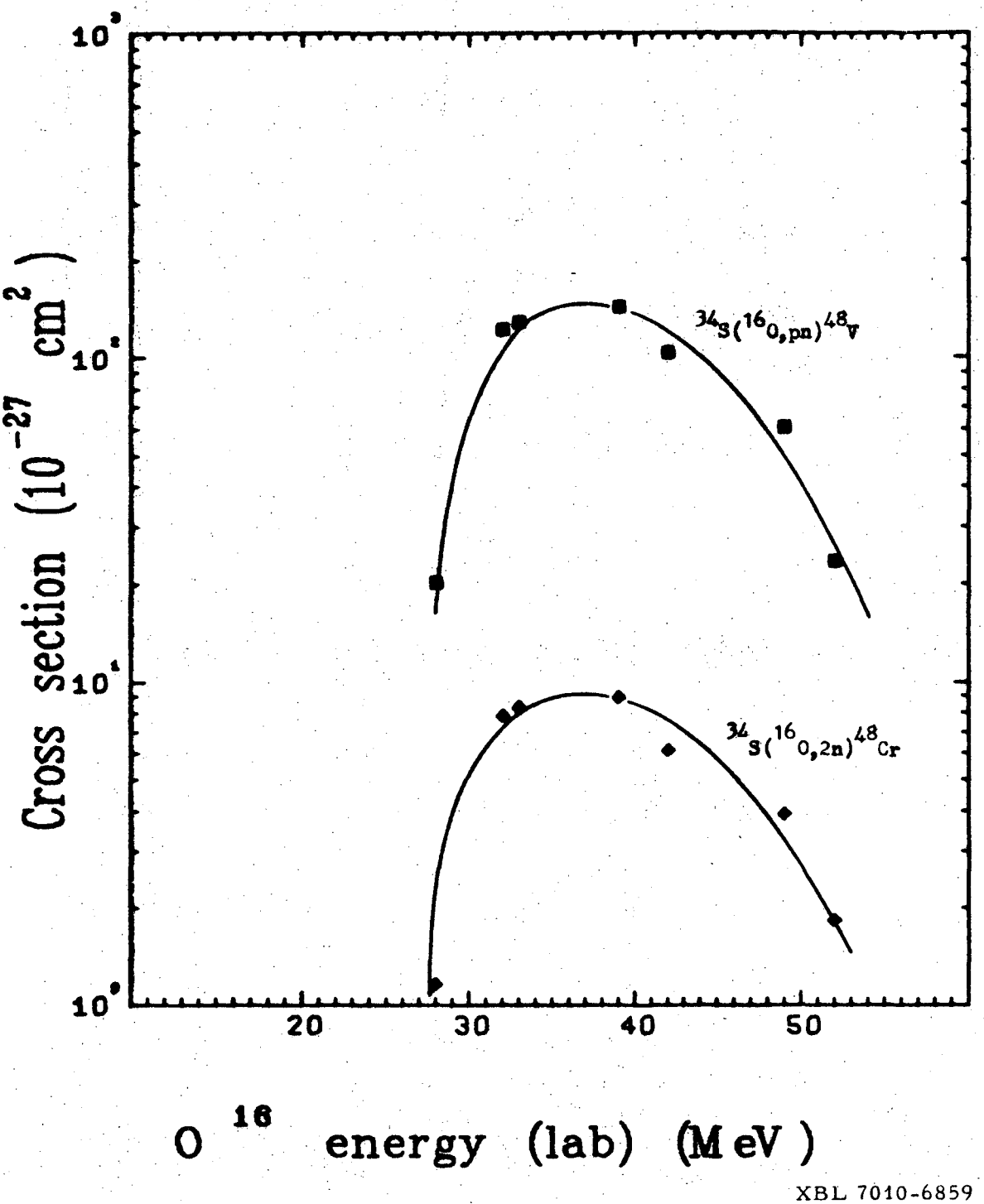

Fig. 12. Experimental cross section for pn and 2n evaporation from $^{16}O + ^{34}S$ reaction. The solid lines are drawn to aid the eyes only.

same suppression of the two-particle evaporation excitation functions at higher excitation energies. The $^{32}S(^{18}O,2n)^{48}Cr$ and $^{32}S(^{18}O,pn)^{48}V$ reaction Q values are somewhat positive and the Coulomb barrier (21 MeV) is about equal to that of the $^{16}O + ^{34}S$ system. At the reaction threshold, the excitation energy is about 44 MeV. The two particle excitation functions are expected to have peaked and become small. This is indicated by the relatively much smaller cross sections and less steepness at the low-energy edge when compared with the excitation functions of the $^{16}O + ^{34}S$ system. Figure 13 shows the $^{32}S(^{18}O,pn)^{48}V$ and $^{32}S(^{18}O,2n)^{48}Cr$ excitation functions. The magnitude of these excitation functions is about a factor of 4 lower than the corresponding ^{16}O excitation functions. The peaks of the ^{18}O reaction cross sections should not be considered as "natural" ones ("natural peak" is due to the competition of different de-excitation channels). These peaks probably show the effect of the decreasing probability of two particles evaporation and the increasing penetration of the Coulomb barrier as bombardment energy increases. These $^{18}O + ^{32}S$ two-particle evaporation cross sections can be regarded as a measurement of the probability for the emission of protons or neutrons with high kinetic energy.

Natural sulfur is used as the target. The ^{34}S isotope should not interfere with the ^{32}S reactions at the excitation energies studied; the isotope ratio of ^{32}S : ^{34}S is 22.5 : 1, and the ^{34}S is two mass numbers away.

5. $^{22}Ne + ^{28}Si$

The Q value of this reaction system is lower than the $^{18}O + ^{32}S$ system; however, the Coulomb barrier (23 MeV) is higher. Similar suppression

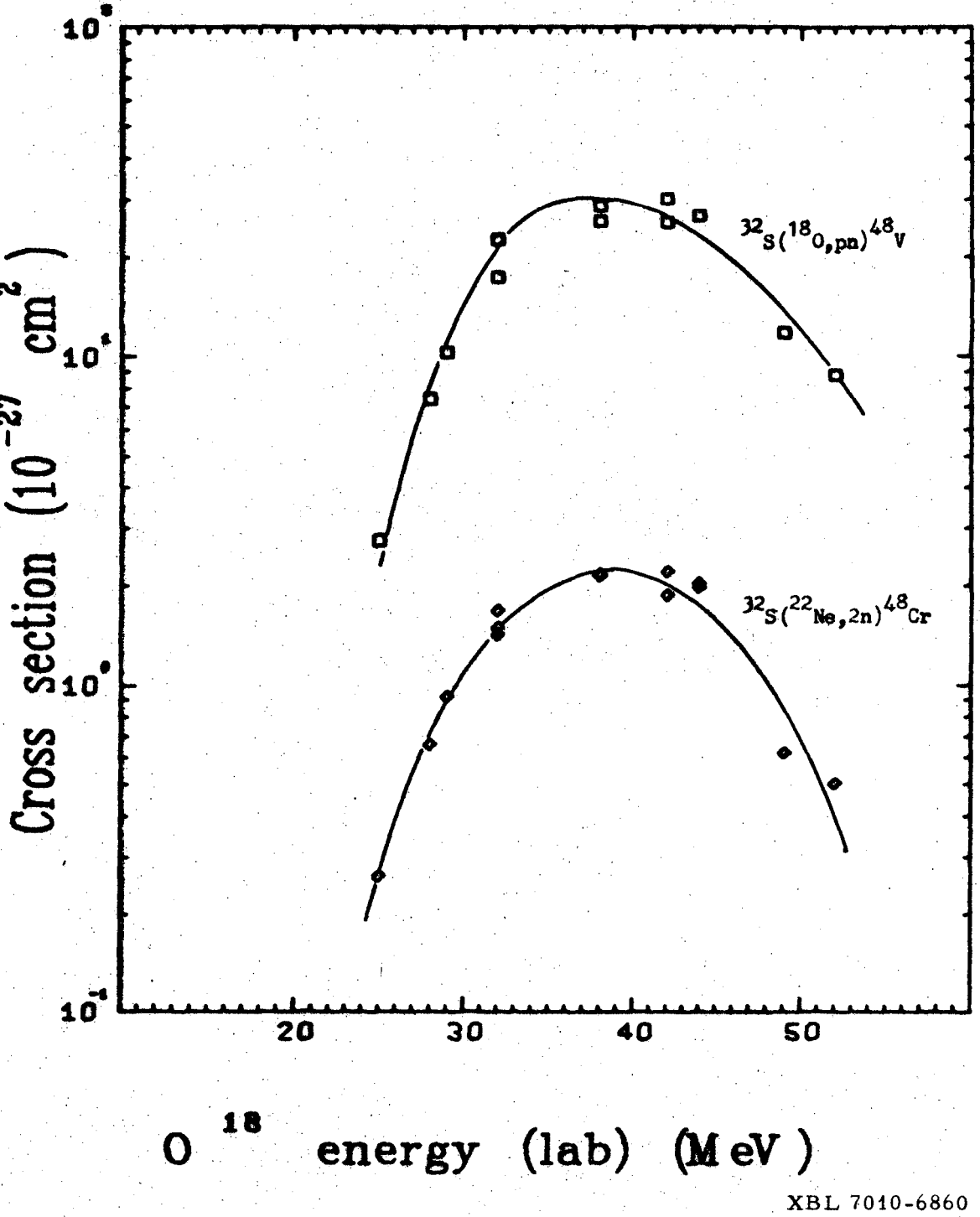

Fig. 13. Experimental cross sections for pn and 2n emission from $^{18}O + ^{32}S$ reaction.

effects should be observable for the $^{28}Si(^{22}Ne,pn)^{48}V$ and the $^{28}Si(^{22}Ne,2n)^{48}Cr$ excitation functions. Indeed, Fig. 14 shows these cross sections have the same magnitude as the ^{18}O reaction cross sections.

The existence of the high energy "tail" in the excitation functions deserves some comment. As pointed out earlier, interaction through a knock-on type of mechanism is not probable, in view of the low incident particle velocity (in this case, the velocity is equal to that which a nucleon would have at about 2 MeV, or at 2×10^9 cm/sec). The target contains ^{29}Si(4.7%), the reaction cross sections for $^{29}Si(^{22}Ne,p2n)^{48}V$ and $^{29}Si(^{22}Ne,3n)^{48}Cr$ may be appreciable at such excitation energies. Therefore, the high energy "tail" of the excitation function is probably due to the contribution from ^{29}Si.

The ratio of the cross sections (^{22}Ne,pn) to (^{22}Ne,2n) is again similar to that of all other reaction pairs studied in this work.

B. Error Estimates

1. Errors in Determination of Beam Energy

The initial uncertainty for beam energy from the Hilac[34] is about ±2%. The 88-inch cyclotron[33] beam is essentially monoenergetic (±0.14%). Because no direct measurement of the beam energy is made, an estimation of ±2% is taken as an upper limit of the uncertainty in true beam energy.

As the ion beam passes through the degrader and target materials, the energy spread in the beam will increase. McIntyre et al.[58] show that the energy straggling due to degradation increases as the stopping power increases. Becker et al.[59] show that the error spread for 145-MeV ^{14}N

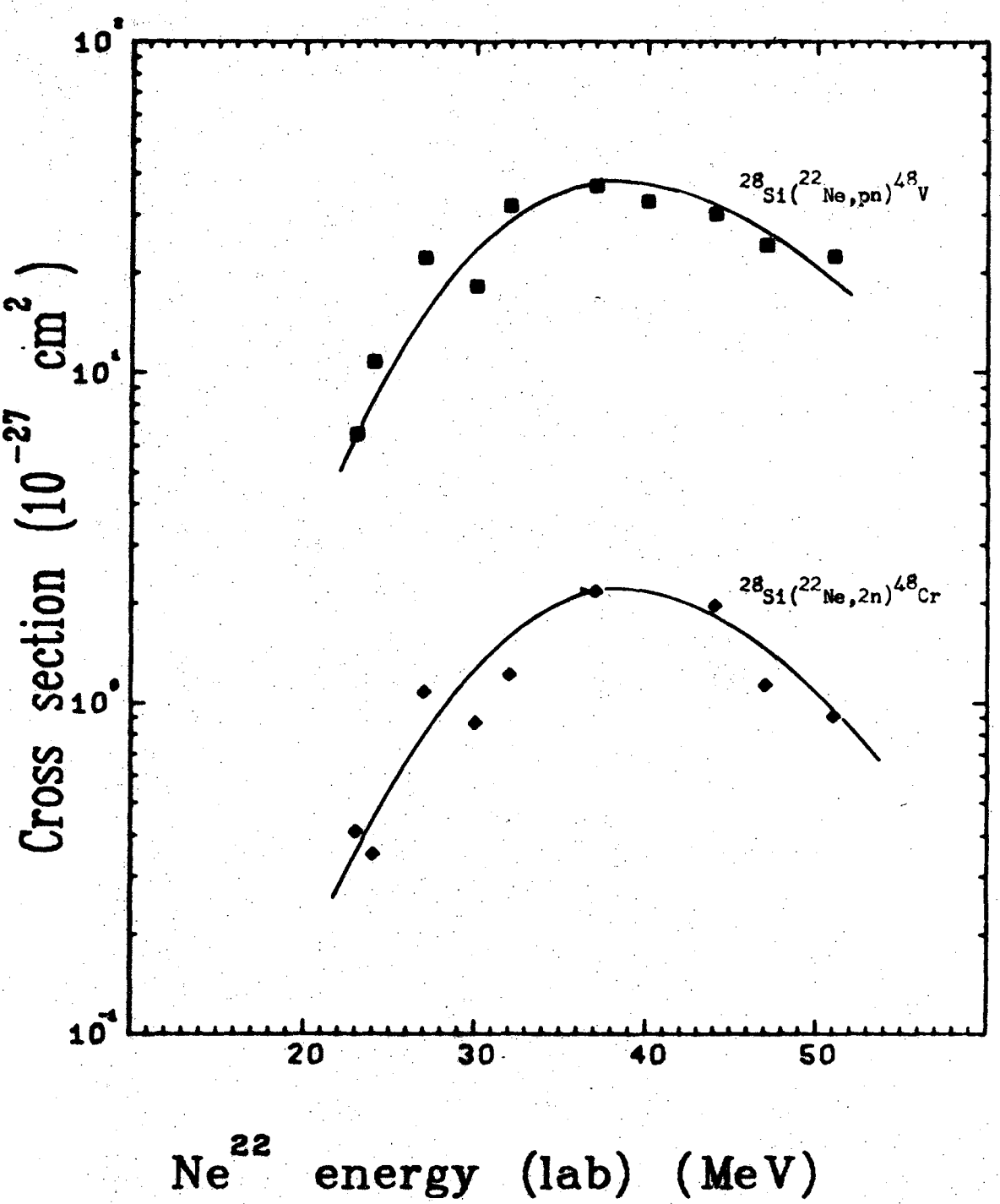

Fig. 14. Experimental excitation functions for the pn and 2n cross sections from ^{22}Ne + ^{28}Si reaction.

beam after degradation to 36 MeV is 4.5 MeV (full width at half maximum, FWHM), with the initial 1.5-MeV beam-spread, and about 2 MeV spread due to non-uniformity in the degrading aluminum foils used. This is consistent with our estimate that for the lower-energy portion of the heavy ion beam, the uncertainty in beam energy could be as large as 5 MeV.

The error introduced by the uncertainty of the range-energy curves is expected to be small, because only the differences in the ranges are used. In summary, the beam energy determination for ^{3}He and ^{4}He particles should be accurate to within 3%; for heavy ions, the uncertainties are from 3% to 15% for high and low-energy portions of the bombardment, respectively.

2. Errors in Determination of Absolute Cross Sections

There are many sources of error that can introduce uncertainty into the determination of absolute reaction cross sections. The particle intensity was measured using a conventional Faraday cup-electrometer method. The integrating electrometer could be read to within ±1% or better, and an occasional calibration of the electrometer with a 1.0186 V Weston standard cell showed that the charge collection efficiency of the Faraday cup is within 1% of the expected value. The charge-to-mass ratio of the heavy ion is given by the strength of the rf field gradient in the poststripper.[34] Therefore, the number of particles passing through the target should be known to ±1%. The percent errors are standard deviations.

As mentioned before, the uncertainty in the evaporated target is better than ±3%. For the sulfur targets, examination under microscope show some unevenness, however the unevenness is regularly distributed

throughout the whole deposit, and sometimes a wobbled ion beam is used to further minimize the non-uniformity in the target. It is felt, therefore, that the "uniformity" of the sulfur targets is also about ±3%.

Statistical errors introduced by the analysis of gamma ray spectra varied with the photopeak to background ratio. When the peak to background ratio exceeds 1.4, the error[47] is less than ±1%; however when the peak to background ratio is only 1.14, the error is ±7%. For γ-ray energies greater than 0.511 MeV (the β^+ annihilation radiation), the background is generally low, and the error in the photopeak analysis should be less than ±2%. For measurements of the ^{49}Cr and ^{48}Cr radioactivities, the energies of the photopeaks are from 0.06 to 0.32 MeV. Because of the β^+ annihilation radiation from many reaction products (contribution also came from the aluminum backing), the photopeak to background ratio of γ-rays in this energy region is of the order of 1.2, analysis error of about ±7% is expected. For x-ray spectra analysis, the background is generally low and an error of less than ±5% is expected.

The γ-ray efficiency calibration from the 1% γ-ray standards (see Appendix III) should be good to within 2 to 2.5%. The error from decay curve analysis should be less than ±2%, because the γ-rays are of the single component type.

There are statistical errors in the counting of radioactivity. Lamb[60] has estimated the photopeak and decay curve analysis errors to be within 10%. Errors in weighing, time measurements, and decay scheme corrections are expected to be very small.

In view of the above discussion, the errors in most of the excitation functions measured should be less than 15%.

Two excitation functions are expected to have larger errors because the differences of two large numbers are used. These are $^{47}Ti(^{3}He,n)^{49}Cr$ and $^{47}Ti(^{3}He,p)^{49}V$. It is felt, however, the relative cross sections at different energies for these two excitation functions should be accurate to within 15%.

The reproducibility of the excitation functions is generally good. The determinations of cross sections from different runs agreed with one another within the error limits. In the case of ^{4}He bombardments, the determinations using different accelerators were also within the error limits.

IV. THEORETICAL CONSIDERATIONS

The significance of the excitation functions measured in this work rests upon the interpretation of these cross sections using some convenient model. In this chapter, predictions of the compound-nucleus and evaporation theory are compared with experiment. Effects of reaction Q values and the Coulomb barrier upon nuclear reactions are noted. Comparison of excitation functions in light of the independence postulate is also made. Effects of angular momentum on the decay of the compound nucleus are discussed. It is hoped that from these considerations, we gain some insight into nuclear reactions in this region of mass and excitation energy.

A. Calculation of Excitation Functions

Nuclear reactions for medium-weight nuclei ($45 < A < 100$) at energies up to 10 MeV per incident nucleon have been successfully described by the statistical theory.[4] The main feature of this theory is that a compound nucleus is formed during a nuclear reaction and the subsequent decay of this compound nucleus can be treated statistically. Schematically the reaction of the incident particle a with the target nucleus A to yield the product nucleus B and the outgoing particle b can be represented as

$$a + A \rightarrow C^* \rightarrow b + B \quad , \tag{2}$$

where C^* is the compound nucleus. Independence postulate[1] allows the cross section for such a reaction to be written as

$$\sigma(a,b) = \sigma_C(\in_a)\ W_b'(U) / \sum_j W_j(U) \quad , \tag{3}$$

where $\sigma_C(\epsilon_a)$ is the cross section for the formation of the compound nucleus with ϵ_a as the kinetic energy of the incident particle a, $W_b'(U)$ is the probability per unit time that only b is emitted from the compound nucleus with excitation energy U, and the summation over j includes all particles that can be evaporated.

Weisskopf[2] has shown that the probability per unit time for evaporating a particle j with kinetic energy between ϵ and $\epsilon + d\epsilon$ is

$$P_j(\epsilon)\, d\epsilon = \frac{g_j m_j}{\pi^2 \hbar^3} \sigma(\epsilon) \frac{\rho_f}{\rho_i} \epsilon\, d\epsilon \quad , \tag{4}$$

where g_j is the statistical weight of particle j, m_j is the reduced mass of the system, $\sigma(\epsilon)$ is the inverse cross section for the evaporation process, and ρ_i, ρ_f are the level densities of the initial and final nuclei.

The statistical weight of particle j is calculated by

$$g_j = 2s + 1 \quad , \tag{5}$$

where s is the intrinsic spin of particle j.

There are many approximate methods for evaluating the level density. The Fermi gas model is usually employed. The Fermi gas model which assumes the one-Fermion level to be equally spaced[61] gives a level density:

$$\rho(U) = \frac{1}{12} \pi^{1/2} a^{-1/4} (U + t)^{-5/4} \exp(2\sqrt{aU}) \quad , \tag{6}$$

where U is the excitation energy, t is the thermodynamic temperature, and a is the level density parameter. The thermodynamic temperature is related to the excitation energy as:

$$U = a\,t^2 - t \quad . \tag{7}$$

From a consideration of the Fermi gas model, the level density parameter a can be calculated by

$$a = \frac{1}{6}\,\pi^2(g_n + g_p) \quad , \tag{8}$$

where g_n and g_p are the single neutron and proton level densities at the Fermi energy respectively. More explicitly the parameter a is given by[15]

$$a = r_o^2\,\frac{A^{2/3}(Z^{1/3} + N^{1/3})}{29.2}\,(\mathrm{MeV})^{-1} \quad , \tag{9}$$

where r_o is the nuclear radius parameter in units of 10^{-13} cm, Z and N are the proton and neutron numbers respectively, and A = Z + N. If we take an approximation that $Z^{1/3} = N^{1/3}$, the parameter a is then

$$a = \frac{A}{20} \quad \text{for} \quad r_o = 1.2 \text{ fm} \tag{10a}$$

or

$$a = \frac{A}{13} \quad \text{for} \quad r_o = 1.5 \text{ fm} \quad . \tag{10b}$$

For convenience, the level density equation (Eq. (6)) is further approximated. The slow dependence of the level density upon the excitation

energy in the pre-exponential term is taken to be constant for high excitation energy and over a small mass region. The level density at excitation energy U is then given by

$$\rho(U) = C \exp(2\sqrt{aU}) \quad , \tag{11}$$

where C is a constant.

The effect of nuclear pairing on the level density must be taken into account. Hurwitz and Bethe[62] pointed out the effect of odd-even nuclei upon the level density should be taken as a displacement of the ground-state energy caused by the pairing of the nucleons. Ericson[63] showed the correctness of this treatment by the level counting experiment. An energy, δ, must be subtracted from the excitation energy. For odd-odd nuclei, δ is taken to be zero, and for all other types, $\delta > 0$. The level density is then

$$\rho(U) = C \exp\{(4a[U - \delta])^{1/2}\} \quad . \tag{12}$$

The consideration of effect of the closed shell on level density is ignored because the nuclei used in this work do not fall into a closed shell. The δ values are taken directly from Cameron.[64] In even-even nuclei, the δ values were considered to be additive. For the ^{48}Cr nucleus ($Z = N$), an additional 3 MeV is added to δ. This follows from the argument of de-Shalit as given by Dostrovsky et al.[65] The transition probability of the excited nucleus to the pure isotopic spin ($T = 0$) state in ^{48}Cr is very small and thus evaporation of neutrons can only lead to, in first approximation, the states in ^{48}Cr with $T \neq 0$. The first of such $T \neq 0$ states is estimated to be about 3 MeV above the ground-state.

The probability per unit time for evaporating a particle j with kinetic energy between ϵ and $\epsilon + d\epsilon$ can be written more explicitly by

$$P_j(\epsilon)\, d\epsilon = \frac{g_j m_j}{\pi^2 \hbar^3 \rho_i}\, \sigma(\epsilon)\, C \exp\{2[a(U - S_j - \delta_j - \epsilon_j)]^{1/2}\}\, \epsilon_j d\epsilon_j \quad , \qquad (13)$$

where S_j is the separation energy of the j particle from the compound nucleus, and the other symbols are the same as in the previous equations.

The inverse cross section is usually taken as the capture cross section for the product nucleus. Dudey et al.[66] showed that the inverse cross sections do not differ significantly from the reactions with the ground state for ^{59}Co production from α or p reactions with Fe or Ni. The empirical equations from Dostrovsky et al.[65] were used for the reaction cross sections. For neutrons, the capture cross section (σ_c) is

$$\sigma_c = \sigma_g\, \alpha\left(1 + \frac{\beta}{\epsilon}\right) \quad , \qquad (14)$$

where $\sigma_g = \pi R^2$ is the geometric cross section, $\alpha = 0.76 + 2.2\, A^{-1/3}$ and $\beta = (2.12\, A^{-2/3} - 0.05)/(0.76 + 2.2\, A^{-1/3})$, A is the mass number, and $R = 1.5\, A^{1/3}$ fm is the nuclear radius. For charged particles, the capture cross section is

$$\sigma_c = \sigma_g(1 + C_j)\,(1 - k_j V_j/\epsilon) \quad . \qquad (15)$$

The symbols C_j and k_j are constants for the charged particle j. The parameters C_j and k_j are interpolated from the values given by Dostrovsky et al.[65] and are shown in Table IV. The symbol V_j in Eq. (15) is the classical Coulomb barrier and can be calculated with the formula

Table IV. Parameters used for inverse or total reaction cross section calculations[a]

Z	k_p	c_p	k_α	c_α	k_d	c_d	$k_{^3He}$	$c_{^3He}$
23	0.61	0.25	0.86	0.10	0.67	0.12	0.80	0.13
22	0.60	0.26	0.85	0.10	0.66	0.13	0.79	0.13
21	0.59	0.27	0.84	0.10	0.65	0.14	0.78	0.13
20	0.58	0.28	0.82	0.10	0.64	0.14	0.76	0.13

[a]The values of the parameters are derived from Dostrovsky et al. (Ref. 65).

$$V_j = \frac{Z_1 Z_2 e^2}{r_o A^{1/3} + r_j} \quad , \tag{16}$$

where Z_1 and Z_2 are the atomic charges of the outgoing and the residual nucleus, e is the electron charge; and r_o = 1.5 fm. The value of r_j was taken to be 1.2 fm for deuterons and ^{3}He and α particles, and zero for protons.

For charged particles emitted with kinetic energy less than 1.8 times the Coulomb barrier, the cross section was calculated by an interpolation of Shapiro's table of reaction cross sections,[67] using $r_o = 1.5 \times 10^{-13}$ cm.

The total probability of evaporating a single particle b can be written as an integration of Eq. (4) over all the possible emission energies,

$$W_b(U) = \frac{g_b m_b}{\pi^2 \hbar^3 \rho_i} \int_0^{U-S_b-\delta_b} C\, \sigma(\epsilon)\, \exp\{2[a(U-S_b-\delta_b-\epsilon_b)]^{1/2}\}\, \epsilon_b d\epsilon_b \, . \tag{17}$$

The integral in this equation takes into account all particles b emitted leaving the residual nucleus in excited levels down to the "displaced level". The decay of the compound nucleus to levels below the "displaced level" is ignored. This is a reasonable approximation, because the level density of the residual nucleus with excitation energy less than δ is expected to be small. Furthermore, in calculating the specific excitation functions, only the ratios of the evaporation probabilities are used and thus the errors introduced in this approximation tend to cancel each other.

Equation (17) gives the total probability for the evaporation of particle b from the compound nucleus with excitation energy U. In order to calculate the reaction cross section for single particle evaporation, the equation must be modified so that after one particle evaporation, no other particle could be emitted (except, of course, photons). This requires that after one-particle emission, the residual nucleus must have excitation energy insufficient for the evaporation of another particle. Therefore the evaporation of particle b with kinetic energy lower than $U-S_b-S_2$ should not be included in the calculation of the single particle emission cross section. S_2 is the evaporation energy (defined below) of the most loosely bond particle after the evaporation of b. The evaporation energy S_2 is given by

$$S_2 = B_2 + \delta_2 + K_2 \quad , \tag{18}$$

where B_2 is the binding energy of particle 2 in the residual nucleus, and δ_2 is the δ value after particle 2 is also evaporated; and K_2 is the effective Coulomb barrier of particle 2. $K_2 = 0$ for neutrons and $K_2 = 1.5$ MeV for protons. Because of the rapid decrease of the excitation energy after the first evaporation, only protons or neutrons are considered for the second emission.

The cross section of the reaction given by Eq. (2) can then be expressed explicitly as

$$\sigma(a,b) = \sigma_c(\epsilon_a) g_b m_b \int_A^{U-S_b-\delta_b} \sigma(\epsilon_b) \exp\{2[a(U-S_b-\delta_b-\epsilon_b)]^{1/2}\} \epsilon_b d\epsilon_b$$

$$\Big/ \sum_j g_b m_b \int_0^{U-S_b-\delta_j} \sigma(\epsilon_j) \exp\{2[a(U-S_j-\delta_j-\epsilon_j)]^{1/2}\} \epsilon_j d\epsilon_j \quad , \qquad (19)$$

where $A = U - S_b - S_2$ (if $U - S_b - S_2 < 0$, $A = 0$). For a simple calculation the summation is taken over neutrons, protons and α-particles only. The evaporations of ^3He, d, and ^3H are very rare[65] and are neglected in this calculation.

The separation energies are taken directly from a calculation by Seeger[68] and are summarized in Table V.

For the evaporation of two particles, the residual nucleus after one-particle evaporation is taken as the starting point. The following equations apply

$$\sigma(a,bc) = \sigma_C(\epsilon_a) \int_0^{U-S_b-S_c} P_b(\epsilon_b) W_C'(\epsilon_b) d\epsilon_b \Big/ \sum_j \int_0^{U-S_j} P_j(\epsilon_j) d\epsilon_j \quad , \qquad (20a)$$

$$W_c'(\epsilon_b) = \int_B^{U-S_b-S_c-\epsilon_b} P_c(\epsilon_c) d\epsilon_c \Big/ \sum_k \int_0^{U-S_b-S_k-\epsilon_b} P_k(\epsilon_k) d\epsilon_k \quad , \qquad (20b)$$

where $B = U - S_b - S_c - \epsilon_b - S_3$ (if $U - S_b - S_c - \epsilon_b - S_3 < 0$, $B = 0$). S_c is the separation energy of the second particle, c; S_3 is the evaporation energy of the most loosely bond particle after the emission of b and c. $P_j(\epsilon_j)d\epsilon_j$ is the probability for evaporation of particle j, given by Eq. (13).

Equations (19) and (20) were programmed for computation on the CDC 6600 computer. This program for the decay of compound nucleus completely ignored the effects of angular momentum.

Table V. Separation energies and values of δ for the calculation of excitation functions.

Excited nucleus	Emitted particle	S_b[a] (MeV)	δ_b[b] (MeV)	S_2(or S_3) (MeV)
^{50}Cr	n	12.83	1.44	10.0
	p	9.26	1.29	11.7
	α	8.28	3.14	12.9
^{49}Cr	n	10.38	5.85	10.7
	p	8.52	0.	11.0
	α	8.24	1.73	--[c]
^{49}V	n	12.10	0.0	11.0
	p	7.20	3.02	13.06
	α	9.03	1.41	--
^{48}Cr	n	15.77	1.44	--
	p	7.76	1.41	--
^{48}V	n	9.61	1.41	--
	p	6.43	1.73	--
^{46}Ti	n	12.78	1.73	--
	p	10.0	1.41	--

[a] The separation energies are based on Seeger (Ref. 68).

[b] δ values are from Cameron (Ref. 64). For N = Z, 3 MeV has been added.

[c] When no value is given, that quantity is not needed in the calculation.

As suggested by Grover,[19,69] the neglect of angular momentum and the competition of γ-ray emission with particle emission causes the low value of the level density parameter, a. Following Chen and Miller,[24] this parameter is taken to be $\frac{A}{25} \cong 2\ \text{MeV}^{-1}$.

For the reactions $^{3}He + ^{47}Ti$ and $^{4}He + ^{46}Ti$, the angular momentum of the reacting systems is not very high (see Sec. D), and thus explicit consideration of the angular momentum effect can be ignored. The results of the calculated excitation functions for $^{46}Ti(\alpha,n)^{49}Cr$, $^{46}Ti(\alpha,p)^{49}V$, $^{46}Ti(\alpha,2n)^{48}Cr$, $^{46}Ti(\alpha,pn)^{48}V$, $^{47}Ti(^{3}He,2n)^{48}Cr$, $^{47}Ti(^{3}He,pn)^{48}V$, and $^{47}Ti(^{3}He,n)^{49}Cr$ are compared with experiment in Figs. 15 to 17.

Because of the low binding energy of the ^{3}He particles, 2.57 MeV per nucleon, direct interaction mechanism might be important at the experimental energies. The possible reactions are

(1) $^{3}He + ^{47}Ti \longrightarrow ^{48}Cr + d$

or $^{3}He \longrightarrow$ "p" + d, Q = -5.49 MeV;

(2) $^{3}He + ^{47}Ti \longrightarrow ^{49}Cr + n$

or $^{3}He \longrightarrow$ "2p" + n, Q = -7.72 MeV;

(3) $^{3}He + ^{47}Ti \longrightarrow ^{49}V + p$

or $^{3}He \longrightarrow$ "d" + p, Q = -5.49 MeV;

(4) $^{3}He + ^{47}Ti \longrightarrow ^{46}Ti + ^{4}He$

or $^{3}He +$ "n" $\longrightarrow ^{4}He$, Q = +18.6 MeV.

Reactions (1) through (3) are stripping reactions, and reaction (4) is a pick up reaction. The reactions (3) and (4) are not observed in this work.

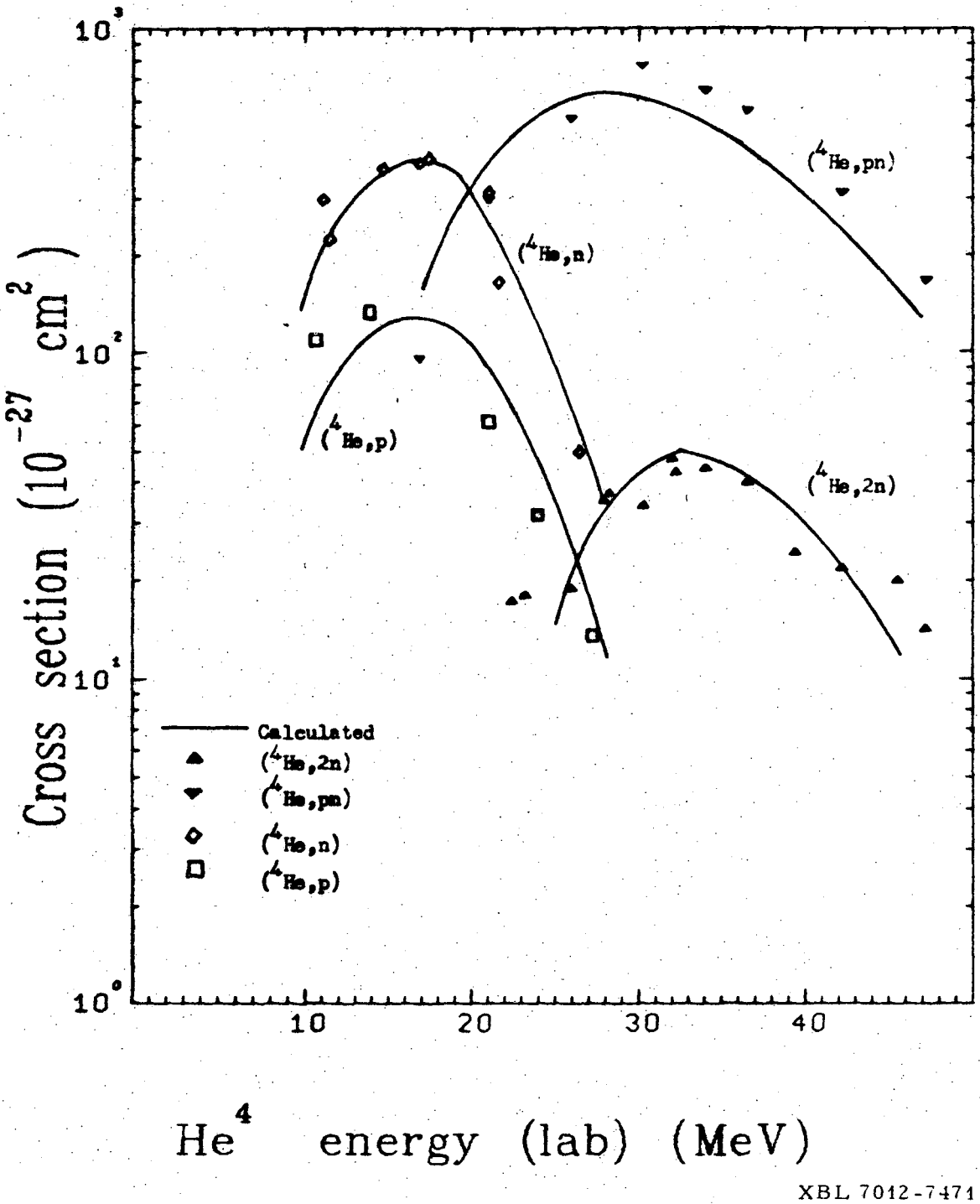

Fig. 15. Comparison of experimental and calculated excitation functions for ^{4}He + ^{46}Ti reactions. The solid lines are calculated, and the points are experimental results.

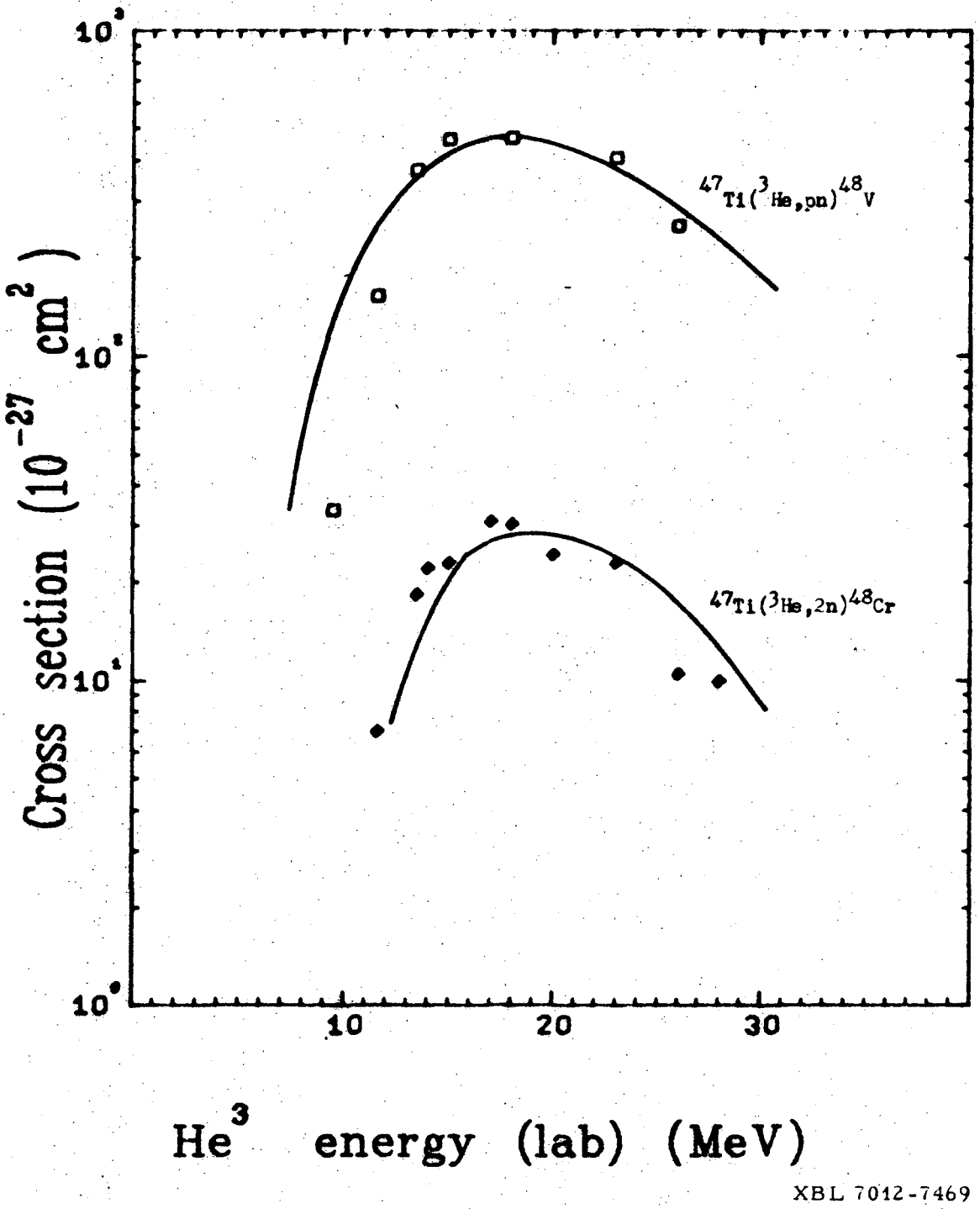

XBL 7012-7469

Fig. 16. Comparison of experimental and calculated excitation functions for ^{47}Ti(^{3}He,pn)^{48}V and ^{47}Ti(^{3}He,2n)^{48}Cr. The points are experimental results, and the solid lines are calculated.

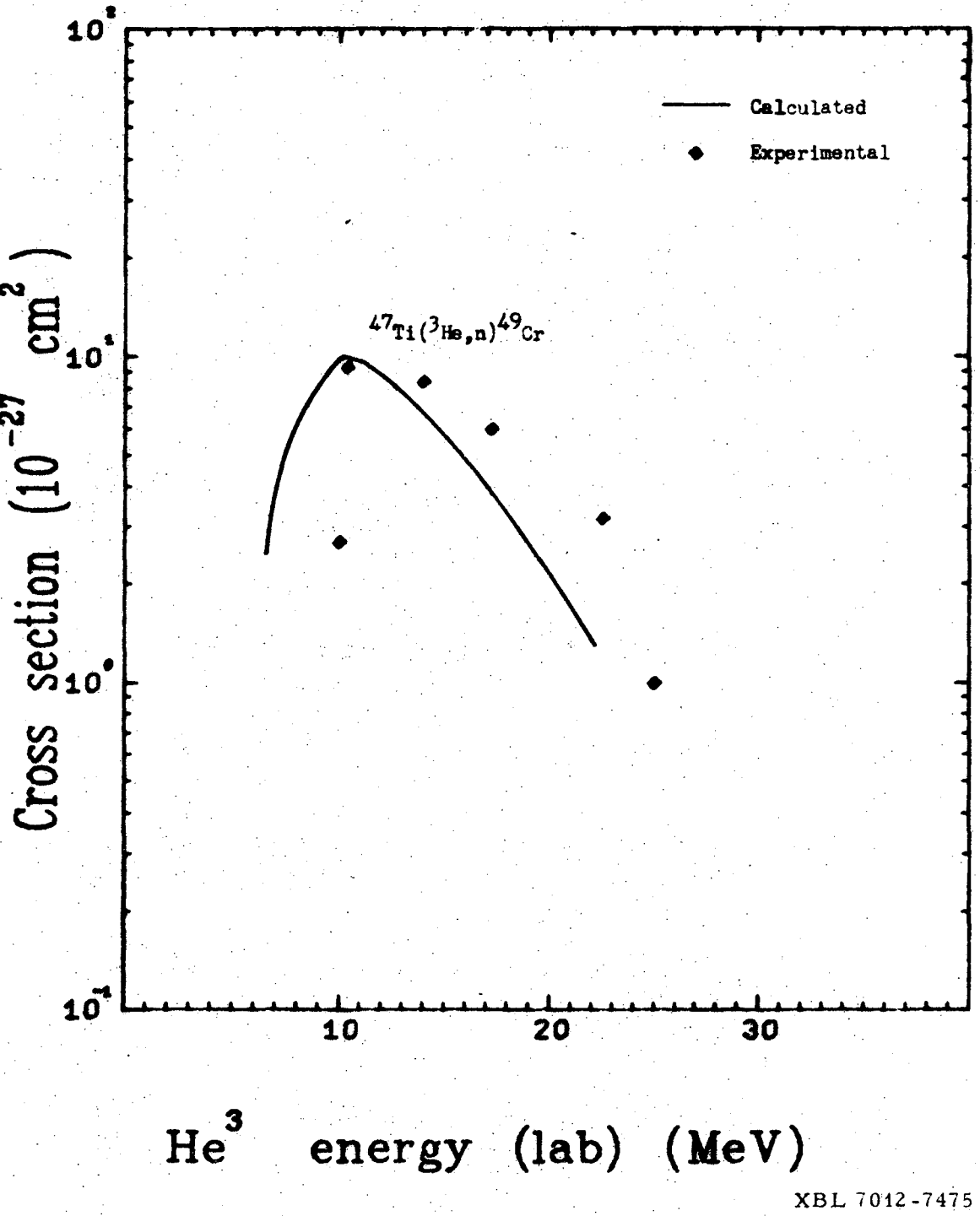

Fig. 17. Comparison of experimental and calculated excitation functions for $^{47}Ti(^{3}He,n)^{49}Cr$.

As seen from the ^{3}He reaction cross sections, the contribution from the stripping reactions is small. In comparison, Chen and Miller[24] observed significant contributions of stripping reactions to the reaction d ⟶ "p" + "n" has a Q value of only -2.23 MeV. The decrease of Q values for the breaking up of ^{3}He tends to reduce the contribution of stripping reactions at the energy region of this work.

The binding energy of ^{4}He particles is 7.1 MeV/nucleon. Therefore, for the ^{4}He + ^{46}Ti reactions, the contribution of stripping reactions is expected to be much smaller than that for the ^{3}He reactions.

The experimental excitation functions generally agree well with the theoretical calculations. For the $^{47}Ti(^{3}He,n)^{49}Cr$ reaction, the agreement is not very good. However, as mentioned before, the determination of this excitation function involves the difference of two large numbers and the uncertainty is thus quite large. Furthermore, the calculation of this excitation function is very sensitive to the value S_2, the energy at which the evaporation of a second particle begins. Nevertheless, the calculated and experimental excitation function does have the same shape and the same magnitude; and the fit is considered reasonable.

Admittedly, the calculation performed is only very approximate. There are many shortcomings in it. First of all, the inverse and the total cross sections are either calculated from a semi-empirical formula or from an interpolation of Shapiro's table. This will introduce uncertainty in the magnitude of the calculated cross section. Secondly, there is no consideration of angular momentum effects on the decay of the compound nucleus. The small value of the level density parameter, a, may partly compensate for the neglect of this effect. Thirdly, the separation

energies and δ values used may contain some uncertainties. The use of the approximate level density formula, Eq. (12), may not be justified at the excitation energies considered. The consideration that only p, n, and α can be emitted in the first stage of the evaporation process, and only p and n can be emitted in the second stage will also introduce some error in the calculation. The decay of the compound nucleus to levels below the "displaced" level may not be completely ignored.

Nevertheless, the reasonable agreement between experimental and calculated excitation functions signifies the applicability of the compound-statistical theory, even with the approximation mentioned, to these ^{3}He and ^{4}He induced reactions.

B. Comparison of Excitation Functions

According to the independence postulate,[1] the decay of the compound nucleus is independent of its mode of formation. Consider the nuclear reactions $a + A \rightarrow C^* \rightarrow b + B$ and $a' + A' \rightarrow C^* \rightarrow b + B$, where a, A, and a', A' are projectile-target pairs capable of forming the same compound nucleus C^*, and yielding the same product nucleus B and outgoing particle b. The reaction cross sections for these reactions are

$$\sigma(a,b) = \sigma_C(a)\, P(C,b) \quad , \tag{21a}$$

and

$$\sigma(a',b) = \sigma_C(a')\, P'(C,b) \quad , \tag{21b}$$

where $\sigma_C(a)$ and $\sigma_C(a')$ are the cross section for the formation of the compound nucleus C^* from the entrance channel involving a and a'

respectively; P(C,b) and P'(C,b) are the probability that the compound nucleus decays through the exit channel b + B from the entrance channels a + A and a' + A'. The independence postulate requires

$$P(C,b) = P'(C,b) \quad , \tag{22}$$

provided that the compound nuclei from both entrance channels have the same excitation energy. More generally, the following would be true:

$$\frac{\sigma(a,X)}{\sigma(a)} = \frac{\sigma(a',X)}{\sigma(a')} = \frac{\sigma(a'',X)}{\sigma(a'')} \quad , \tag{23}$$

where $\sigma(a,X)$ is the cross section for the nuclear reaction with entrance channel a + A and exit channel X (emission of particle and the corresponding residual nucleus); similarly for the other entrance channels a' and a'' through the same exit channel X, all involving the same compound nucleus C^*.

Equation (23) constitutes the basis for the classical test of the independence postulate. Ghoshal[21] first applied this test to the $^{64}Zn^*$ system. Ignoring angular momentum effects, the abscissa for the test is the excitation energy of the compound nucleus. The excitation energy is the sum of the available kinetic energy from the incident particle and its binding energy to the compound nucleus; and is given explicitly by

$$E^* = E_{pr} - \frac{m_{pr}}{m_C} E_{pr} + E_b = \frac{m_t}{m_C} E_{pr} + E_b \quad , \tag{24}$$

where E^* is the excitation energy in the compound nucleus,

E_{pr} is the kinetic energy of the projectile in the laboratory system,

m_{pr}, m_C, m_t are the masses of projectile, compound nucleus and target respectively,

E_b is the binding energy of the projectile to the compound nucleus.

Figure 18 shows the relationship between the excitation energy of the compound nucleus and the lab kinetic energy of the incident particle. The binding energies are calculated from the data given in the Table of Isotopes.[70]

The Coulomb barriers are shown in Fig. 18 as black dots. It must be emphasized that these Coulomb barriers are only approximations. Nuclear reaction below this barrier does occur, although with smaller cross section. It is interesting to note that the reaction with ^{3}He provides a way to high excitation energies in the compound nucleus at low bombardment energies. At the Coulomb barrier, the reaction involving ^{3}He has already possessed enough excitation energy to evaporate two or more particles. This accounts for the low cross section for the (^{3}He,n) reaction. For ^{22}Ne and ^{18}O induced reactions, the excitation energies at the Coulomb barrier are so high that even the two-nucleon evaporation cross sections are severly reduced in favor of three or more particle emissions.

The classical test of the independence postulate must be based on the "natural" reaction cross sections--that is, no Coulomb suppression of the excitation function should be allowed. Figure 19 shows the pn and 2n emission excitation functions for ^{3}He + ^{47}Ti and ^{4}He + ^{46}Ti. The similar shape and peak position of these excitation functions indicate that the independence postulate is essentially correct for this system.

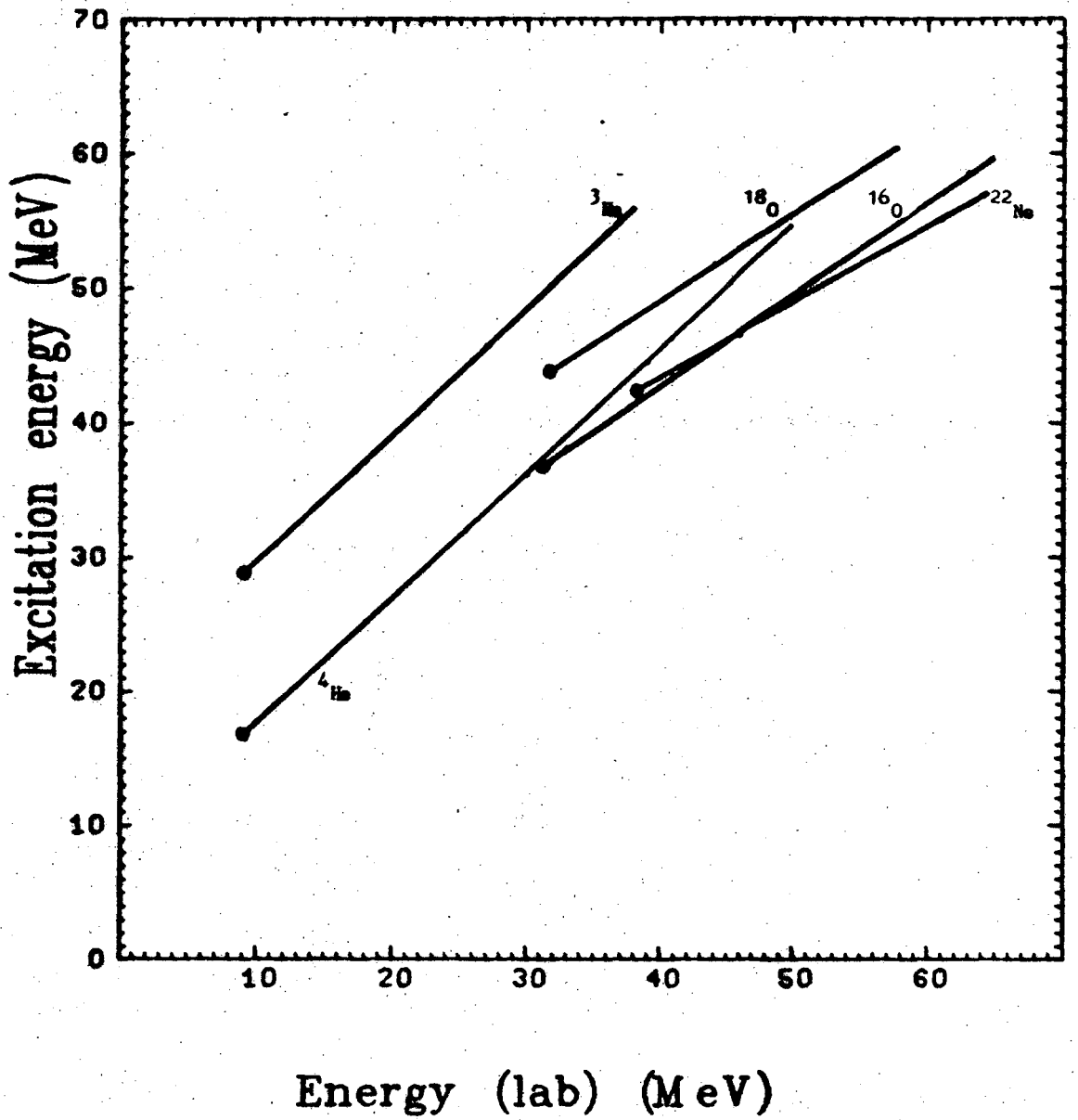

XBL 7012-7477

Fig. 18. Conversion curve for the bombardment energy and the excitation energy of the $^{50}Cr^{*}$ compound nucleus for various projectiles. Coulomb barriers are indicated by the black dots.

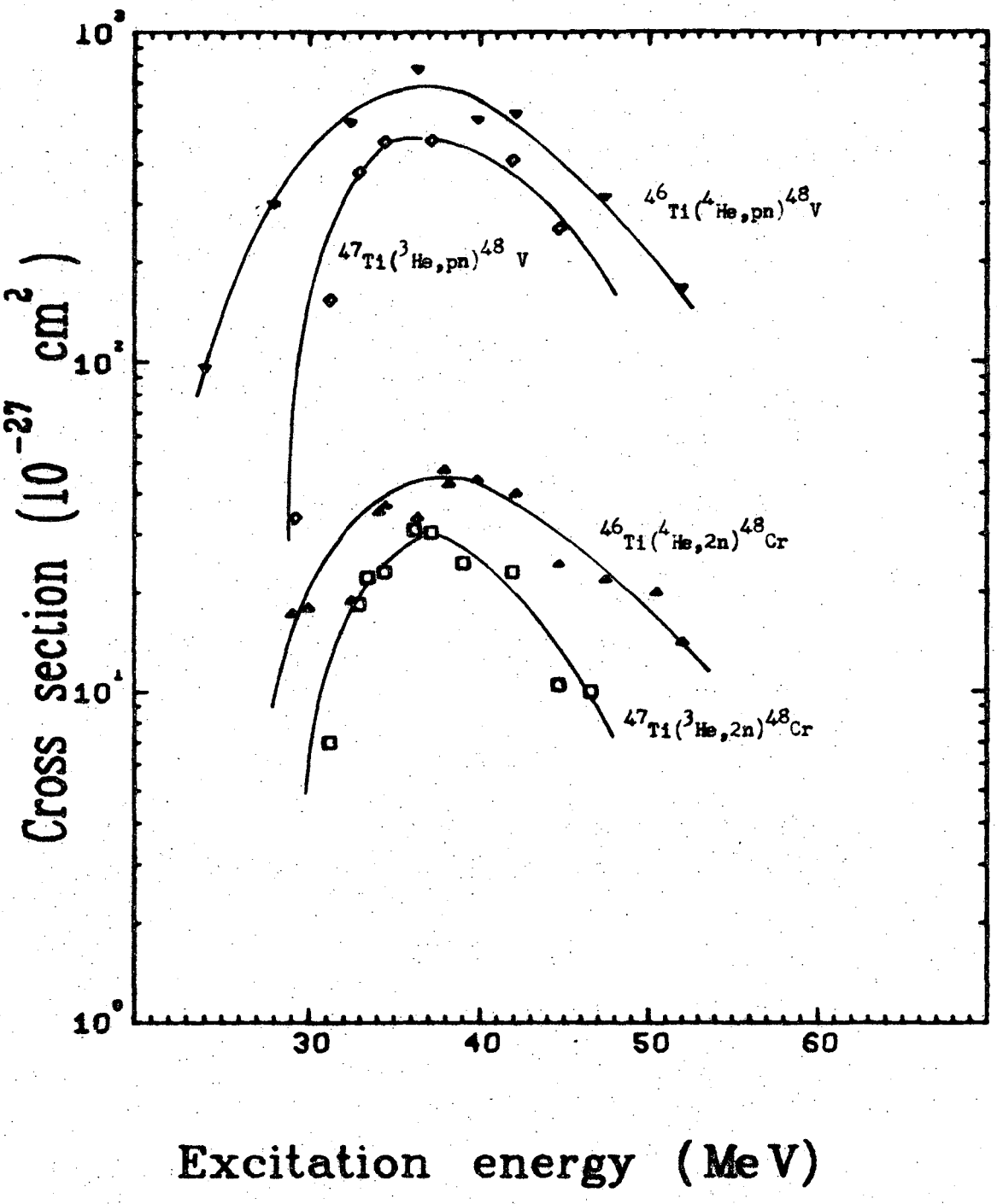

XBL 7012-7476

Fig. 19. Comparison of the 2n and pn evaporation excitation functions from ^{3}He + ^{47}Ti and ^{4}He + ^{46}Ti reactions. The solid lines are drawn to guide the eyes only.

The ^{3}He cross sections are lower than the corresponding ^{4}He cross sections by $\sim$ 20%. This difference is caused by the difference in the total reaction cross section for the formation of the compound nucleus at the same excitation energy with ^{3}He and ^{4}He particles.

As mentioned in Chapter III, the (^{16}O,pn) and (^{16}O,2n) excitation functions showed the "natural" peak. It is interesting to compare these excitation functions with those involving light particle (^{3}He or ^{4}He) bombardments. Figure 20 presents the 2n and pn excitation functions for ^{3}He, α and ^{16}O induced reactions.

In the classical test of the independence postulate, the comparison of various excitation functions can be made only after the reaction cross sections have been divided by the total cross section for the formation of the compound nucleus. However, the cross sections for the $^{16}O + ^{34}S$ reaction is near the Coulomb barrier, and the calculation of the compound nucleus formation total cross section by the optical model[71] is very sensitive to the parameters used. Furthermore, the parameters for the optical potential for this reaction system are not known experimentally. Therefore, the following procedure is taken to facilitate the comparison. The magnitude of the cross sections for the (^{3}He,pn) and (^{16}O,pn) reactions are arbitratily increased so that they are about equal to the (α,pn) excitation function at the peak position. The (^{3}He,2n) and (^{16}O,2n) cross sections are also increased the same percentage as the respective pn excitation functions. The result is shown in Fig. 21. A complete coincidence of the respective pn and 2n excitation functions will be a verification of the independence postulate in the classical sense. A glance at Fig. 21 shows that the ^{3}He and ^{4}He excitation functions agree quite well, and the ^{16}O excitation functions are definitely shifted toward

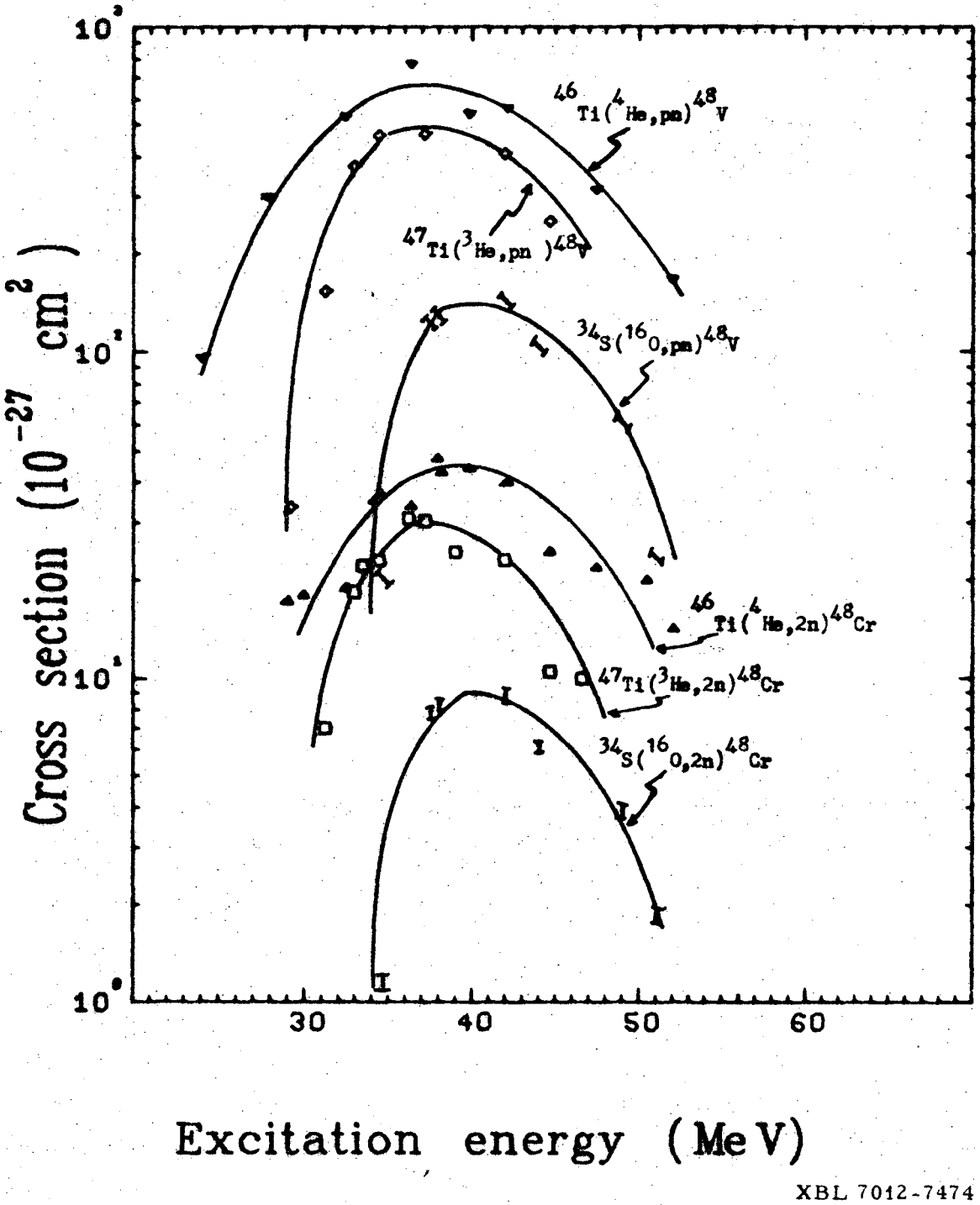

Fig. 20. Threeway comparison of the 2n and pn evaporation excitation functions from ^{3}He + ^{47}Ti, ^{4}He + ^{46}Ti, and ^{16}O + ^{34}S reactions.

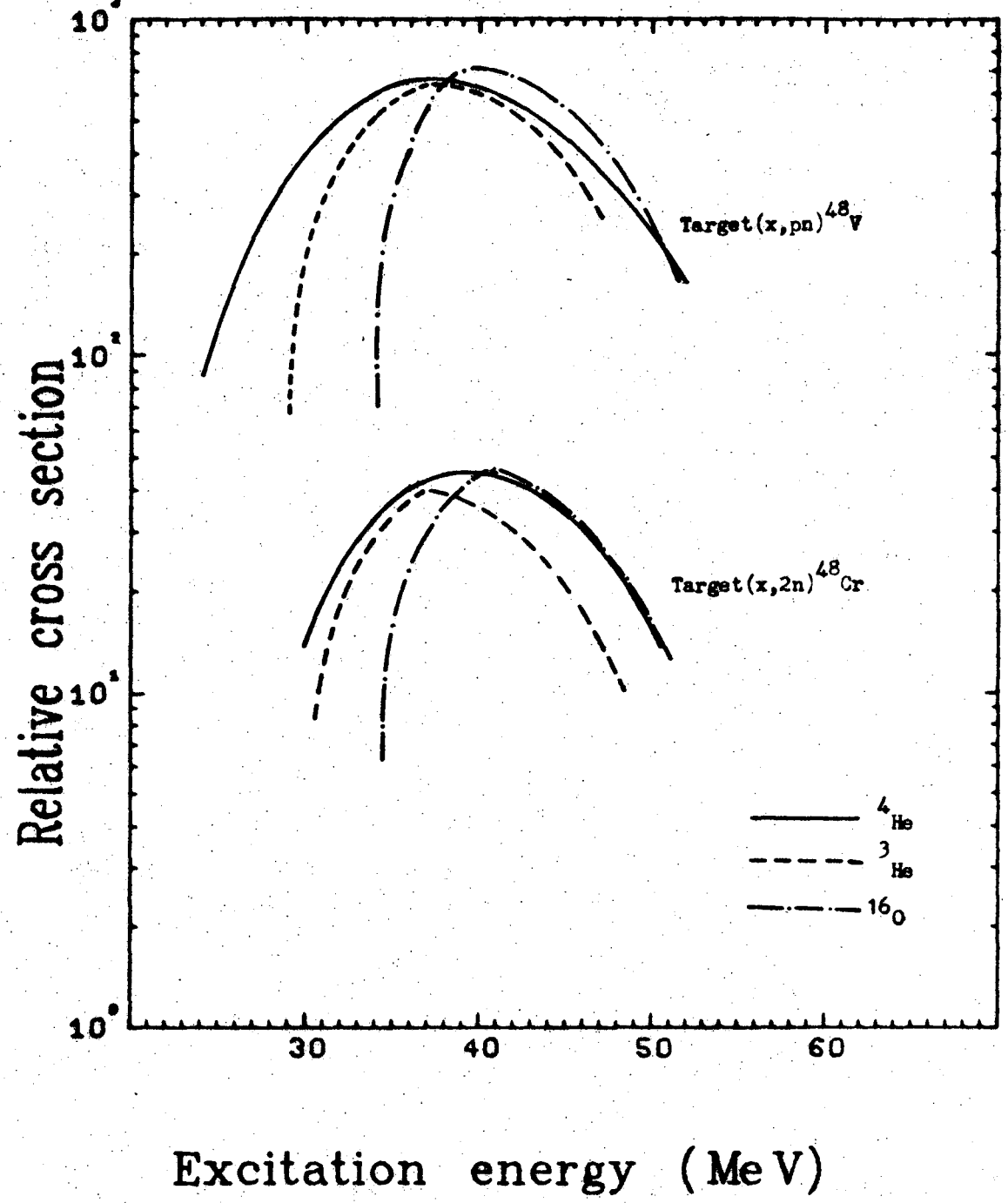

XBL 7012-7470

Fig. 21. Threeway comparison of the 2n and pn evaporation excitation functions after arbitrarily shifting the magnitude of the ^{16}O and ^{3}He cross sections. The ^{4}He cross sections are not shifted.

higher excitation energy. This violation of the independence postulate will be discussed later in Sec. D.

The excitation functions $^{32}S(^{18}O,2n)^{48}Cr$, $^{32}S(^{18}O,pn)^{48}V$, $^{28}Si(^{22}Ne,2n)^{48}Cr$, and $^{28}Si(^{22}Ne,pn)^{48}V$ can not be compared with the excitation functions shown in Fig. 21. The high Coulomb barrier and reaction Q values strongly suppress the reaction cross sections. As seen before, the ^{18}O and ^{22}Ne excitation functions are much smaller than the corresponding cross sections for ^{16}O-induced reactions. These excitation functions probably arise from the evaporation of high energy protons and neutrons. In this context, the ^{18}O and ^{22}Ne-induced reaction excitation functions can be compared with each other. Figure 22 shows such a comparison. The magnitudes and shapes of these excitation functions are quite similar. However, the ^{18}O excitation functions are shifted to a higher excitation energy from the ^{22}Ne-induced reactions.

If the ^{18}O induced reaction excitation functions are shifted arbitrarily 5.5 MeV toward lower excitation energies, there is a merger of the ^{18}O and ^{22}Ne excitation functions. Figure 23 presents the situation after the shift. This energy shift can be attributed to angular momentum effects (see Sec. D).

C. Effect of Nuclear Coulomb Barrier

Nuclear reactions involving ^{3}He and α-particles on similar targets might be expected to have similar cross sections at the same excitation energies, if the compound nucleus mechanism is involved. However, the low binding energy of the ^{3}He nucleus will bring into the compound nucleus a large amount of excitation energy. In the classical comparison of excitation functions, this increase in the excitation energy is taken

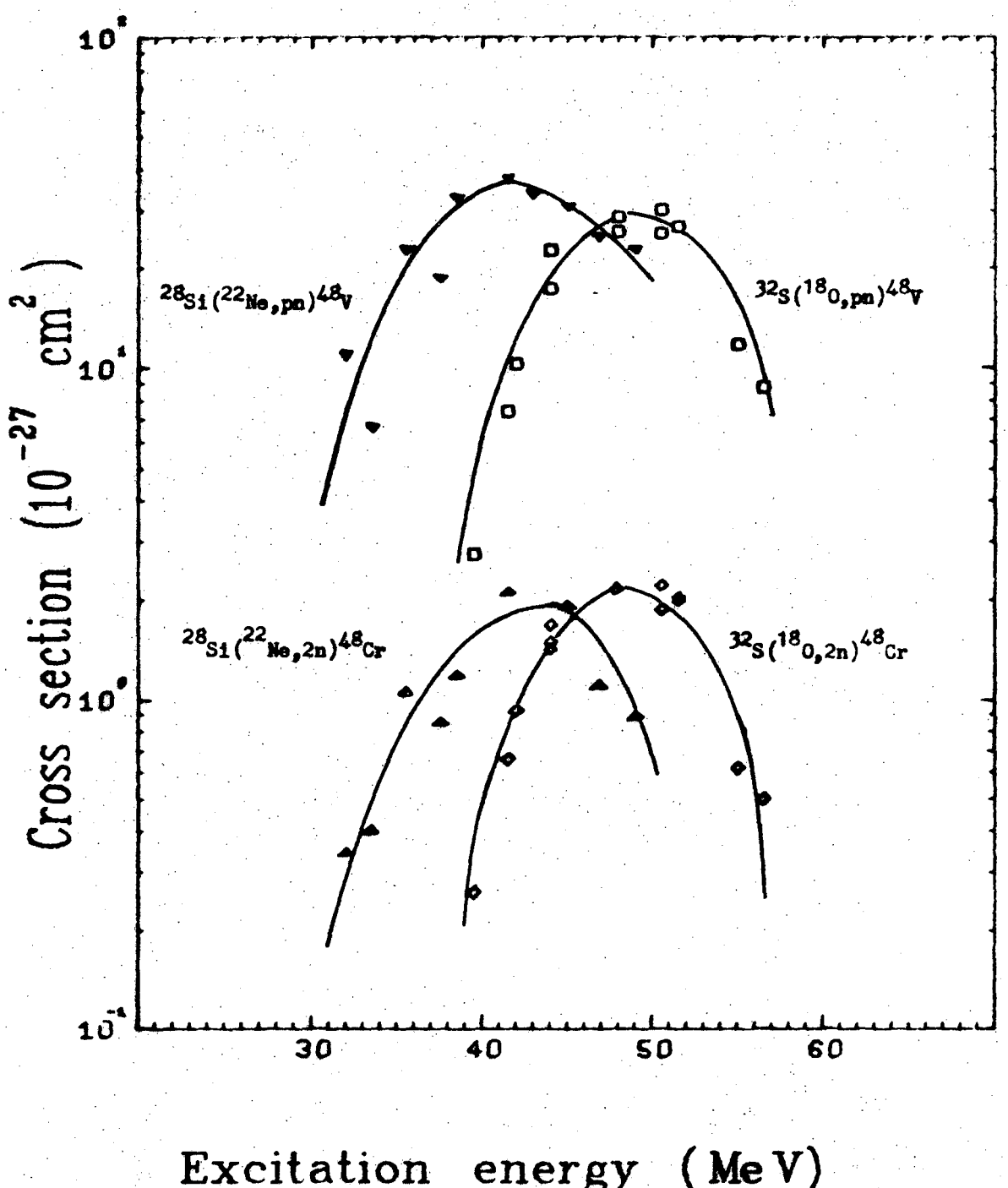

Fig. 22. Comparison of the 2n and pn emission excitation functions from the $^{18}O + ^{32}S$ and $^{22}Ne + ^{28}Si$ reactions. All these excitation functions are suppressed by the high Coulomb barrier.

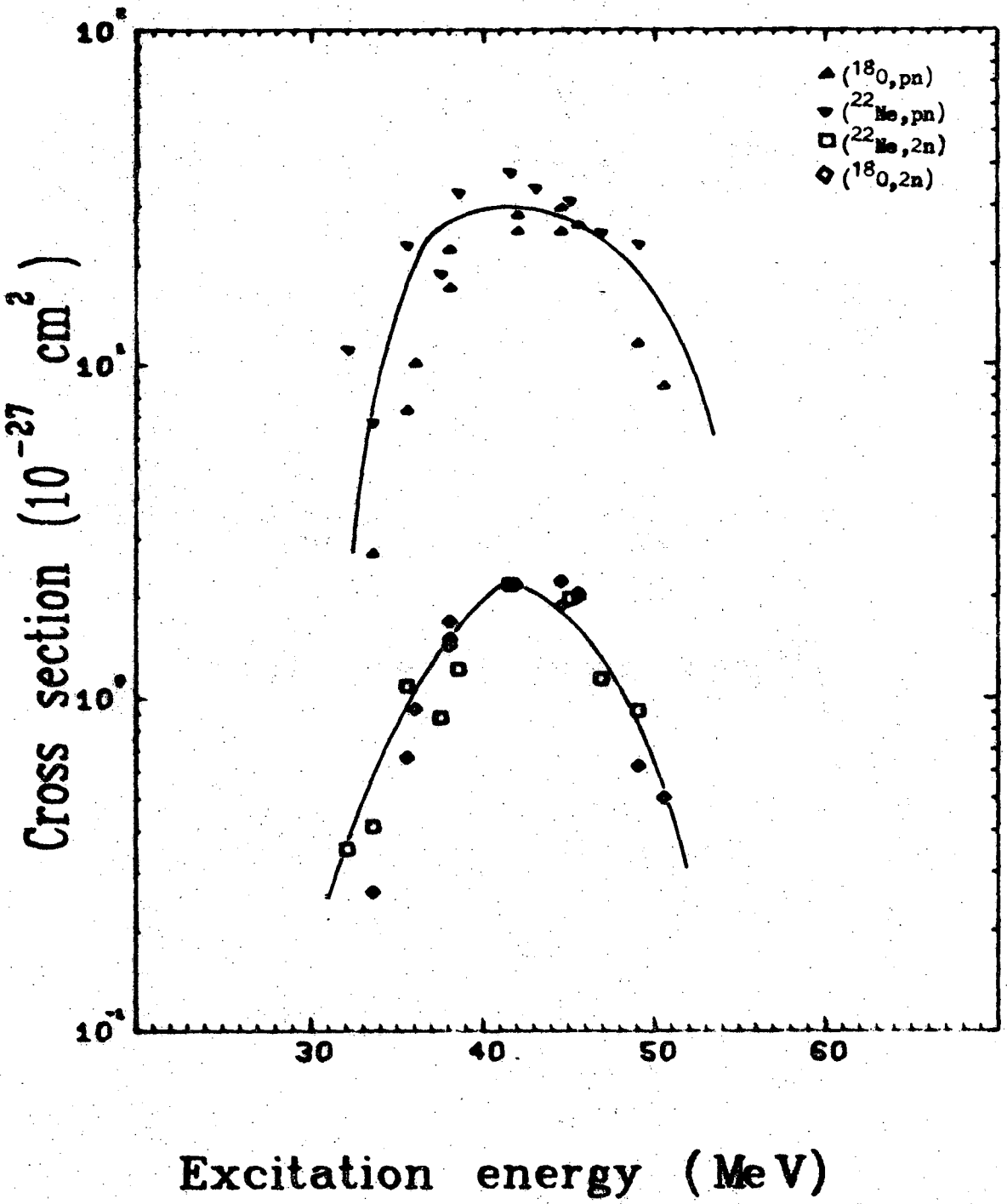

XBL 7010-6866

Fig. 23. Comparison of the 2n and pn evaporation excitation functions from the ^{18}O + ^{32}S and ^{22}Ne + ^{28}Si reactions after the ^{18}O-induced cross sections have been shifted 5.5 MeV toward lower excitation energy. The solid lines are drawn only to guide the eyes.

into account by using the excitation energy as the basis for comparison. In the case of single nucleon evaporation, such as (^{3}He,n) or (^{3}He,p), the excitation energy of the system is very high even at the Coulomb barrier such that these reactions are suppressed in favor of other reactions involving multiple nucleon emission. In effect, these reaction cross sections are "buried" under the Coulomb barrier.

Figure 24 shows the excitation functions for ^{47}Ti(^{3}He,n)^{49}Cr and ^{46}Ti(α,n)^{49}Cr reactions. As seen in last section, the two-nucleon evaporation cross sections (2n or pn) for α and ^{3}He reactions do not differ by more than 20%; whereas Fig. 24 shows the (^{3}He,n) cross section is an order of magnitude less than that for (α,n). This should not be considered as a violation of the compound-nuclear picture (particularly the independence postulate). There is a significant difference in the compound nucleus formed by the ^{3}He and α reactions--at the expected peak position for the (X,n) reaction, the probability for forming the ^{50}Cr* compound nucleus from ^{3}He + ^{47}Ti is extremely small due to the Coulomb barrier. Even though the decay of the compound nucleus is independent of its mode of formation, there are much fewer compound nuclei for the ^{3}He + ^{47}Ti reaction; and the cross section will be much smaller than the corresponding ^{4}He induced reaction.

Similar situation exists for the ^{16}O and ^{18}O induced reactions. Because these reactions involve heavy ions, the Coulomb barriers are much higher than the reactions involving α and ^{3}He. The binding energy of the ^{18}O nucleus is much lower than that for ^{16}O, and at the Coulomb barrier, the excitation energy for the ^{18}O induced reaction is high enough to suppress two-nucleon evaporations in favor of more nucleon emissions.

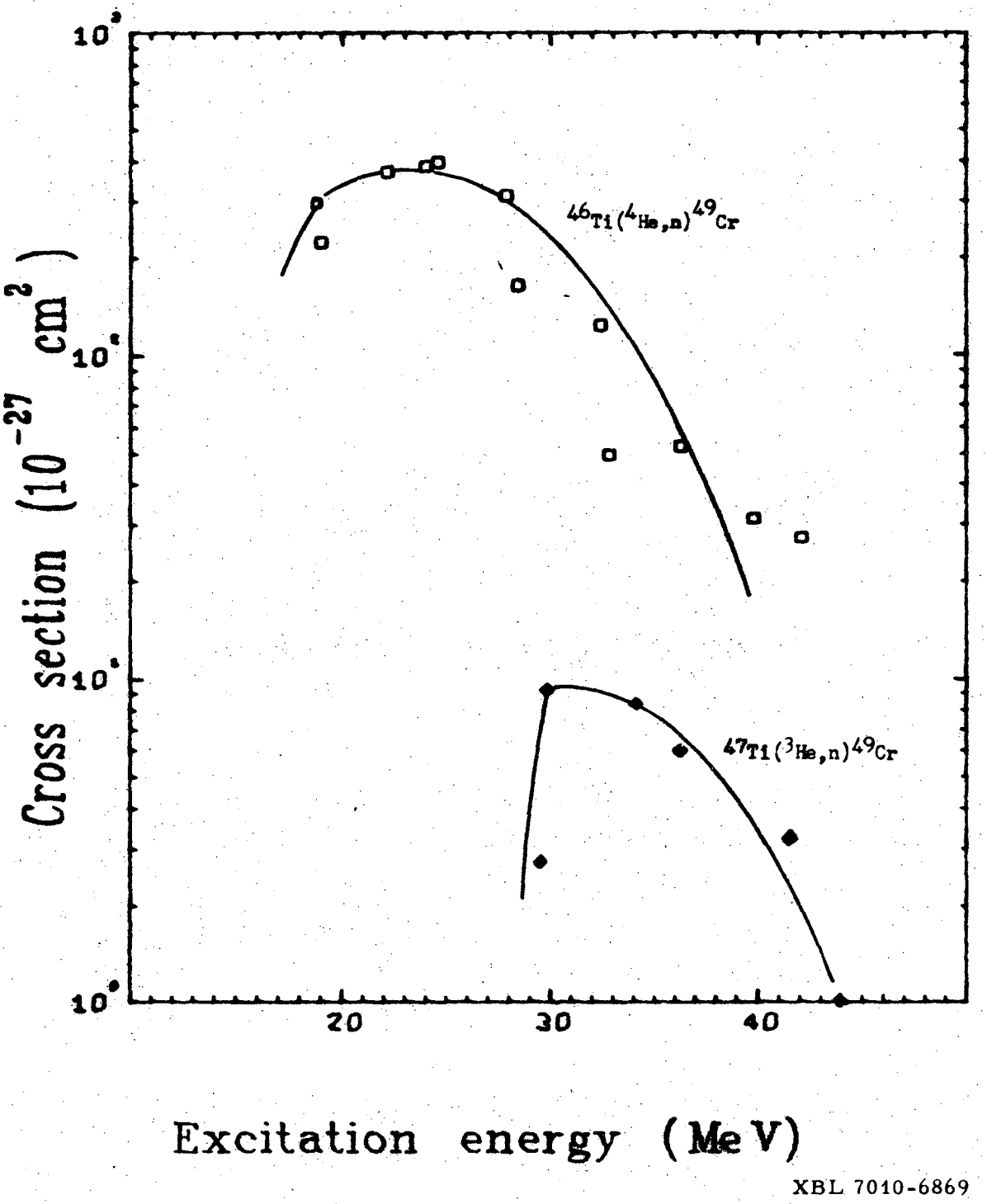

Fig. 24. Comparison of the (X,n) cross sections from ^{3}He and ^{4}He reactions. The ^{47}Ti(^{3}He,n)^{49}Cr is strongly suppressed by the Coulomb barrier.

Although at the Coulomb barrier, the excitation energy for the ^{16}O-induced reaction is high enough to evaporate three low-energy nucleons, the two-nucleon evaporation is still favored. Figure 25 shows that the $^{34}S(^{16}O,2n)^{48}Cr$ and $^{34}S(^{16}O,pn)^{48}V$ excitation functions are about 10 times that of the corresponding excitation functions for the $^{18}O + ^{32}S$ reaction system.

In general, when performing a classical test of the independence postulate, care must be taken to insure that the excitation functions used are "natural" ones which have not been suppressed by the Coulomb barrier. The steep low-energy edge, such as in the $(^{16}O,2n)$ and $(^{16}O,pn)$ excitation functions (Figs. 12 and 25), caused by the Coulomb barrier should also be noticed.

D. Effects of Angular Momentum

Admittedly, the study of the angular momentum effects based on total excitation functions is not ideal. The details of the angular and energy distribution of the evaporated particles are lost. The spin-dependent level density[72,73] will influence both the p and n evaporation, so that no anomaly is apparent. Grover[19] has pointed out that the inclusion of the competition between gamma-ray and particle emission will give a level density parameter "a" more consistent with that expected from the Fermi-gas system.[61] Sperber[18] showed that the ratio of gamma emission width to neutron width increases with increasing angular momenta in the compound nucleus.

One of the obvious effects of high angular momentum is indicated by the energy shift of the excitation functions. Generally, the evaporation of particles will release from the compound nucleus a large amount

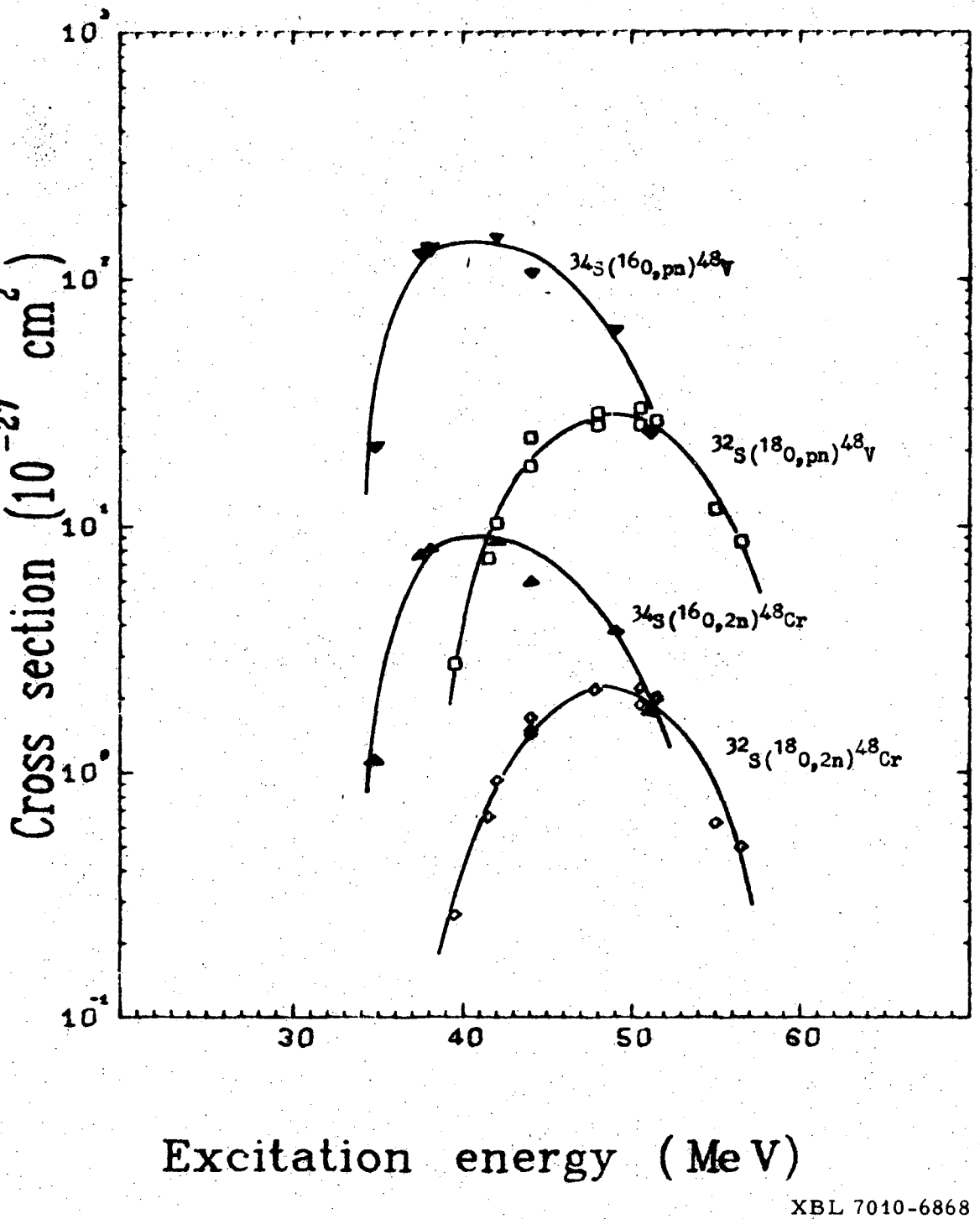

Fig. 25. Comparison of the 2n and pn evaporation excitation functions from $^{16}O + ^{34}S$ and $^{18}O + ^{32}S$ reactions. The ^{18}O reaction cross sections are suppressed by the Coulomb barrier.

of excitation energy but small amount of angular momentum, because of the large binding energy and small kinetic energy of the emitted particle. However, for any given angular momentum, there is an energy limit[74,75] below which no level could exist. If the decay of the compound nucleus with large initial angular momentum only by particle emission, the compound nucleus will achieve a situation where it will have low excitation energy and high angular momentum. This compound nucleus then will possess enough excitation energy to emit another particle, but there is no available level with the necessarily high angular momentum in the residual nucleus, and thus the emission of that particle is prohibited. In this case, de-excitation must proceed via gamma-ray emission. This de-excitation by gamma rays essentially removes some of the available excitation energy for nucleon emission and therefore, the excitation function must be shifted toward higher excitation energy.

An alternative view is developed by Ericson and Strutinski.[76] In this treatment, the rotational energy of the compound nucleus is considered to be unavailable for de-excitation by particle emission, and the true internal excitation energy, $E^{\dagger}$, is given by

$$E^{\dagger} = E^{*} - E_{r} \quad , \tag{25}$$

where E^{*} and E_{r} are the excitation energy and rotational energy respectively.

In this section, attempts will be made to estimate the rotational energy of the compound nucleus and compare it with the experimentally observed energy shift of the excitation functions. The rotational energy of the compound nucleus is[69]

$$E_r = \frac{\hbar^2}{2\mathfrak{J}} \langle J(J+1) \rangle \quad , \tag{26}$$

where $\mathfrak{J}$ is the moment of inertia of the compound nucleus

J is the spin of the compound nucleus

$\hbar$ is Planck's constant/2π,

the moment of inertia of the compound nucleus is usually approximated by its high excitation limit,[76]

$$\mathfrak{J} \approx \mathfrak{J}_r = \frac{2}{5} mR^2 \quad , \tag{27}$$

where $\mathfrak{J}_r$ is the moment of inertia of a rigid sphere,

m is the mass of the compound nucleus,

R is the radius, and is given by $1.2\ A^{1/3}$ fm, where A is the mass number of the compound nucleus.

The quantity $\langle J(J+1) \rangle$ in Eq. (26) is given by its equivalent

$$\langle J(J+1) \rangle \equiv \langle J^2 \rangle + \langle J \rangle \quad . \tag{28}$$

Here, $\langle J \rangle$ is the average angular momentum quantum number of the compound nucleus. In order to calculate the average quantities, the distribution of angular momentum for the compound nucleus as a function of energy is required.

1. Calculation of Average Angular Momentum

The cross section for the formation of a compound nucleus with angular momentum quantum J_C at bombarding energy E is[77]

$$\sigma(J_C,E) = \pi\lambda^2 \sum_{S=|I-s|}^{I+s} \sum_{\ell=|J_C-S|}^{J_C+S} \frac{2J_C + 1}{(2s + 1)(2I + 1)} T_\ell(E) \quad , \tag{29}$$

where λ is the de Broglie wavelength of the incoming particle,

I is the spin of the target nucleus

s is the spin of the projectile

$T_\ell(E)$ is the transmission coefficient of the projectile with orbital angular momentum ℓ and energy E.

Of course, there is a maximum angular momentum quantum number $J_C(\max)$ for the compound nucleus at a given energy,

$$J_C(\max) = \ell_{max} + s + I \quad , \tag{30}$$

where ℓ_{max} is chosen so that $T_{\ell_{max}} > 10^{-6}$.

Now the probability P_{J_C} for the formation of the compound nucleus with spin J_C is simply

$$P_{J_C} = \frac{\sigma(J_C,E)}{\sum_{J_C=0}^{\infty} \sigma(J_C,E)} \quad . \tag{31}$$

By definition, the average angular momentum quantum number $\langle J_C \rangle$ and $\langle J_C^2 \rangle$ can be calculated as

$$\langle J_C \rangle \equiv \frac{\sum_{J_C} J_C P_{J_C}}{\sum_{J_C} P_{J_C}} \quad , \tag{32a}$$

$$\langle J_C^2 \rangle \equiv \frac{\sum_{J_C} J_C^2 P_{J_C}}{\sum_{J_C} P_{J_C}} , \qquad (32b)$$

where the sum is performed over the interval $J_C(\max)$ and $J_C(\min) = |I-s|$. Hafner et al.[78] have written a computer program, ISOMER, based on Eqs. (29) - (32) to calculate the average angular momentum quantum number of the compound nucleus. The ISOMER program requires as its input the spin of target and projectile, the de Broglie wavelength of the incident particle, and the transmission coefficients for the projectile of different ℓ at E. The calculation of $T_\ell(E)$ will be discussed next.

2. Calculation of Transmission Coefficients

The transmission coefficients for any target-projectile system can be calculated by the optical model.[79] However, the optical parameters for the heavy ion reactions on light targets are not well known, approximate methods will be used to calculate the transmission coefficients. Following a method given by Thomas,[80] the nuclear interaction between the target and projectile can be approximated by a diffuse potential

$$V(r,\ell) = \frac{Z_1 Z_2 e^2}{r} + \frac{\hbar^2 \ell}{2\mu r^2}(\ell+1) - 67 \exp\left[\frac{r-1.17(A_1^{1/3} + A_2^{1/3})}{-0.574}\right] , \qquad (33)$$

where Z_1, Z_2 = charges of the projectile and target respectively,

A_1, A_2 = mass number of projectile and target,

μ = reduced mass of the system,

r = distance between the interacting pair,

ℓ = orbital angular momentum of the projectile

e = electron charge.

This potential is then further approximated by a parabola with matching position, height, and curvature at its maximum. For the parabola, Hill and Wheeler[81] showed that the transmission coefficient is given by

$$T = \frac{1}{1 + \exp[2\pi(B-E)/\hbar\omega]} \quad , \tag{34}$$

where B is the height of the barrier, E is the center of mass energy of the system, and ω is the vibrational frequency of the harmonic oscillator having a potential energy function given by the negative of the barrier. The frequency $\hbar\omega$ can be calculated by[82]

$$\hbar\omega_\ell = \left| \frac{\hbar^2}{\mu} \frac{d^2V_\ell}{dr^2} \right|^{1/2} \quad , \tag{35}$$

where d^2V_ℓ/dr^2 is the second derivative of the diffuse potential (Eq. (33)) evaluated at r_o where $V(r_o)$ is a maximum.

First and second derivatives for Eq. (33) are calculated and Eq. (35) is evaluated by the conventional Newton's method. Then the values of $\hbar\omega$ and B substituted in Eq. (34) to obtain the transmission coefficients.

The values of the $T_\ell(E)$ are "fed" to the ISOMER program for compound nucleus spin distribution calculation. A typical spin distribution for the reaction $^{16}O + ^{32}S$ forming the $^{50}Cr^*$ compound nucleus is shown in Fig. 26. The value of $\langle J(J+1) \rangle$ is then calculated from Eq. (28) and (32). The result of the calculation is summarized in Fig. 27.

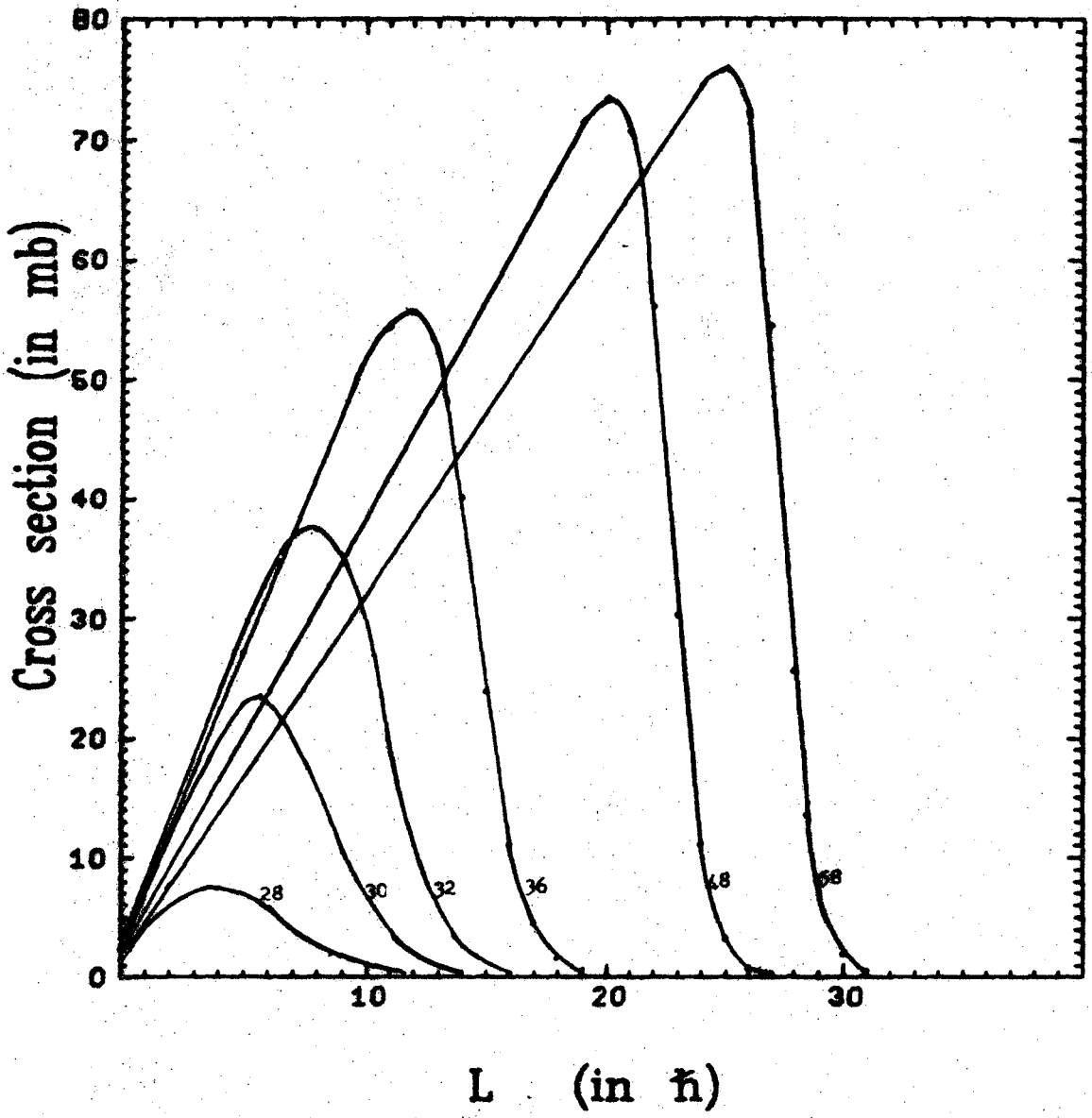

XBL 7012-7478

Fig. 26. Distribution of angular momenta for the $^{50}Cr^{*}$ compound nucleus from $^{16}O + ^{34}S$ reactions. The numbers in the figure refer to the ^{16}O bombardment energy in MeV.

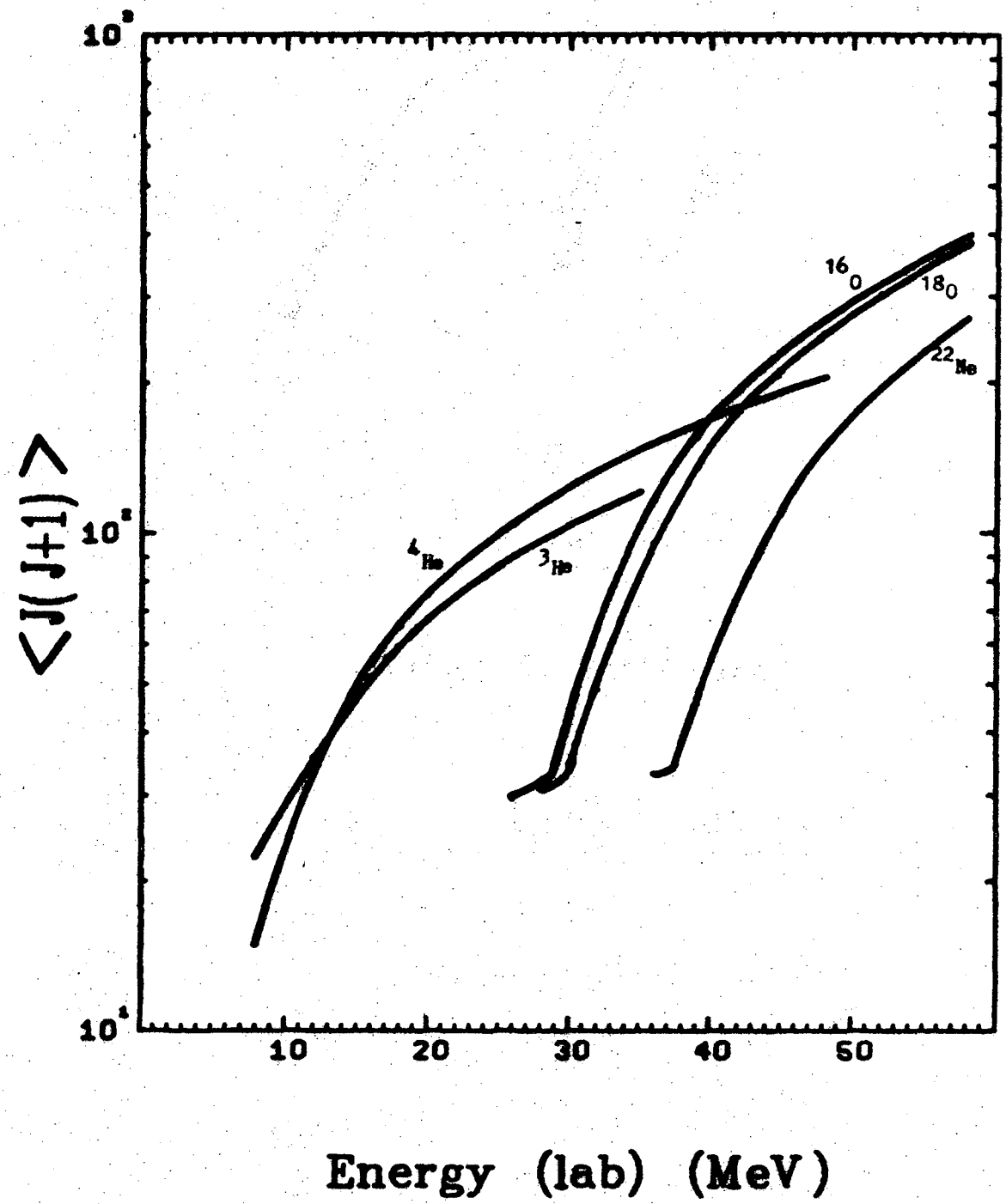

XBL 7012-7479

Fig. 27. Values of the ⟨J(J+1)⟩ for the $^{50}Cr^{*}$ compound nucleus as a function of bombarding energy for the various reactant pairs.

3. Estimation of Rotational Energy

From Fig. 27, it can be seen that for ^{3}He and ^{4}He, ^{16}O and ^{18}O systems at similar bombarding energies, the average angular momentum are quite similar. It is also noted that the heavy ion reactions generally bring in more angular momentum to the compound nucleus.

With Eq. (26) and Fig. 27, the rotational energy of the compound nucleus can be calculated. At the peak position of the $(\alpha,2n)$ and (α,pn) excitation functions, the bombarding energy is about 31 MeV. The $\langle J(J+1) \rangle$ value is 130 and the rotational energy is 6.4 MeV. For the $(^{16}O,2n)$ and $(^{16}O,pn)$ excitation functions, the rotational energy at the peak is 7.4 MeV. The expected energy shift between the ^{16}O and α induced reactions will therefore be 1 MeV. The observed shift is about 2 ± 1 MeV. The difference may be caused by the Coulomb barrier acting on the low-energy edge of the ^{16}O excitation functions.

For the ^{22}Ne-induced reactions, the rotational energy at the peak of the two-nucleon evaporation excitation functions is about 2.0 MeV, and for the ^{18}O-induced reactions E_r is 5.9 MeV. The expected displacement between the ^{18}O and ^{22}Ne excitation functions is about 4 MeV. The observed shift is 5.5 ± 1 MeV (see Fig. 20).

Although the calculated energy shifts do not agree perfectly with the observed ones, these approximate calculations do allow qualitative understanding of the effect of angular momentum upon the de-excitation of the compound nucleus. Better agreement can be achieved if the moment of inertia of the rotating compound nucleus is taken to be[25] $k\mathcal{J}_r$ where k is a parameter, and $\mathcal{J}_r$ is given by Eq. (27). For more accurate and realistic calculations, the treatment which involves the detailed calculation of the γ-ray de-excitation and spin distribution[83] of the decaying compound nucleus may be necessary.

V. FORWARD RECOIL EXPERIMENTS

The usefulness of recoil studies as applied to the compound nucleus reaction mechanism has been pointed out by several authors.[11,84] Forward recoil ranges in aluminum for the products from $\alpha + {}^{46}Ti$ reaction were measured to supplement excitation function measurements. In the following sections, a "thick-target" method for the recoil range measurement is described. The implication of the experimental result to the nuclear reaction mechanism is also discussed.

A. Thick-Target Method

In the recoil studies of nuclear reaction mechanism, two techniques are generally employed--thin-target and thick-target methods. In the thick-target method, the target thickness is large compared with the range of the recoiling nuclei, therefore only nuclei sufficiently close to the surface of the target can escape out of the target. It can be shown[85] that the fraction of recoiling nuclei (F) is related to the target thickness (W) and the projected range (R_p) as

$$F = R_p/W \quad . \tag{36}$$

Usually F is the only quantity measured during a thick-target recoil experiment, and the projected range is calculated from Eq. (36).

In a thin-target ($\sim$ 10 $\mu g/cm^2$) experiment, the distribution of the recoil nuclei in a stopping medium is measured and the range is obtained directly from the distribution curve. Generally the thin-target experiment yields more information of the nuclear reaction in question. However, it is quite difficult to prepare very thin and uniform targets, and sometimes the low product yeilds render the subsequent

detection of radioactivity impossible. It is therefore desirable to be able to determine the range distribution by using a thick target.

The distribution of the range about the mean range R_o for a thin-target experiment is[85]

$$Y(R) = (2\pi)^{-1/2}(\rho R_o)^{-1} \exp\left[-(R_o - R)^2/2\rho^2 R_o{}^2\right] \quad , \qquad (37)$$

with ρ, the straggling parameter given by[86]

$$\rho^2 = 2M_1M_2/3(M_1 + M_2)^2 \quad , \qquad (38)$$

where M_1 and M_2 are the masses of the recoiling and stopping nuclei, respectively.

A computer program was used to simulate the recoiling nuclei from a 1-$\mu g/cm^2$ target into a few 160-$\mu g/cm^2$ stopping foils. The fractions of the recoiling nuclei passing through each foil are calculated for the distribution of Eq. (37). The result is shown in Fig. 28. The straight line in this probability plot is indicative of a Gaussian distribution, and the point at 50% corresponds to the mean range R_o.

A thick target can be thought of as a stack of thin targets, and the distribution of the recoil nuclei can be taken as the sum of the contributions from each of the thin targets in the stack. If we choose a stopping material having approximately the same stopping power as the target material, and use the Gaussian distribution of Eq. (37), the recoil behavior of any target thickness can be calculated. Figure 29 represents such a calculation for a 1-mg/cm^2 and a 200-$\mu g/cm^2$ in aluminum. From Fig. 29, we see that the relative amount of activity in equal catcher foils does not change whenever the target thickness is large compared with R_o.

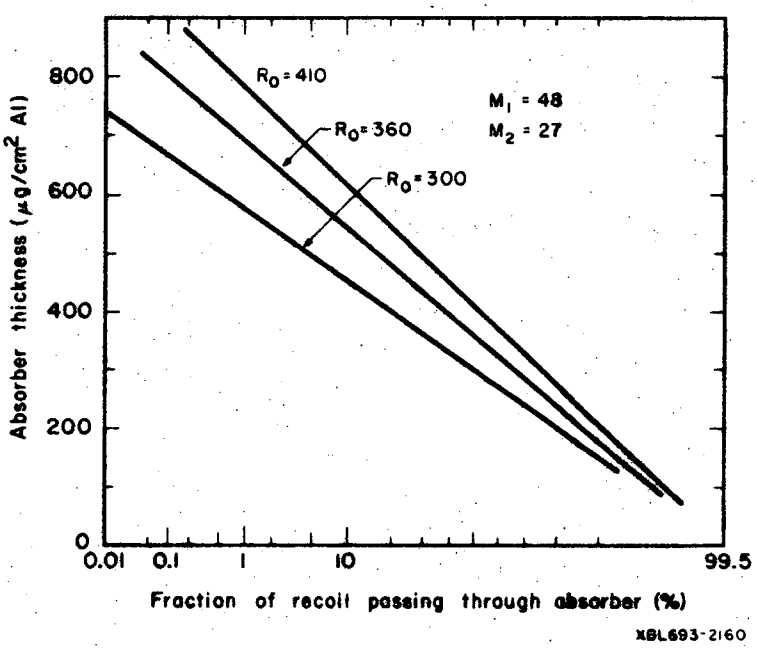

Fig. 28. Calculated probability plot for a 1-μg/cm^2 TiO_2 target with 160 μg/cm^2 Al catcher foils. Notice that R_o corresponds to where the straight line passes through the 50% fraction. The recoil nuclei are ^{48}Cr.

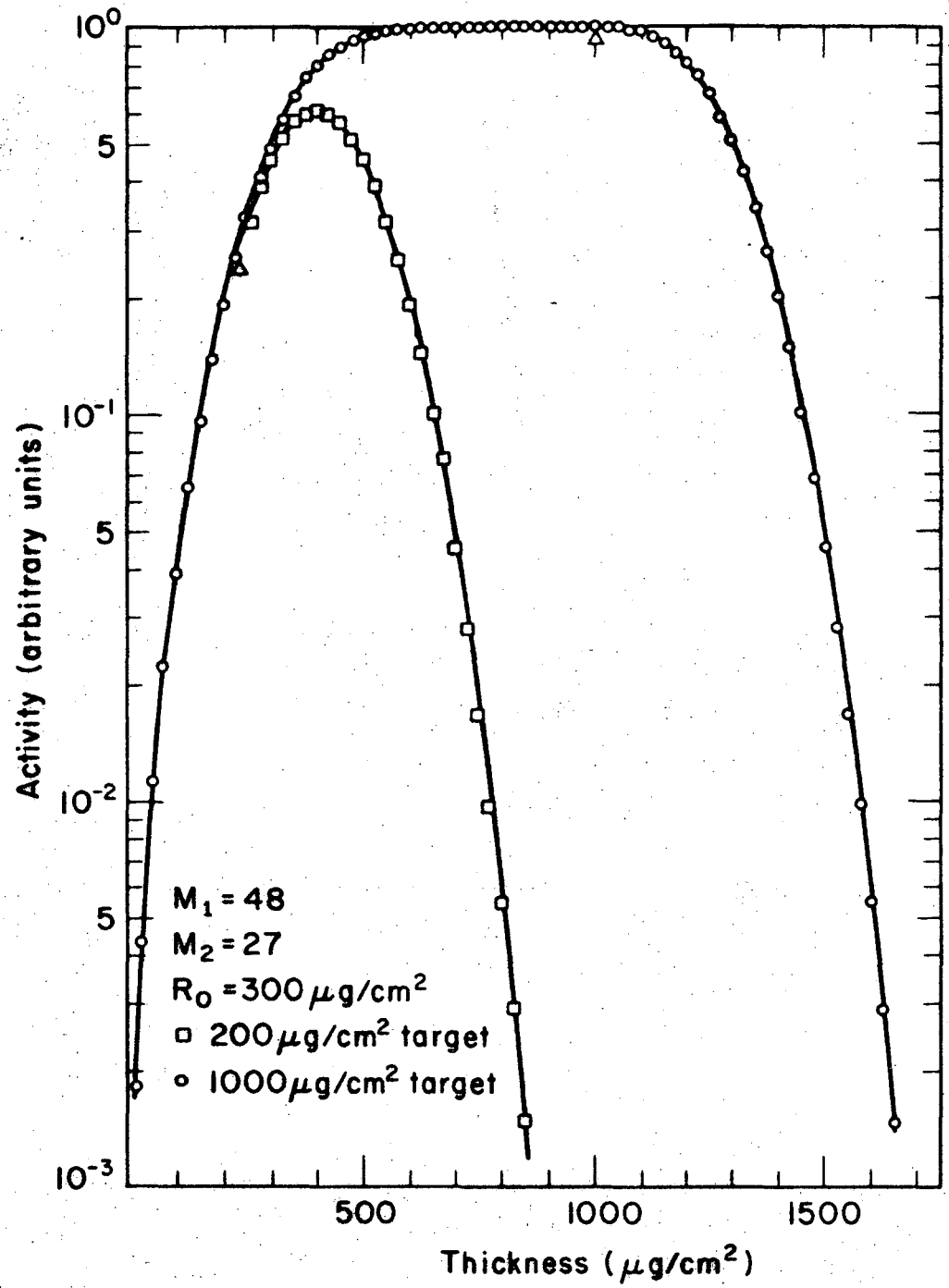

Fig. 29. Calculated distribution of recoil for targets of different thicknesses based on a stacking of thin (1-μg/cm^2) targets. Targets and the catcher foils are assumed to have equal stopping power for the recoiling nuclei. The triangles in the figure indicate the interfaces of the targets and catchers.

When the target thickness is less than R_o, the relative amount of activity in equal catcher foils not only depends on the R_o, but also depends on the target thickness.

Figure 30 represents a calculation for a 1-mg/cm^2 target as the sum of 1000 1-μg/cm^2 targets. Since many of the recoil nuclei have been stopped in the target, the 50% point no longer corresponds to R_o.

The thickness of the target used in the experiment is 1 mg/cm^2 TiO_2. The target is prepared by sedimentation of TiO_2 powder in alcohol onto 5-mil Al foil. The TiO_2 used is enriched in ^{46}Ti, with the average charge ($\bar{Z}$), 12.7, and average mass per atom ($\bar{A}$), 26.2. The stopping power of the target material is taken as equal to that of aluminum (A = 27, Z = 13). A stack of six aluminum foils (160 μg/cm^2 each) is used as catchers. The target is bombarded at the 88-inch cyclotron with 40 MeV α-particles at the rate of 1 μA. The actual α-particle energy is estimated from the range-energy curve for Al calculated by the computer code RANGES.[31]

After bombardment, the target and the catcher foils are counted with the 14 c. c. Ge(Li) detector. The activity of ^{48}Cr is determined from the 0.116 MeV(100%) γ-ray. The result is represented by the dotted line in Fig. 30. R_o is estimated to be 390 μg/cm^2 Al for the α-particle bombarding energy of 31.6 MeV.

Vacuum-evaporated targets are also used. These targets are made by vacuum evaporation of ^{46}Ti-enriched TiO_2 onto 1-mil aluminum foils. The thickness is typically 200 μg/cm^2 with good uniformity. Five to six aluminum leaves (160 μg/cm^2) are stacked to form the catcher assembly. The targets are again bombarded with α-particles at the 88-inch cyclotron. The activities of ^{49}Cr and ^{48}Cr are measured with a Ge(Li) detector. The

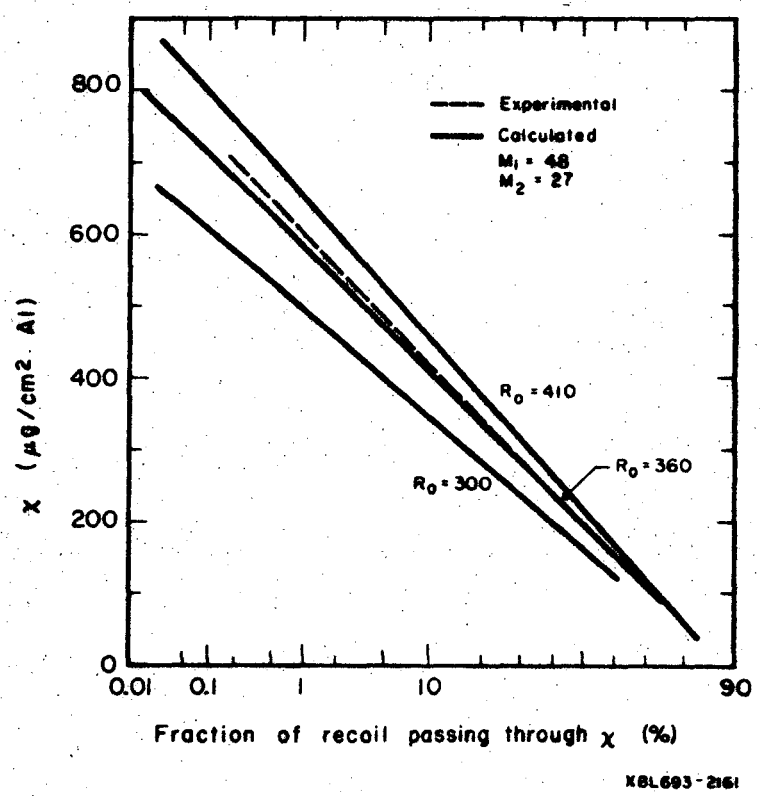

Fig. 30. Calculated plot for a 1-mg/cm^2 TiO_2 target with 160-μg/cm^2 Al catchers. The broken line contains experimental values for the recoils of the $^{46}Ti(\alpha,2n)^{48}Cr$ reaction. The R_o for the experimental data is estimated to be 390 μg/cm^2 Al.

results are presented in probability plots and shown in Figs. 31 and 32.

Experimental recoil ranges can be estimated from the probability plots. The results are summarized in Table VI.

B. Results

When a projectile particle fuses with the target nucleus to form a compound nucleus, the momentum transfer from the incoming particle to the compound nucleus is complete. If the subsequent de-excitation of this compound nucleus is assumed to be isotropic emission of particles, the recoil energy of the residual nucleus is given by[87]

$$E_r = \frac{A_{pr}A_r}{(A_{pr} + A_t)^2} E_{pr} \quad , \tag{39}$$

where E and A are energy and mass number respectively. The subscripts r, pr, and t refer to recoil, projectile, and target nucleus. Theoretical treatment of the ion-matter interaction has been advanced by Lindhard, Scharff, and Schiøtt.[88] They obtained the range-energy relations for ions in a stopping medium. A series of universal range-energy curves for different values of the electronic stopping parameter K is plotted in the dimensionless range and energy space. Their plot can be converted to the more conventional range-energy curves. A plot for ^{48}Cr recoiling into aluminum is calculated and presented in Fig. 33.

Table VI summarized the results of experimental and theoretical recoil ranges. Gaussian distribution of the recoil can be inferred from the straight lines in Figs. 30, 31, and 32. The Gaussian distribution

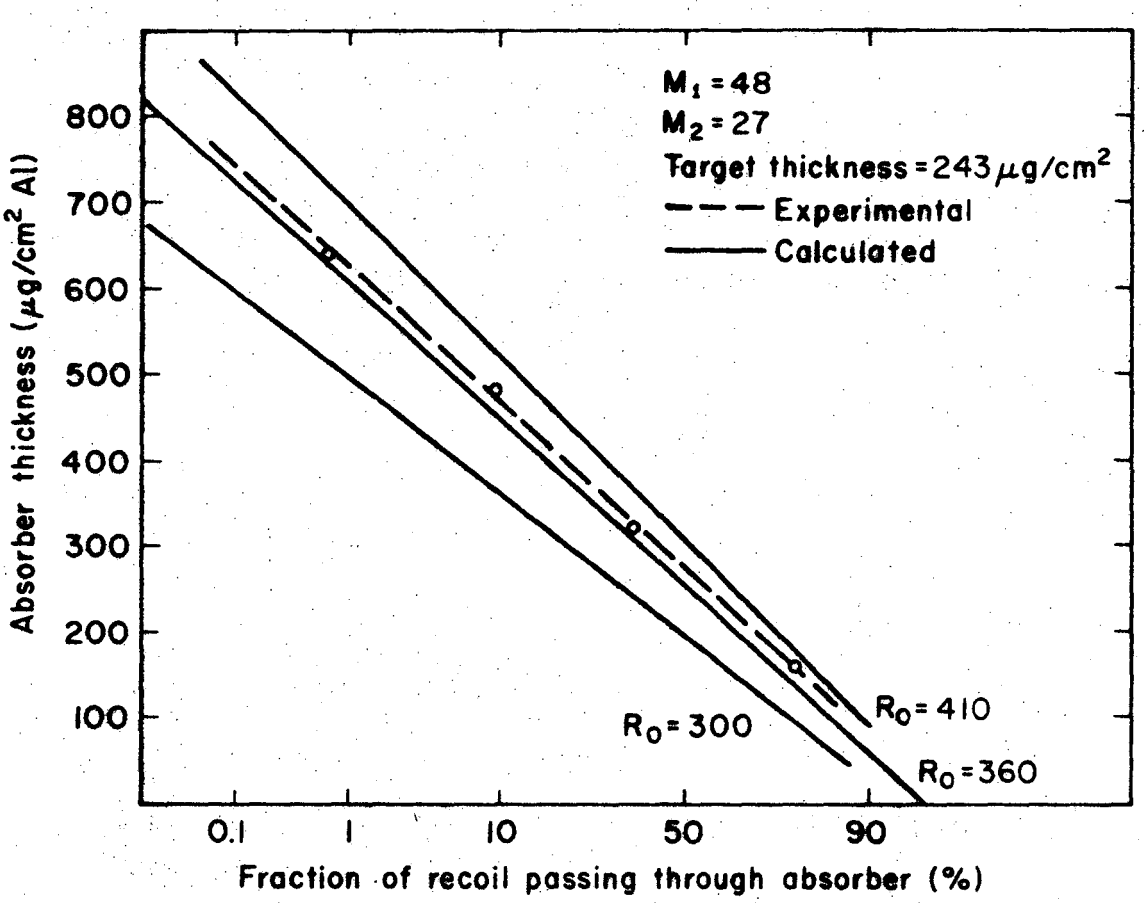

XBL 701-2031

Fig. 31. Probability plot for ^{48}Cr recoil from $^{46}Ti(\alpha,2n)^{48}Cr$. A straight line indicates Gaussian distribution. The experimental range is estimated to be 380 $\mu g/cm^2$.

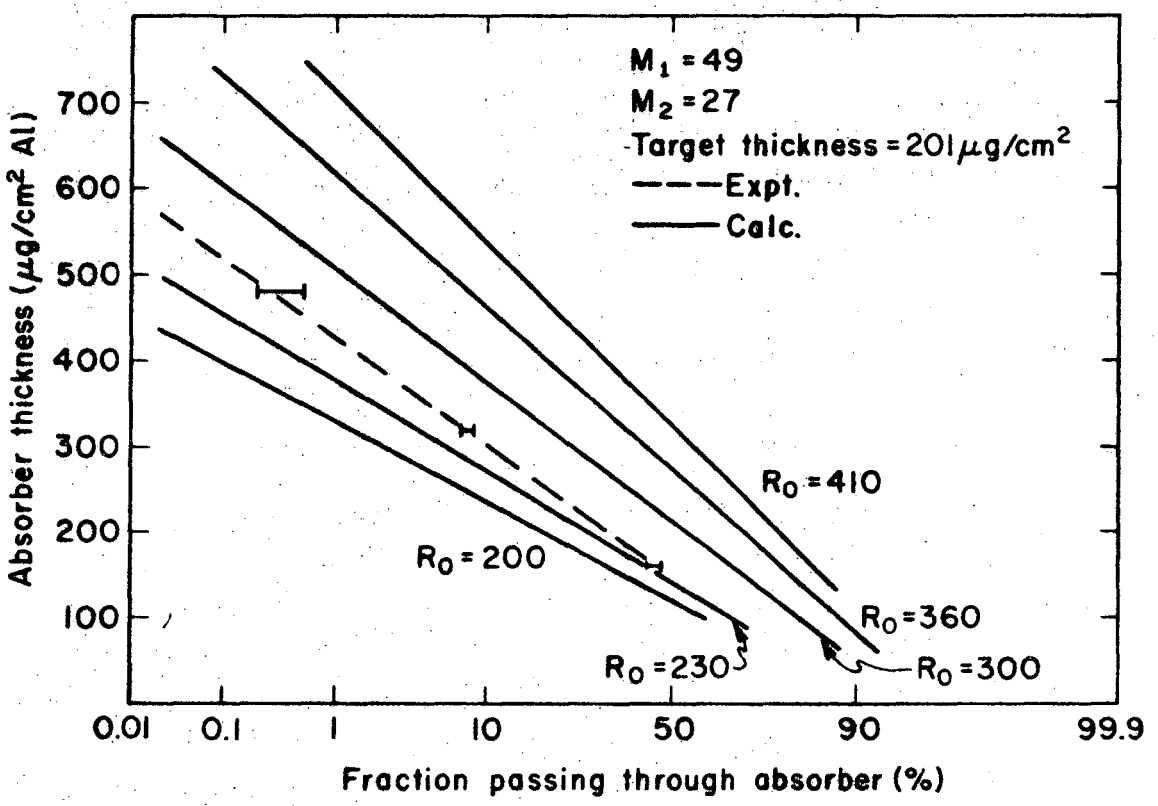

XBL701-2034

Fig. 32. Probability plot for ^{49}Cr recoil from $^{46}Ti(\alpha,n)^{49}Cr$. The large errors in experimental values are due to low counting rates. The solid lines are calculated. The experimental range is 250 $\mu g/cm^2$ Al.

Table VI. Results of forward recoil experiment for $^{4}He + ^{46}Ti$.

Product nucleus	Target thickness ($\mu g/cm^2$)	Bombardment energy (MeV)	Recoil[a] energy (MeV)	Range[b] (expt.) ($\mu g/cm^2$ in Al)	Range[c] (theo.) ($\mu g/cm^2$ in Al)
^{49}Cr	201	12.8	1.0	250	240
^{48}Cr	243	27.8	2.14	380	390
^{48}Cr	1000	31.6	2.4	390	400

[a]Recoil energy is calculated with Eq. (39).

[b]Experimental ranges are estimated from the probability plots of Figs. 30, 31, and 32.

[c]Theoretical ranges are based on Lindhard, et al. (Ref. 88).

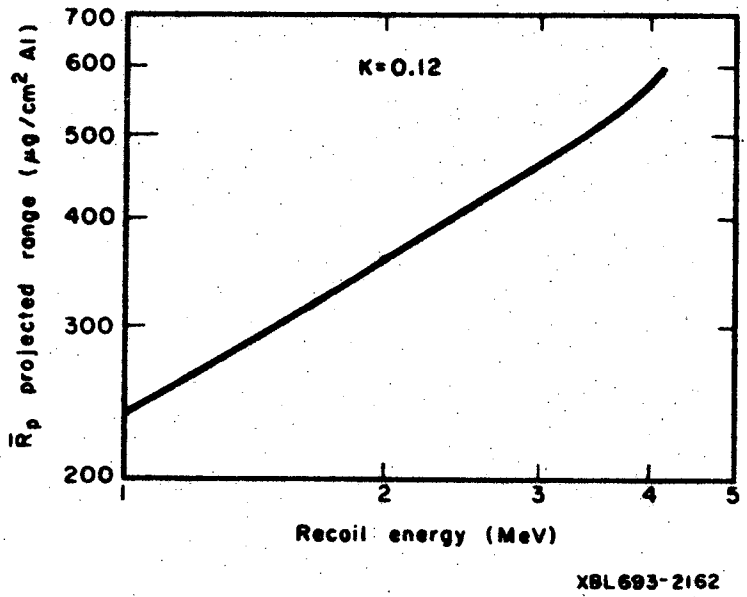

Fig. 33. Conventional range-energy curve for ^{48}Cr nuclei from $^{46}Ti(\alpha,2n)^{48}Cr$ reaction recoil into aluminum stopper. Calculation is performed from the theoretical curves in Lindhard et al. (Ref. 88).

and the good agreement between the experimental and the calculated average recoil ranges strongly indicates that the $^{46}Ti(\alpha,2n)^{48}Cr$ and $^{46}Ti(\alpha,n)^{49}Cr$ reactions proceed predominantly via a compound nucleus route, and the subsequent neutron decay is isotropic.[89]

No attempt has been made to measure the recoil ranges for the reactions involving heavy ions by this method. The condition that the target material possess approximately the same stopping power as the catcher material is not fulfilled. For the ^{3}He reactions, the bombarding energy at the peak of the $(^{3}He,n)$ or $(^{3}He,2n)$ excitation function is so low that the recoil energy is calculated to be less than 1 MeV. This low recoil energy renders the measurement using 160 $\mu g/cm^2$ Al catcher foils very unreliable. Thinner catcher foils must be employed to obtain reliable results.

VI. CONCLUSIONS

The experimental and theoretical results lead to several conclusions:

1. The reactions of ^{3}He, α, ^{16}O, ^{18}O, and ^{22}Ne with appropriate targets capable of forming the $^{50}Cr^{*}$ nucleus at excitation energies below 60 MeV proceed predominantly through a compound nucleus reaction mechanism.

2. A few reactions induced by ^{3}He, ^{18}O, and ^{22}Ne are strongly suppressed by the Coulomb barrier. When comparing excitation functions in light of the independence postulate, care must be taken to avoid comparison of the Coulomb-suppressed cross sections with the "natural" ones.

3. The ratio of σ_{pn}/σ_{2n} for all the five reactant pairs are effectively constant near the peaks of the respective excitation functions. The shapes of the experimental excitation functions for a given product are quite similar. Therefore, the independence postulate is quite reasonable, and is supported by this research, within experimental error.

4. Angular momentum effects must be considered to explain the energy shifts of the excitation functions for reactions involving different reactant pairs. Simple estimation of the rotational energy of the compound nucleus agrees reasonably with the observed energy shift.

5. Approximate calculation ignoring angular momentum is adequate to describe reaction systems involving low angular momenta. The level density parameter for such a calculation is smaller than that predicted for a Fermi-gas system.

6. A thick target can be used to yield information of recoil range distribution. From the average recoil range and the distribution, the reaction mechanism for $\alpha + {}^{46}Ti$ is found to be consistent with the compound-statistical theory.

ACKNOWLEDGMENTS

I wish to thank Professor Samuel S. Markowitz for his continuing assistance and patient guidance throughout my research.

I am grateful to Dr. James F. Lamb and Mrs. Diana Lee for their helpful discussions and assistance. I greatly appreciate the efforts of the electronics group, particularly F. S. Duarte, M. N. Firth, and M. K. Lee. I wish to thank Dr. R. Pehl and the semiconductor detector group for providing and maintaining the germanium and silicon detectors.

Appreciation is extended to the operators and staff of the HILAC and the 88-inch cyclotron. I wish also to thank R. M. Larimer and A. Ghiorso for scheduling the bombardments.

The assistance of E. Calhoon and the health chemistry group in transporting the targets is appreciated.

This work was performed under the auspices of the U. S. Atomic Energy Commission.

APPENDIX I

Spectrophotometric Analysis of Evaporated TiO_2 Targets

In preparation of vacuum evaporated TiO_2 targets, the titanium dioxide powder is evaporated in a tungsten crucible by electric heating. The high temperature involved may well be able to decompose the TiO_2 compound. It is therefore desirable to determine the chemical content of titanium after vacuum evaporation. The analysis is performed by measuring the color of the yellow complex formed by titanium and H_2O_2 in sulfuric acid solution.[90]

Procedure:

1. Dissolve the evaporated titanium dioxide (about 1 mg) and the aluminum backing foil in 5 ml of 1:1 H_2SO_4. Heat to dissolve if necessary.
2. Evaporate dry.
3. Dissolve in 7 ml of 3N H_2SO_4. Cover and warm to achieve complete solution. Cool.
4. Transfer to a 25 ml volumetric flask containing 1 ml of 3% H_2O_2.
5. Dilute to volume with distilled water.
6. Measure the absorbance against a blank at 400 mμ in a 1 cm cell. The blank is prepared by adding 7 ml of H_2SO_4 and 1 ml of 3% H_2O_2, and enough H_2O to 25 ml.

A calibration curve is prepared by performing the above procedure with known amount of TiO_2 and about 5 mg of Al foil. The absorbance follows Beer's law. The calibration curve is presented in Fig. 34.

The spectrophotometric determination shows that evaporation does change the composition of the deposited material. The determination of

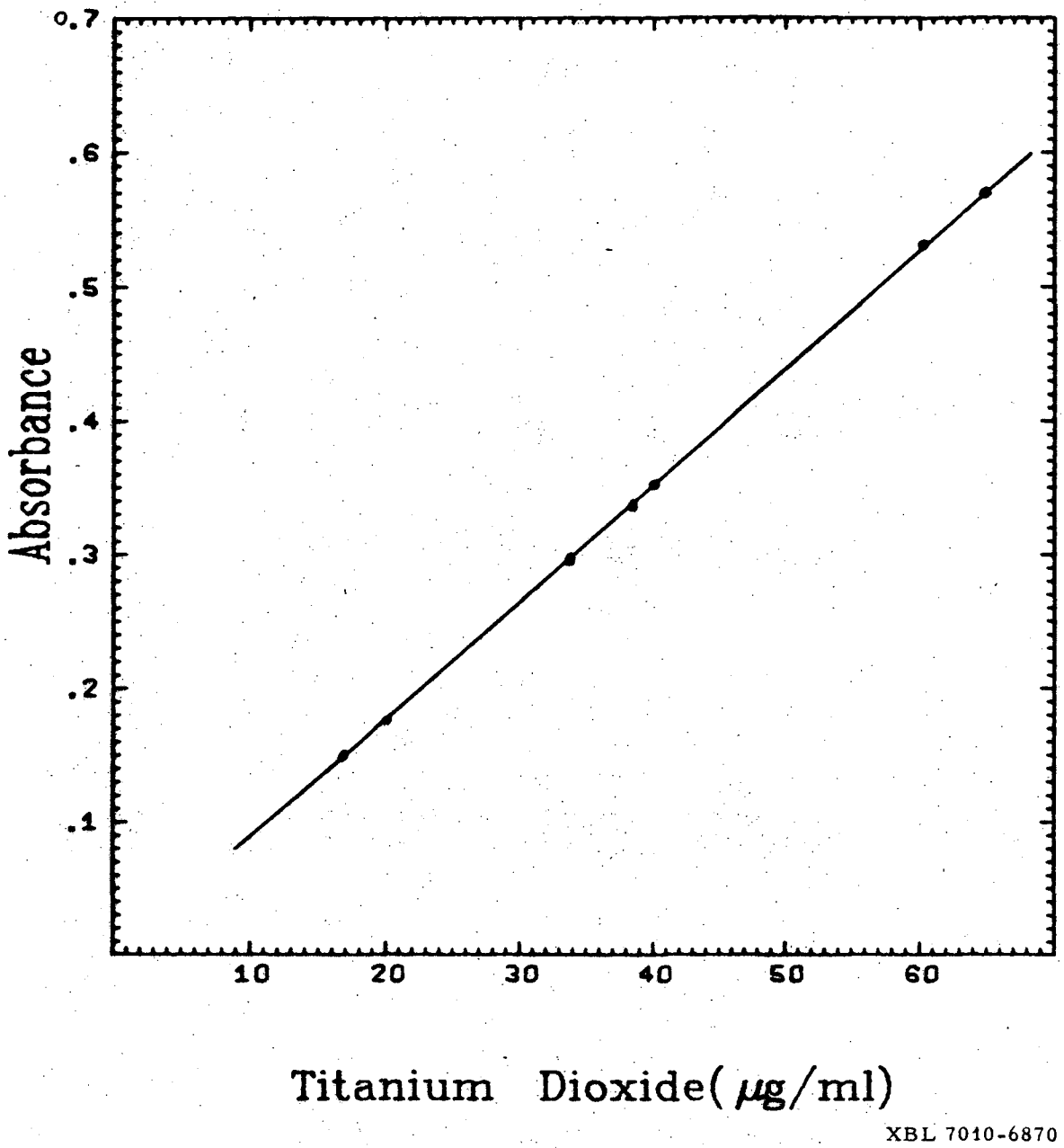

Fig. 34. Calibration curve for the spectrophotometric determination of titanium dioxide content in the evaporated targets.

six evaporated targets gives consistent values averaging 1.15. To obtain target thickness in numbers of atoms of titanium per cm^2, the titanium content of the evaporated target must be taken as 1.15 times that in TiO_2, that is

$$\% \text{ Ti in target} = \frac{\text{Ti}}{\text{TiO}_2} * 1.15 * 100.$$

APPENDIX II

Growth and Decay of ^{48}Cr From ^{48}V

With a radioactive decay sequence a → b → c, the behavior of the nuclear species b can be described as

$$\frac{d N_b}{d t} = \lambda_a N_a - \lambda_b N_b \quad , \tag{40}$$

where N_a, N_b are the number of atoms present at time t for species a and b; λ_a, λ_b are the decay constants of a and b. The solution of Eq. (40) can be obtained by standard techniques.[91] If we consider that species b is formed only from decay of a, we have

$$N_b = \frac{\lambda_a}{\lambda_b - \lambda_a} N_a^o \left(e^{-\lambda_a t} - e^{-\lambda_b t}\right) \quad , \tag{41}$$

where N_a^o is the value of N_a at t = 0.

In order to obtain the excitation functions for $^{47}Ti(^3He,pn)^{48}V$ and $^{46}Ti(^4He,pn)^{48}V$ reactions, it is necessary to determine the contribution of ^{48}V activity from the decay of ^{48}Cr. The sequence of decay is $^{48}Cr \xrightarrow{23hr} {}^{48}V \xrightarrow{16d} {}^{48}Ti$.

"Natural" Ti foils (5.8 mg/cm^2) are bombarded at the 88-inch cyclotron with 32 MeV α-particles for a total current of 1 μA-hr. The Ti foils are dissolved in a small amount of concentrated HF. After boiling off the HF with conc. HNO_3, the solution is cooled in an ice bath and a few drops of 30% H_2O_2 is added. The chromium is extracted with ethyl ether,[92] and back-extracted with dilute KOH solution. Finally the chromium is mounted as $BaCrO_4$.

The 0.116-MeV γ-ray (100%) of ^{48}Cr is measured with a Ge(Li) detector. The activity of ^{48}V is determined at the same time from the 0.98-MeV γ-ray (100%) of ^{48}V. The result is shown in Fig. 35.

The counting efficiencies of the 0.116- and 0.98-MeV γ-rays are determined using IAEA standards (see Appendix III). The growth and decay of ^{48}V is calculated based on Eq. (41) and the counting efficiencies. From an extrapolation of the decay curve of ^{48}V, we can obtain the contribution of $^{48}Cr \rightarrow {}^{48}V$ for this particular counting system: 405 counts of 0.116-MeV γ-ray observed will create 1 count of 0.98-MeV γ-ray.

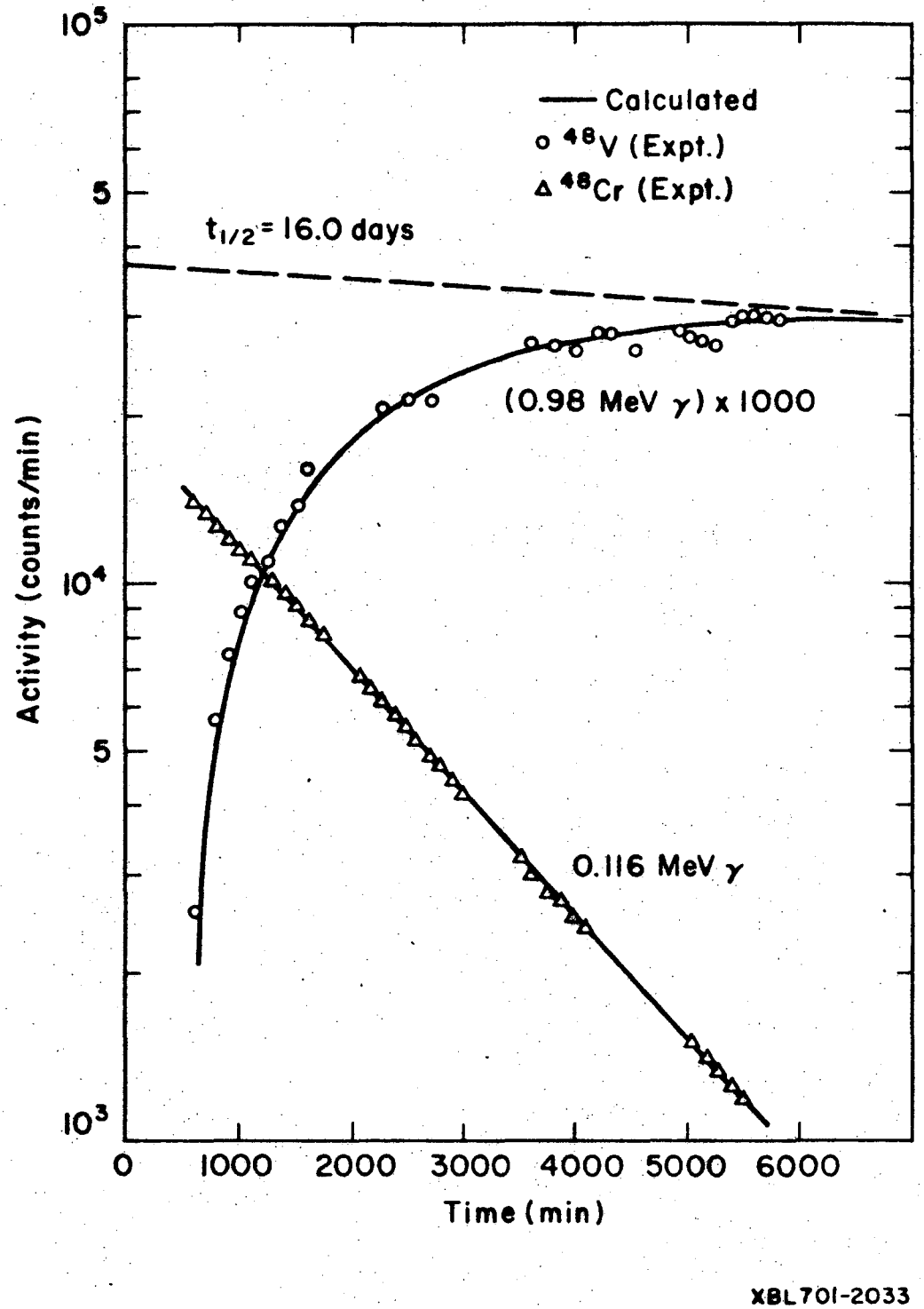

Fig. 35. Growth and decay of ^{48}V from the decay of ^{48}Cr. The solid lines are calculated from equations for simple and complex radioactive decay. The ^{48}V activity at later times (not shown) is extrapolated to t = 0 and is shown as the dotted line.

APPENDIX III

Determination of Gamma Ray Counting Efficiencies

The γ-ray photopeak counting efficiencies* for the two Ge(Li) detectors were calibrated using a set of eight absolute γ-ray standards obtained from the IAEA laboratory.[93] The absolute disintegration rate of the IAEA sources are known to within ±1%. The strength of the sources was about 10 μCi each. The energies of the γ-rays span from about 60 keV to 1836 keV. The detector efficiency* for a standard γ-ray is calculated from the count rate in the detector and the absolute disintegration rate with decay correction. The energy and decay scheme of the standards are obtained from the IAEA recommendations, which accompanied the set. Table VII summarizes the decay scheme corrections used.

The standards are counted with the Ge(Li) detectors at a fixed geometry. The γ-ray spectra are then analyzed using the computer code SAMPO as described in Chapter II. Because of the purity and intensity of the standards, SAMPO was able to define the photopeak areas to within ±1%. The results of the calibration of the γ-ray counting efficiencies are presented in Fig. 36. These curves are determined with the source 1 cm from the detector.

---

*The counting efficiency is defined to be

Counts per minute in the photopeak/No. of γ-photons emitted per minute.

Table VII. Nuclear data for the γ-ray standards.

Radionuclide	Half-life	Photon energy (keV)	% per disintegration
^{241}Am	432.9 years	59.54	35.9
^{57}Co	271.6 days	122.0	85.0
		136.3	11.4
^{203}Hg	46.8 days	72.9	9.7
		82.5	2.8
		279.2	81.6
^{22}Na	2.6 years	511. (from β^+)	181.1
		1274.6	100.
^{137}Cs	30.5 years	661.6	85.1
^{54}Mn	312.6 days	834.8	100.
^{60}Co	5.28 years	1173.2	100.
		1332.5	100.
^{88}Y	107.4 days	898.0	91.4
		1836.1	99.4

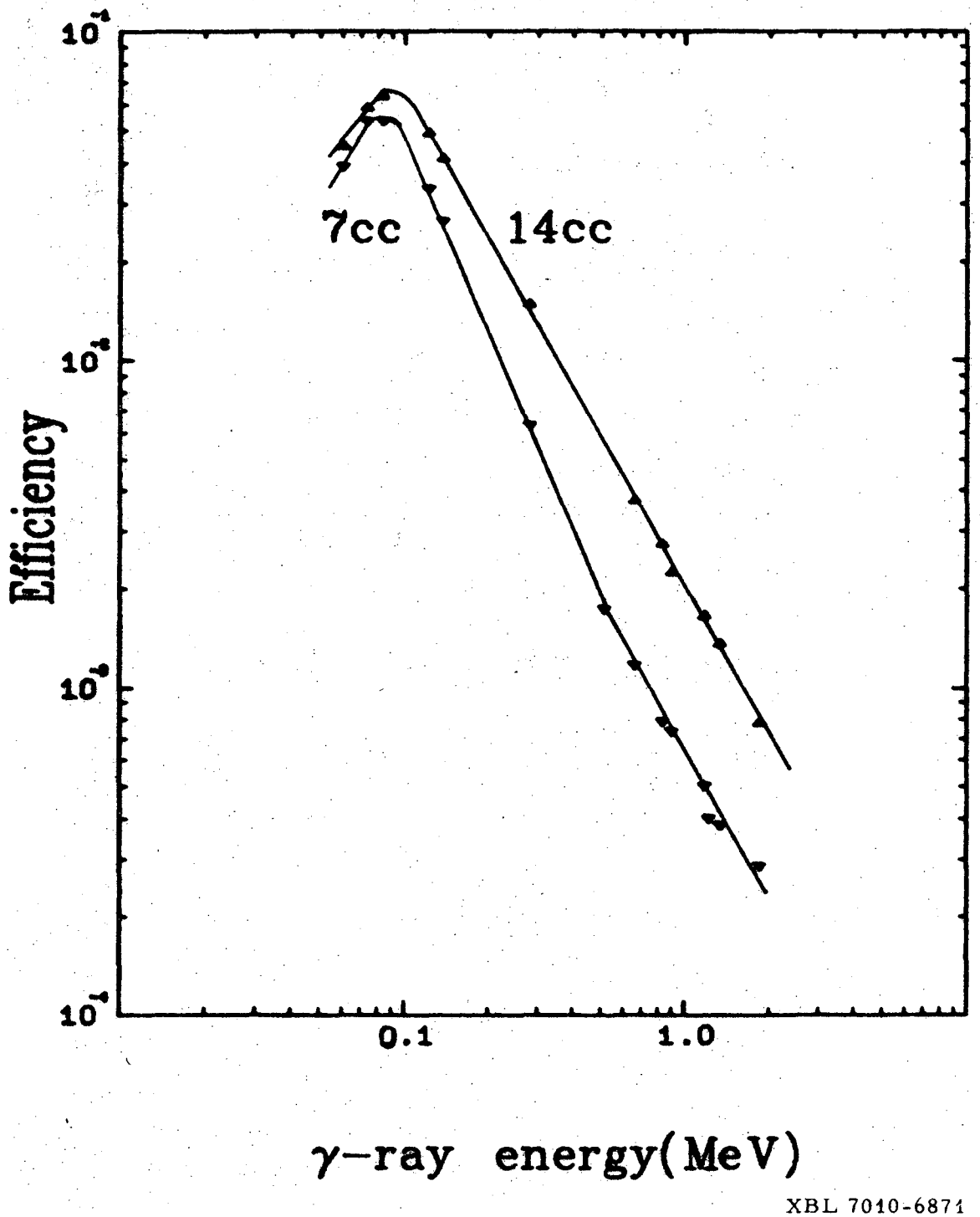

Fig. 36. Calibration curves for the determination of gamma-ray with Ge(Li) detectors. The points are obtained with the IAEA γ-ray standards placed 1 cm from the detector. The Ge(Li) detectors possess active volumes of 7 and 14 c. c.

APPENDIX IV

Determination of Titanium K X-Ray Counting Efficiency

A Si(Li) detector is used to measure the Ti K x-ray from ^{49}V decay. The x-ray energy for K_α transition[70] is 4.5 keV. In view of the low energy x-ray, many factors will affect the detection efficiency. Besides such factors as detector volume and counting geometry, source thickness, air absorption, and fluorescence yield all will effect the detection efficiency. Of course, it will be easy to determine the counting efficiency if an absolute standard of ^{49}V is commercially available. However no such standard is currently available.

Two methods have been employed in this work to determine the Ti x-ray counting efficiency. In this first method, decay of ^{51}Cr is used. Radioactive ^{51}Cr isotope was purchased from New England Nuclear Company[94] in the form of $CrCl_3$ in 0.5 N HCl. The source is prepared by evaporating the $^{51}CrCl_3$ solution on 0.5 mil gold foil. The absolute disintegration rate is determined by counting the 0.32 MeV γ-ray (9%) with a calibrated Ge(Li) detector. The source is then counted with the Si(Li) detector for the 4.95 keV x-ray. The detector efficiency for the 4.95 keV x-ray is then calculated using the fluorescence yield for the vanadium K x-ray,[95] 0.242. The efficiency for the detection of the 4.95 keV x-ray at 0.6 cm from the detector is 5.0×10^{-3}. Assuming the efficiency for the detection of 4.5 keV x-ray does not differ significantly from that for the 4.95 keV x-ray, the overall detection coefficient (ODC) for the ^{49}V decay can be obtained with the given fluorescence yield,[95] 0.213. The result is, $ODC = 1.06 \times 10^{-3}$.

In the second method, the decay of ^{48}V isotope is used. Natural titanium foil 0.5 mil thick is bombarded with 9 MeV protons. The reaction

$^{48}Ti(p,n)^{48}V$ predominates at this energy. The interference from $^{49}Ti(p,n)^{49}V$ reaction is negligible, because ^{48}Ti is much more abundant than ^{49}Ti in the target, and ^{48}V has a much shorter half-life. The ^{48}V is counted with a Ge(Li) detector for the 0.98 MeV (100%) γ-ray. The absolute disintegration rate is determined with the calibration curve in Appendix III. The decay of ^{48}V is taken to be 39% by electron capture.[96] The ^{48}V sample is then counted with the Si(Li) detector. The ODC for the detection of the 4.5 keV Ti K x-ray can be calculated. Because Ti x-ray is used, no fluorescence yield correction is necessary. The result is, ODC = 1.01×10^{-3}, within 5% of the determination by the ^{51}Cr method.

In addition to the errors in analyzing the γ-ray and x-ray spectra, three uncertainties will affect the ^{51}Cr determination--a) decay scheme, b) fluorescence yield, c) assumption that the detector efficiency for the 4.5 keV x-ray is the same as that for the 4.95 keV x-ray. Only decay correction is necessary for the method involving ^{48}V. Therefore, the second method is more reliable.

APPENDIX V

Remarks on Ghoshal's $^{64}Zn^*$ Compound System

In his original report (1950), Ghoshal[21] pointed out that in order to compare the excitation functions for the same radioactive product from different reaction entrance channels, corrections must be made to compensate the reaction Q values for different target-projectile pairs. In the absence of accurate mass data, Ghoshal arbitrarily shifted the excitation functions for the $^{1}H + {}^{63}Cu$ reactions 7 ± 1 MeV with respect to that for the $^{4}He + {}^{60}Ni$ system so that the maxima of the excitation functions coincide. Verification of the compound nucleus theory for this system was then claimed when a mass-spectrographic measurement gave a value of 5.74 ± 0.5 MeV for the energy shift.

However, recently more accurate measurements of the mass difference of $^{1}H + {}^{63}Cu$ and $^{4}He + {}^{60}Ni$ systems give a value[99] of 3.75 MeV. It would be interesting to see the result of an energy shift of only 3.75 MeV, not 7 MeV. In Fig. 37, Ghoshal's data are replotted, using an energy shift of 3.75 MeV for the $^{1}H + {}^{63}Cu$ system. It is noted immediately that the compound nucleus assumption can not be used to adequately describe this data.

More drastic deviations from the independence postulate can be illustrated by plotting the cross section ratios (α,n)/(p,n), (α,pn)/(p,pn), and (α,2n)/(p,2n). If the independence postulate is upheld, then

$$\frac{\sigma(\alpha,n)}{\sigma(p,n)} = \frac{\sigma(\alpha,pn)}{\sigma(p,pn)} = \frac{\sigma(\alpha,2n)}{\sigma(p,2n)} = \frac{\sigma_\alpha(E^*)}{\sigma_p(E^*)} \quad , \tag{42}$$

where $\sigma_\alpha(E^*)$ and $\sigma_p(E^*)$ are the cross sections for the formation of the compound nucleus with excitation energy E^* by α and p reactions.

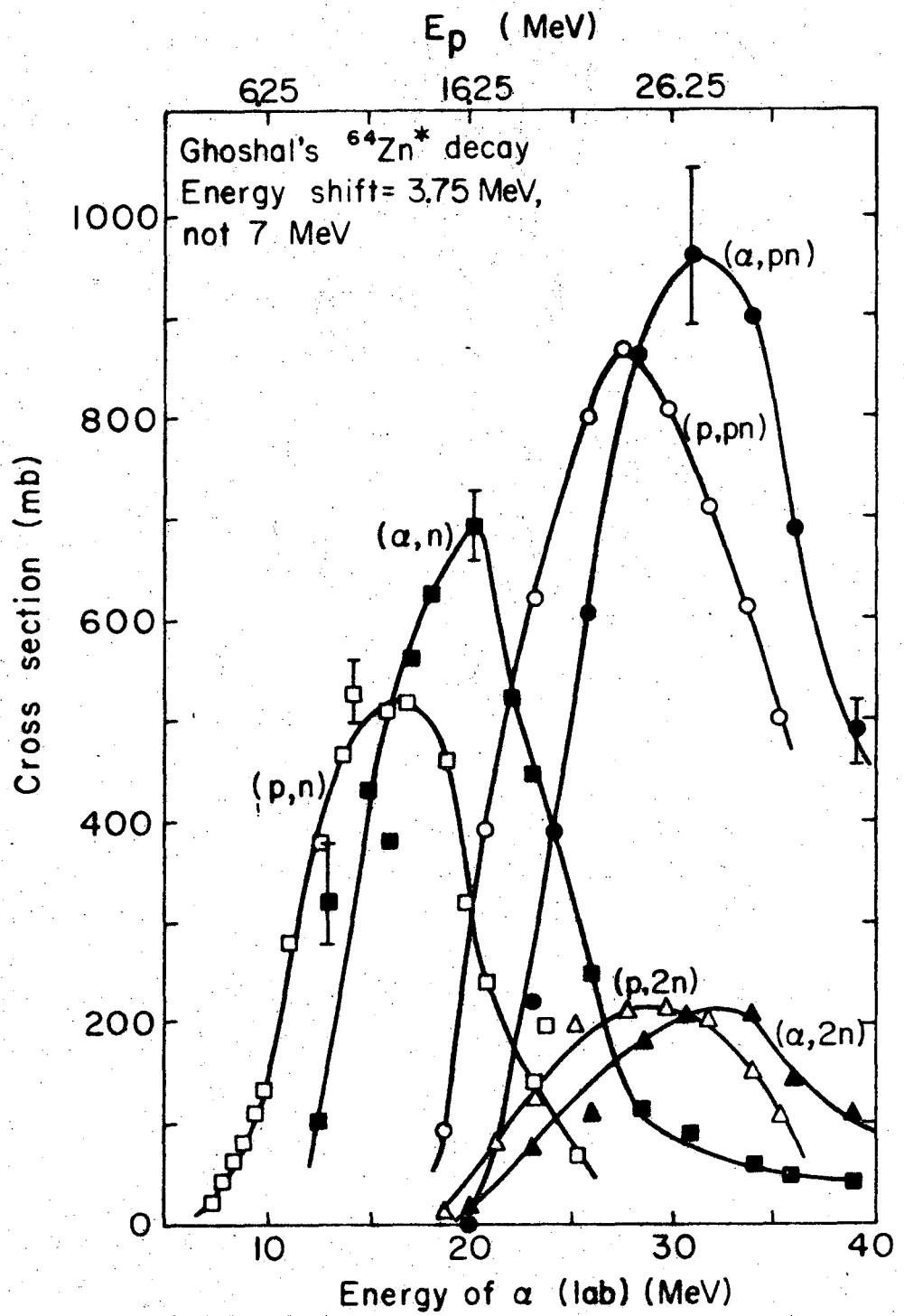

XBL714-3254

Fig. 37. Excitation functions for the $^{64}Zn^*$ compound nucleus system. Data are taken from Ghoshal (Ref. 21). The energy shift of the ^{1}H + ^{63}Cu system with respect to the ^{4}He + ^{60}Ni system is 3.75 MeV, not 7 MeV. The reactions are $^{63}Cu(p,n)^{63}Zn$, $^{60}Ni(\alpha,n)^{63}Zn$, $^{63}Cu(p,pn)^{62}Cu$, $^{60}Ni(\alpha,pn)^{62}Cu$, $^{63}Cu(p,2n)^{62}Zn$, and $^{60}Ni(\alpha,2n)^{62}Zn$. Black symbols = ^{60}Ni target, open symbols = ^{63}Cu target.

Figure 38 shows the ratios of the cross sections. While the ratios obtained after 7-MeV energy shift fall consistently near the value of one, with the more reasonable 3.75 MeV shift, the equalities in Eq. (42) are no longer observed.

It must be pointed out, however, that the experimental cross sections for $^{4}He + ^{60}Ni$ reactions from Ghoshal differ significantly (about 4 MeV energy shift) with those obtained by Tanaka,[97] Smith,[25] and McGowan et al.[98] Detailed analysis of the $^{64}Zn^{*}$ compound nucleus system with consideration of angular momentum effects can be found in Ref. 25.

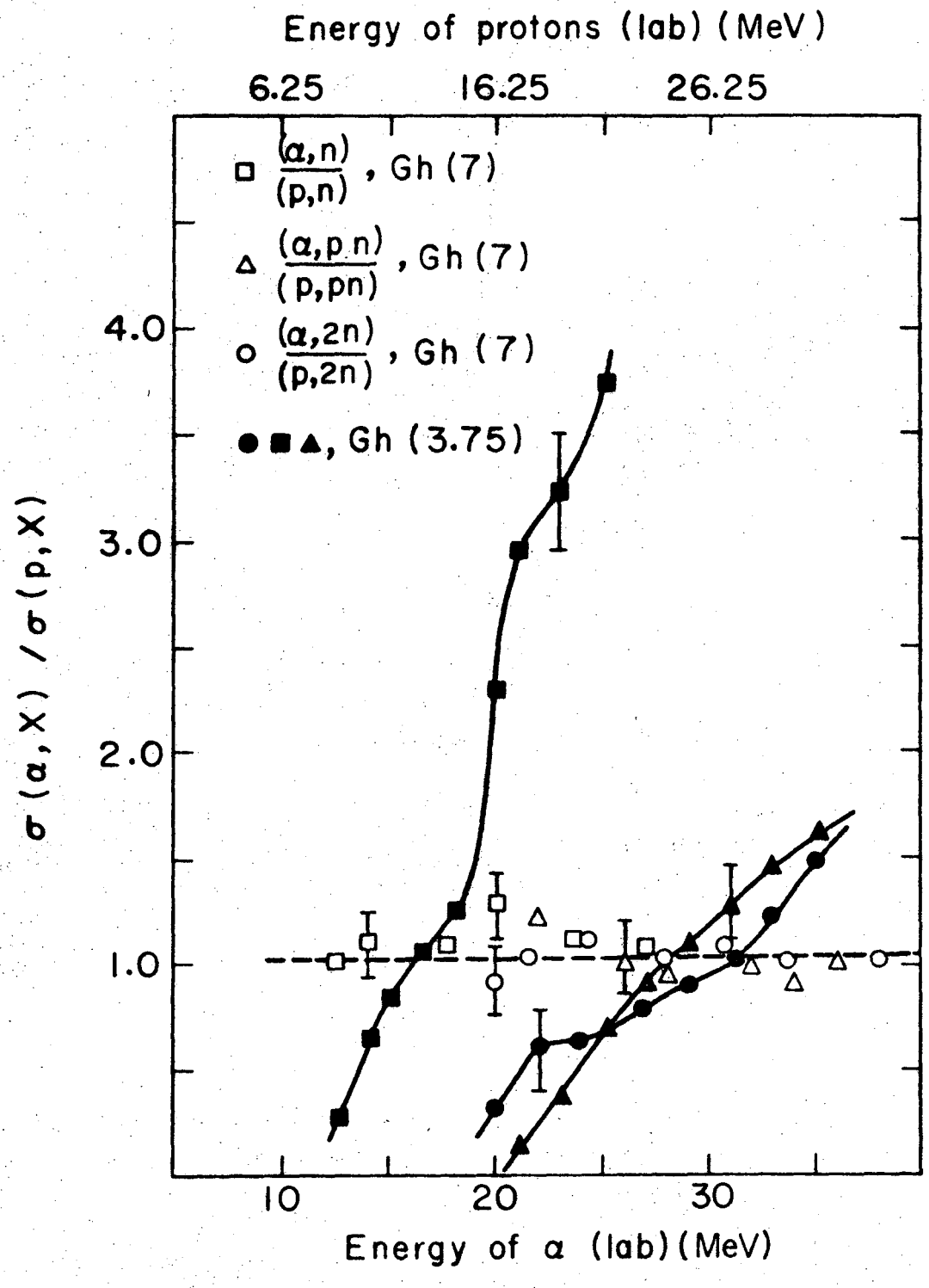

XBL714-3253

Fig. 38 Ratios of the cross sections for the $^{1}H + ^{63}Cu$ and the $^{4}He + ^{60}Ni$ reactions. The open symbols refer to the ratios calculated with a 7 MeV proton energy shift. The solid symbols refer to that calculated with a proton energy shift of 3.75 MeV. The data used are taken from Ghoshal (same as those used in Fig. 37).

REFERENCES

1. N. Bohr, Nature 137, 344 (1936).
2. V. Weisskopf, Phys. Rev. 52, 295 (1937).
3. T. Ericson, Advan. Phys. 9, 424 (1960).
4. D. Bodansky, Ann. Rev. Nucl. Sci. 12, 79 (1962).
5. G. D. Harp, J. M. Miller, and B. J. Berne, Phys. Rev. 165, 1166 (1968).
6. D. V. Reames, Phys. Rev. 137, B332 (1965).
7. F. E. Durham and M. L. Halbert, Phys. Rev. 137, B850 (1965).
8. M. J. Fluss, J. M. Miller, J. M. D'Auria, N. Dudey, B. M. Foreman, Jr., L. Kowalski, and R. C. Reedy, Phys. Rev. 187, 1449 (1969).
9. M. L. Halbert, F. E. Durham, and A. van der Woude, Phys. Rev. 162, 899 (1967).
10. L. Kowalski, J. C. Jodogne, and J. M. Miller, Phys. Rev. 169, 894 (1968).
11. J. M. Alexander and G. N. Simonoff, Phys. Rev. 162, 952 (1967).
12. D. W. Seegmiller and K. Street, Phys. Rev. C1, 695 (1970).
13. For example, N. T. Porile, S. Tanaka, H. Amano, M. Furukawa, S. Iwata, and M. Yaki, Nucl. Phys. 43, 5000 (1963).
14. R. M. Eisberg, D. R. Yennie, D. H. Wilkinson, Nucl. Phys. 18, 338 (1960).
15. D. G. Sarantites and B. D. Pate, Nucl. Phys. A93, 545 (1967).
16. T. D. Thomas, Ann. Rev. Nucl. Sci. 18, 343 (1968).
17. M. Blann, Nucl. Phys. 80, 223 (1966).
18. D. Sperber, Phys. Rev. 141, 927 (1966).
19. J. R. Grover, Phys. Rev. 123, 267 (1961).
20. H. A. Weidenmüller, Comments Nuclear Particle Phys. 3, 16 (1969).
21. S. N. Ghoshal, Phys. Rev. 80, 939 (1950).

22. J. R. Grover and R. J. Nagle, Phys. Rev. 134, B1248 (1964).

23. W. John, Phys. Rev. 103, 704 (1956).

24. K. L. Chen and J. M. Miller, Phys. Rev. 134, B1269 (1964).

25. C. Smith, Jr., Lawrence Radiation Laboratory Report UCRL-11862, Ph.D. Thesis, 1965 (unpublished).

26. L. Wolfenstein, Phys. Rev. 82, 690 (1951).

27. J. M. D'Auria, M. J. Fluss, G. Herzog, L. Kowalski, J. M. Miller, and R. C. Reedy, Phys. Rev. 174, 1409 (1968).

28. M. K. Go and S. S. Markowitz, Lawrence Radiation Laboratory Report UCRL-18667, p. 29 (1969).

29. C. F. Williamson, J. P. Boujot, and J. Picard, Commissariat à'l'Energie Atomique Report, CEA-R3042 (1966).

30. W. H. Barkas and M. J. Berger, NAS-NRC 1133, 103 (1964).

31. H. Bischel, Lawrence Radiation Laboratory Report UCRL-17538 (1967).

32. P. G. Steward, Lawrence Radiation Laboratory Report UCRL-18127, Ph.D. Thesis (1968).

33. E. L. Kelly, Nucl. Instr. Methods 18, 19, 33 (1962).

34. E. L. Hubbard, W. R. Baker, K. W. Ehlers, H. S. Gordon, R. M. Main, N. J. Norris, R. Peters, L. Smith, C. M. Van Atta, F. Voelker, C. E. Anderson, R. Beringer, R. L. Gluckstern, W. J. Knox, M. J. Malkin, A. R. Quinton, L. Schwarcz, and G. W. Wheeler, Rev. Sci. Instr. 32, 621 (1961).

35. P. P. Webb and R. L. Williams, Nucl. Instr. Methods 22, 361 (1963).

36. J. H. Elliot, Nucl. Instr. Methods 12, 60 (1960).

37. F. S. Goulding, Nucl. Instr. Methods 43, 1 (1966).

38. F. S. Goulding, D. A. Landis, and R. H. Pehl, Lawrence Radiation Laboratory Report UCRL-17560 (1967).

39. F. S. Goulding and D. A. Landis, Proceedings of the Conference on Instrumentation Techniques in Nuclear Pulse Analysis, Monterey, NAS-NRC, 1184 (1963).

40. Manufactured by the Victoreen Instrument Co., Cleveland, Ohio.

41. Manufactured by the Northern Scientific, Inc., Madison, Wisconsin.

42. D. A. Landis, F. S. Goulding, and J. M. Jaklevic, Nucl. Instr. Methods (to be published), UCRL-19796 (June, 1970).

43. M. K. Lee, Lawrence Radiation Laboratory, Instr. No. 19X 2920P1 and 19X 2750P1.

44. Manufactured by Cipher Data Products, Inc., San Diego, California.

45. J. T. Routti and S. Prussin, Nucl. Instr. Methods 72, 125 (1969).

46. F. M. Bernthal, Lawrence Radiation Laboratory Report UCRL-18651, Ph.D. Thesis (1969).

47. J. T. Routti, Lawrence Radiation Laboratory Report UCRL-18514, Ph.D. Thesis (1969).

48. RAD is a program modified by C. Rugge, Lawrence Radiation Laboratory, Berkeley, from the Los Alamos least square package, LA-2367.

49. J. B. Cumming, NAS-NRC Nuclear Science Series, NAS-NS-3107, 25 (1963).

50. S. S. Markowitz, J. M. Miller, and G. Friedlander, Phys. Rev. 98, 1197 (1955).

51. N. T. Porile, Phys. Rev. 315, 939 (1959).

52. For example, see J. M. Miller and F. S. Houck, Bull. Am. Phys. Soc. Ser. II, 2, 60 (1957) and S. N. Ghoshal (Ref. 21).

53. D. O. Raleigh, Ph.D. Thesis, Columbia University, 1960 (unpublished).

54. B. N. Kalinkin and I. Z. Petkov, Acta Phys. Polon. 25, 265 (1964); (English translation: UCRL translation No. 1151, 1964).

55. R. Kaufman and R. Wolfgang, Phys. Rev. 121, 192 (1961).

56. A. Zucker, Ann. Rev. Nucl. Sci. 10, 183 (1960).

57. J. B. Natowitz, Phys. Rev. C1, 2157 (1970).

58. J. A. McIntyre, T. L. Watts, and F. C. Jobes, Nucl. Instr. Methods 21, 281 (1963).

59. L. C. Becker, G. K. Tandon, F. C. Jobes, J. A. McIntyre, and T. L. Watts, Nucl. Instr. Methods 21, 298 (1963).

60. J. F. Lamb, Lawrence Radiation Laboratory Report UCRL-18981, Ph.D. Thesis, 1969 (unpublished).

61. J. M. Lang and K. J. LeCouteur, Proc. Phys. Soc. London, 67A, 586 (1954).

62. H. Hurwitz and H. A. Bethe, Phys. Rev. 81, 898 (1951).

63. T. Ericson, Nucl. Phys. 11, 481 (1959).

64. A. G. W. Cameron, Can. J. Phys. 36, 1040 (1958).

65. I. Dostrovsky, Z. Fraenkel, and G. Friedlander, Phys. Rev. 116, 683 (1959).

66. N. D. Dudey, I. Kowalski, and J. M. Miller, Phys. Rev. 163, 1074 (1967).

67. M. M. Shapiro, Phys. Rev. 90, 171 (1953).

68. P. A. Seeger, Nucl. Phys. 25, 1 (1961).

69. J. R. Grover, Phys. Rev. 127, 2142 (1962).

70. C. M. Lederer, J. M. Hollander, and I. Perlman, Table of Isotopes, sixth edition, John Wiley and Sons, Inc., New York (1967).

71. E. H. Auerbach, Brookhaven National Laboratory Report BNL-6562, unpublished (1964).

72. D. C. Williams and T. D. Thomas, Nucl. Phys. A92, 1 (1967).

73. T. D. Thomas, Nucl. Phys. 53, 577 (1964).

74. J. R. Grover, Phys. Rev. 157, 832 (1967).

75. J. O. Newton, F. S. Stephens, R. M. Diamond, W. H. Kelly, and H. Ward, Nucl. Phys. A141, 631 (1970).

76. T. Ericson and V. M. Strutinski, Nucl. Phys. 8, 284 (1958); and 9, 689 (1959).

77. R. Vandenbosch and J. R. Huizenga, Phys. Rev. 120, 1313 (1960).

78. W. L. Hafner, Jr., J. R. Huizenga, and R. Vandenbosch, Argonne National Laboratory Report ANL-6662, unpublished (1962).

79. E. H. Auerbach and C. E. Porter, Proceedings of the Third Conference on Reactions Between Complex Nuclei, Eds. A. Ghiorso, R. M. Diamond, and H. E. Conzett (University of California Press, Berkeley and Los Angeles, 1963), p. 19.

80. T. D. Thomas, Phys. Rev. 116, 703 (1959).

81. D. L. Hill and J. A. Wheeler, Phys. Rev. 89, 1102 (1953).

82. J. R. Huizenga and G. Igo, Nucl. Phys. 29, 462 (1962).

83. J. R. Grover and J. Gilat, Phys. Rev. 157, 802 (1967).

84. V. Subrahmanyam and M. Kaplan, Phys. Rev. 142, 174 (1966).

85. B. G. Harvey, Ann. Rev. Nucl. Sci. 10, 235 (1960).

86. R. B. Leachman and H. Atterling, Arkiv Fysik 13, 101 (1958).

87. L. Winsberg and J. M. Alexander, Phys. Rev. 121, 518 (1961).

88. J. Lindhard, M. Scharff, and H. Schiøtt, Danske Videnskab Selskab Mat.-Fys. Medd. 33, No. 14 (1963).

89. The same conclusion can be reached by assuming that the neutrons are emitted symmetrically about an axis perpendicular to the beam direction.

90. E. F. Norton, National Academy of Science Report NAS-NS-3111, p. 86.

91. G. Friedlander, J. Kennedy, and J. Miller, Nuclear and Radiochemistry, (John Wiley and Sons, New York, 1966), p. 72.

92. W. W. Meinke, Lawrence Radiation Laboratory Report UCRL-432, p. 24-3 (1949).

93. International Atomic Energy Agency, Vienna, Austria.

94. New England Nuclear Co., Boston, Mass.

95. R. W. Fink, R. C. Jopson, H. Mark, and C. D. Swift, Rev. Mod. Phys. 38, 513 (1966).

96. R. A. Ristinen, A. A. Bartlett, and J. J. Kranshaar, Nucl. Phys. 45, 321 (1963).

97. S. Tanaka, J. Phys. Soc. Japan, 15, 2159 (1960).

98. F. K. McGowan, P. H. Stelson, and W. G. Smith, Bull. Am. Phys. Soc. II 5, 266 (1960).

99. J. H. E. Mattauch, W. Theile, and A. H. Wapstra, Nucl. Phys. 67, 1 (1965) as quoted in "Nuclear Wallet Cards" (sheets) January, 1971, prepared by S. Morse and F. Ajzenberg-Selove.

TECHNICAL INFORMATION DIVISION
LAWRENCE RADIATION LABORATORY
UNIVERSITY OF CALIFORNIA
BERKELEY, CALIFORNIA 94720